論文 / 著書情報
Article / Book Information

題目(和文)	AlScNチャネルトランジスタのコンタクト抵抗低減に関する研究
Title(English)	A Study on Low Resistance Ohmic Contact for AlScN Channel MOSFET
著者(和文)	片岡淳司
Author(English)	Junji Kataoka
出典(和文)	学位:博士（工学）, 学位授与機関:東京工業大学, 報告番号:甲第11927号, 授与年月日:2021年3月26日, 学位の種別:課程博士, 審査員:角嶋 邦之,筒井 一生,若林 整,渡辺 正裕,飯野 裕明,岩井 洋
Citation(English)	Degree:Doctor (Engineering), Conferring organization: Tokyo Institute of Technology, Report number:甲第11927号, Conferred date:2021/3/26, Degree Type:Course doctor, Examiner:,,,,,
学位種別(和文)	博士論文
Type(English)	Doctoral Thesis

Doctoral Thesis

A Study on Low Resistance Ohmic Contact for AlScN Channel MOSFET

A Dissertation Submitted to the Department of Electrical and Electronic Engineering

School of Engineering, Tokyo Institute of Technology

March 2021

Junji Kataoka

Supervisor: Assoc. Prof. Kuniyuki Kakushima

Abstract

$Al_{1-x}Sc_xN$ films are attractive materials for high-sensitive piezoelectric sensors and filters because of their high piezoelectric coefficient with a high-temperature tolerance. Besides, recent works have experimentally demonstrated that the $Al_{1-x}Sc_xN$ films exhibit ferroelectric properties with a high remnant polarization (P_r) of over 100 μC/cm^2.The bandgap of the $Al_{1-x}Sc_xN$ film which shows the ferroelectricity is from 3.0 to 6.0 eV, indicating that the $Al_{1-x}Sc_xN$ films can be considered as one of the nitride semiconductors. Once we can control the carrier charge types of the $Al_{1-x}Sc_xN$ films for source and drain, complementary metal-oxide-semiconductor (CMOS) thin-film transistors (TFT) with ferroelectric $Al_{1-x}Sc_xN$ channel can be realized, which opens a wide range of unique applications. One of the issues for using the $Al_{1-x}Sc_xN$ film as a channel of the TFT is the formation of contacts with low Ohmic contact resistance (ρ_c). The key to achieving the low ρ_c is lowering the Schottky barrier height (ϕ_B) and/or increasing the carrier concentration (N) of the $Al_{1-x}Sc_xN$ film. The purpose of the thesis is the extraction of band alignment of metal/$Al_{1-x}Sc_xN$ interface and propose a guideline to reduce the ϕ_B, and also to demonstrate n-type conduction to increase in the N for low ρ_c.

The band alignment was extracted by leakage current analysis of the metal/ferroelectric/metal (MFM) capacitors with either TiN or W electrode. The electron conduction through the $Al_{0.78}Sc_{0.22}N$ film followed the Schottky emission model with an initial ϕ_B of 0.46 and 0.55 eV for TiN and W electrodes, respectively. During the first ferroelectric polarization switching, a gradual shift in the leakage current was observed, changing the effective ϕ_B to 0.36 eV for both electrodes. After the initial polarization switching, the current level kept the same level during the further positive/negative sweeping, indicating that the ϕ_B for both polarization states (metal-face, N-face) was the same. The formation of an interface dipole layer possibly formed by nitrogen vacancies (V_N) at the metal interface can be deduced from the modeling of the Richardson constant (A^*). With the obtained results, a small ϕ_B to reduce the ρ_c can be achieved by forming

the interface dipole layer at the interface.

The demonstration of the n-type conduction in the $Al_{0.78}Sc_{0.22}N$ film was achieved by Si ion doping followed by activation annealing. The activation of Si atoms was found above an annealing temperature of 800°C. Under a dose of 2×10^{15} cm^{-2} with an activation annealing at 900°C, n-type conduction was obtained with Hall mobility and a carrier concentration of 8.6 cm^2/Vs and 8.9×10^{18} cm^{-3}, respectively. The Si atom concentration in the $Al_{0.78}Sc_{0.22}N$ film was 4.1×10^{20} cm^{-3} by secondary ion mass spectroscopy. Therefore, the activation ratio can be deduced to be 2.2%. The activation annealing temperature of implanted Si atoms in $Al_{0.78}Sc_{0.22}N$ film is relatively low for those implanted to AlN or AlGaN. The n-type conduction was realized in a relatively low-temperature process. This can be an advantage for applications such as the ferroelectric semiconductor-FET.

The surface of the n-type $Al_{0.78}Sc_{0.22}N$ film turned out to be sensitive to exposure to air, and two orders of magnitude increase in the sheet resistance (R_s) were measured. The mechanism of the increase in R_s was explained by H_3O^+ molecules adsorption by self-ionization of water in the air to the Si-doped $Al_{0.78}Sc_{0.22}N$ surface. With the adsorption, a depletion region from the backside of the $Al_{0.78}Sc_{0.22}N$ film is formed, caused by the balance between the spontaneous polarization and surface charges. To overcome this issue, it is necessary to coat a proper passivation layer on the n-type $Al_{0.78}Sc_{0.22}N$ film, or either thicken the n-type $Al_{0.78}Sc_{0.22}N$ film or increase the carrier concentration of n-type $Al_{0.78}Sc_{0.22}N$ film.

Based on the obtained results, the remaining issues of $Al_{1-x}Sc_xN$ films for TFT application are summarized. Considering other n-type semiconductors used for TFT, the ρ_c needs to be further reduced to increase the current density. Therefore, it is essential to increase the carrier concentration of the $Al_{1-x}Sc_xN$ film. Secondly, the demonstration of p-type conduction by impurity doping is required for CMOS application. Also, a carrier conduction model between the ferroelectric and doped regions needs to be constructed.

Table of contents

Chapter 1. Introduction

1.1 Channel material for thin-film transistors

Thin-film transistors (TFTs) are widely used for the switching elements of image sensors and liquid crystal display (LCD). TFT is a field-effect transistor (FET) composed of a semiconductor layer, a dielectric layer, and electrodes at source, drain, and gate. The conductivity of the semiconductor layer is controlled by the gate voltage application. Recently, as the TFT can be fabricated at a low-temperature process, it has attracted attention as a back-end-of-line (BEOL) transistor for 3D-LSIs. [1-1, 1-2]

In the field of LCD devices, a technology called memory-in-pixel (MIP) is drawing attention to low power consumption. The MIP is a technology that gives a memory function to the pixels, keeping the static image unchanged. The current MIP technology consists of a static-random-access memory (SRAM) circuit for each pixel in the liquid crystal drives. [1-3] However, SRAM is still power consuming, giving a high transient current during the switching. Also, as SRAM is composed of at least six transistors, it occupies large area, reducing the efficiency of the backlight energy consumption. Therefore, the TFT embedded memory with low power consumption is required.

The ferroelectric liquid crystal display (F-LCD) is a display technology with memory function and is proposed in 1980 by Clark and Lagerwall. [1-4] Liquid crystal molecules with ferroelectric have a helical structure in enough thick cells. However, when the width of the cell is narrowed down to 1 μm, the helical structure disappears and only two states in which the remnant polarization is up or down become stable. [1-5] By applying an electric field, only one state can exist at the same time, so that the two states can be switched. The F-LCD has several advantages in terms of high-speed response, viewing angle, memory function, and so on. Above all, the F-LCD has not been used as a direct-view display device due to its manufacturing problem for large-area displays on the instability of the layered structure of ferroelectric liquid crystal in the thin cell, and the issue of tolerance against physical impact. [1-6, 1-7, 1-8] Table 1.1 shows the comparison of

the display technology with memory function.

Table 1.1 Comparison of the display technology with memory function. [1-5~1-9]

	FLCD	MIP by ferro. TFT
Memory function	Ferroelectric liquid crystal	Driver circuit
P_r (μC/cm^2)	0.1~0.3	100 (AlScN)
issue	Synthesis of ideal ferroelectric liquid crystal materials.	Realization of n/p-type ferroelectric semiconductor

TFT using a ferroelectric semiconductor for the channel can be a solution for the MIP application. Figure 1.1 shows the difference in structure between the well-known ferroelectric-FET and the ferroelectric semiconductor-FET. In the ferroelectric-FET, a ferroelectric film is used as a gate insulator in a standard metal-oxide-semiconductor field-effect transistor (MOSFET). As the channel conductance changes depending on the direction of polarization in the ferroelectric film, the polarization state can detect by the measurement of the channel conductance. With this structure, the data reading operation is non-destructive. However, the ferroelectric-FET has an issue of the short retention times originated from the depolarization field and the large gate leakage current caused due to the poor insulation of the polycrystalline ferroelectric insulator, which limits their commercialization. [1-10] To overcome this issue, the ferroelectric-semiconductor-FET was proposed. [1-10] In ferroelectric semiconductor-FET, the ferroelectric semiconductor film is used as a channel in the general MOSFET. The polarization in the ferroelectric semiconductor layer changes the conductance of the ferroelectric semiconductor layer. A significant difference between the ferroelectric-FET and the ferroelectric semiconductor-

FET is that the ferroelectric semiconductor-FET can use high-quality amorphous material such as SiO_2 for the gate insulator, which can potentially suppress the gate leakage current.

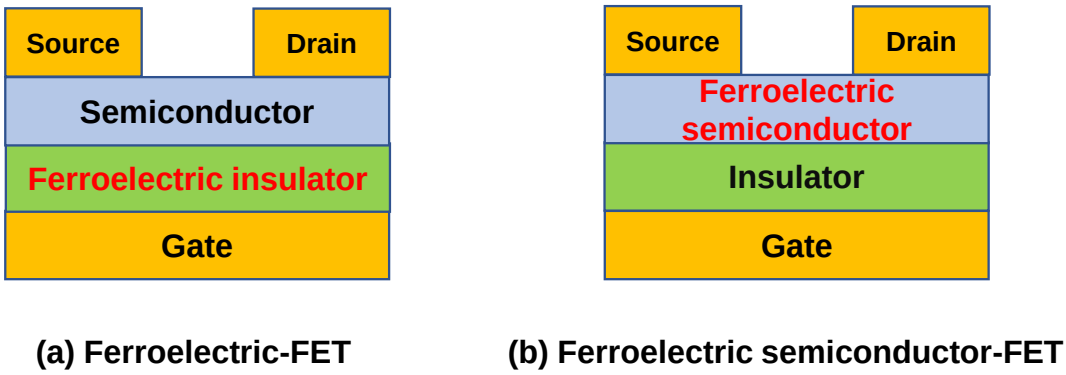

Fig. 1.1 Schematic structures of (a) ferroelectric-FET, and (b) ferroelectric semiconductor-FET.

The working mechanism of the ferroelectric semiconductor-FET is as follows. By applying an electric field, the polarization switching occurs throughout the ferroelectric semiconductor layer. Therefore, the conductive path can be formed at the top surface of the ferroelectric semiconductor layer. In the downstate polarization case as shown in fig. 1.2 (a), (b), the channel resistance is high due to the absence of the mobile charges at the bottom surface of the ferroelectric semiconductor layer as shown in fig. 1.2 (b). On the other hand, in the case of the upstate polarization as shown in fig. 1.2 (c), (d), the channel resistance is low because the mobile charges accumulate at the top surface of the ferroelectric semiconductor layer and the conductive path is formed. Therefore, the drain current on the gate voltage (I_d-V_g) curve shows a counterclockwise hysteresis as shown in fig. 1.2 (e). The presence of the fixed charge states at the metal/ferroelectric semiconductor interface leads to a shift of the I_d-V_g curve as shown in fig. 1.2 (f). If the electron trap states exist at the ferroelectric semiconductor/insulator interface, the I_d-V_g curve may show a clockwise hysteresis, leading to the disappearance of the hysteresis caused by the P_r in the ferroelectric semiconductor layer.

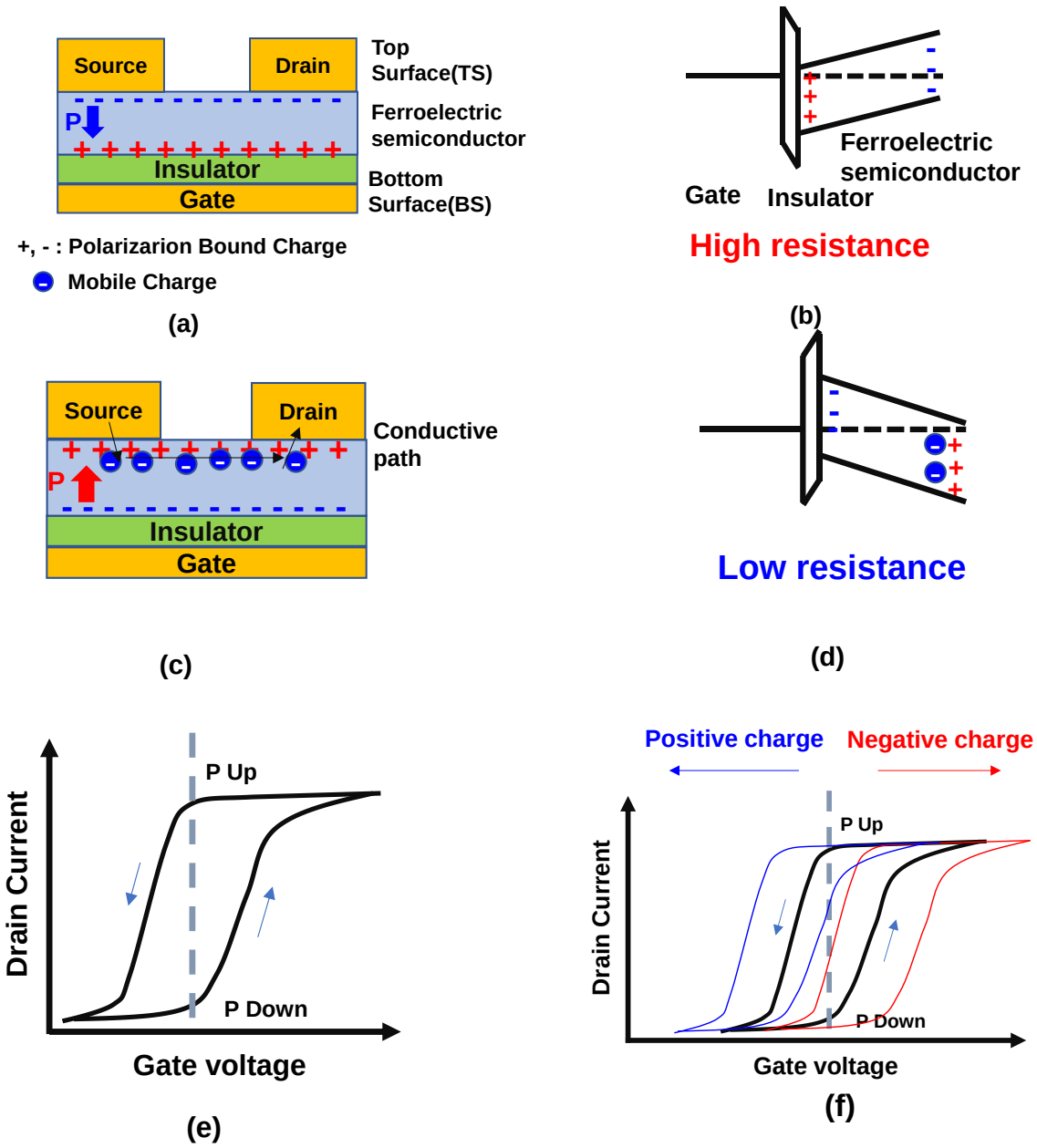

Fig. 1.2 Working mechanism of the ferroelectric semiconductor-FET. (a) Schematic of the cross-sectional structure in polarization down, (b) Band diagram in polarization down, (c) Schematic cross-sectional structure in polarization up, (d) Band diagram in polarization up, (e) I_d-V_g curve, (f) Effect of the fixed charge states at the interface. [1-10]

1.2 $Al_{1-x}Sc_xN$ for TFT applications

One of the material candidates for the ferroelectric semiconductor channel is $Al_{1-x}Sc_xN$. $Al_{1-x}Sc_xN$ is an alloy between AlN with its crystal structure of the wurtzite and its lattice constants of a=3.112 Å, c=4.982 Å [1-11] and ScN with its crystal structure of the rock-salt and its lattice constant of 4.501 Å, [1-12] where a and c are the lattice parameters of the a-axis and c-axis, respectively. The crystal structure of ScN is generally rock-salt, however, the first principle calculation predicted that the existence of the metastable wurtzite ScN and the alloy of Sc-(Al, Ga, In)-N can be realized. [1-13]

In 2009, Akiyama *et al*. reported that the four times larger piezoelectric coefficient of $Al_{1-x}Sc_xN$ compared to AlN. [1-14] Generally, the piezoelectric materials with higher Curie temperature (T_C) show the lower piezoelectric coefficient, but $Al_{1-x}Sc_xN$ can overcome this trade-off relationship. Since then, $Al_{1-x}Sc_xN$ films have attracted attention for high-sensitive piezoelectric sensors and the filters because of their high piezoelectric coefficient [1-14~1-17] with a high-temperature (500°C) tolerance. [1-15] By incorporating ScN into AlN, the distortion of the lattice structure from the wurtzite towards the cubic may be caused due to the difference in the lattice structure between AlN and ScN. As a result, the chemical bonding becomes soft, indicating that $Al_{1-x}Sc_xN$ easily causes the atomic and the lattice displacement for the same strain. [1-18] Therefore, $Al_{1-x}Sc_xN$ shows high piezoelectric properties. As an increase in the Sc composition of $Al_{1-x}Sc_xN$, the c/a ratio decrease, and the energy landscape of the cations are flattened, which facilitates the movement of cations and increases piezoelectricity. [1-19]

In recent years, the ferroelectricity of $Al_{1-x}Sc_xN$ has been attracting attention. The $Al_{1-x}Sc_xN$ film has two stable states of III-polar and N-polar as the same as the AlN film and the polarities can be switched by an external electric field as shown in fig. 1.3. [1-18] The ferroelectric functionality of $Al_{1-x}Sc_xN$ was predicted by the density functional theory calculation in 2013, [1-20] and the recent works have experimentally demonstrated that the $Al_{1-x}Sc_xN$ films exhibit ferroelectric properties with a box-like high remnant polarization

(P_r) of over 100 μC/cm^2. [1-9] Many conventional oxide-based ferroelectric films suffer from the size-effect, which means the ferroelectricity degrades as its thickness thinner. [1-21~1-23] On the other hand, $Al_{1-x}Sc_xN$ retains the ferroelectricity with its thickness of 9 nm. [1-19] Also, it is reported that the breakdown field of $Al_{1-x}Sc_xN$ film of 4.5 MV/cm was kept constant in the film thickness range from 50 to 20 nm. [1-24] Thanks to these advantages, $Al_{1-x}Sc_xN$ became a promising material for ferroelectric memory applications including ferroelectric-FETs.

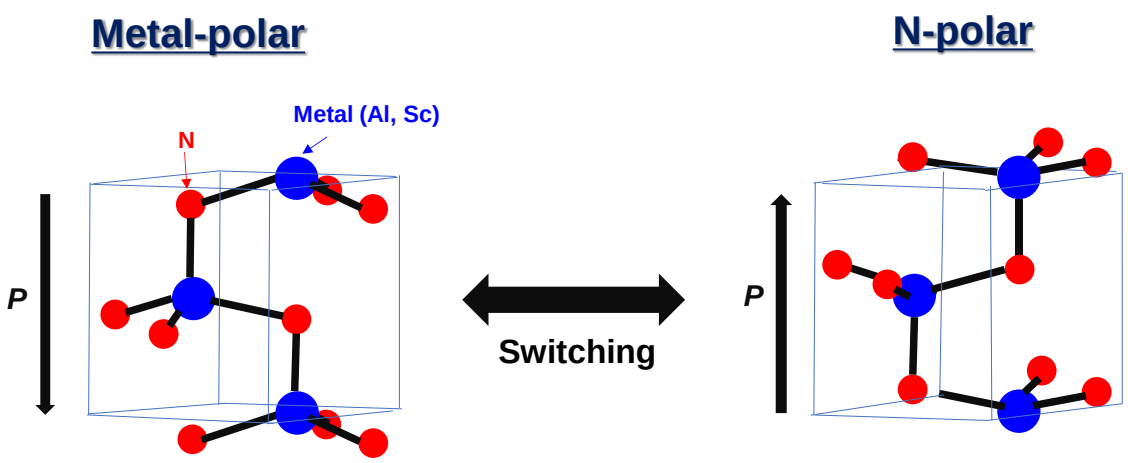

Fig. 1.3 Atomic locations of $Al_{1-x}Sc_xN$ corresponding to the polarization states. [1-9]

For mass production, it is an important factor whether the $Al_{1-x}Sc_xN$ film can be etched by a reactive ion etching process (RIE). The wurtzite $Al_{1-x}Sc_xN$ film is mainly composed of AlN composition. The AlN film commonly etches by the inductively coupled plasma (ICP) etching with Cl_2 or Cl_2/BCl_3 gas chemistry. [1-25] In the same manner, $Al_{1-x}Sc_xN$ etching by ICP-RIE with Cl_2 based gas chemistry is reported. [1-26] Table 1.2 shows the dissociation energy of the various bonds related to the $Al_{1-x}Sc_xN$ etching. [1-27] In the plasma process, the reaction proceeds to form a large energy bond. The surface oxide

layer AlO impedes the progress of the etching reaction of forming the volatile Al-Cl bond in the Cl_2 chemistry RIE process. By adding the BCl_3, the surface AlO layer is removed by forming the B-O bond, and the etching of AlN is proceeding smoothly.

Table 1.2 Dissociation energy of various bonds related to $Al_{1-x}Sc_xN$ etching.

bond	Dissociation energy(kJ/mol)	bond	Dissociation energy(kJ/mol)	bond	Dissociation energy(kJ/mol)
B-O	809	Al-Cl	502	Sc-O	671.4±1.0
B-N	377.9±8.7	Al-O	501.9±10.6	Sc-N	464±84
		Al-N	368±15	Sc-Cl	331
		Al-Al	140.5±1.8	Sc-Sc	163±21

The bandgap of $Al_{1-x}Sc_xN$ films can be expressed as $E_g(x)= -9.5x+6.2$ (eV), under the Sc composition of $0<x<0.34$. [1-28] Thus, $Al_{1-x}Sc_xN$ films can be considered as one of the nitride semiconductors. Once we can control the carrier charge types of the $Al_{1-x}Sc_xN$ films for source and drain, CMOS TFT with ferroelectric $Al_{1-x}Sc_xN$ channel can be realized, which opens a wide range of unique applications.

1.2.1 BEOL transistor

$Al_{1-x}Sc_xN$ films that show ferroelectric characteristics can be deposited at a relatively low temperature of 400°C. [1-9, 1-19, 1-24] This feature gives the $Al_{1-x}Sc_xN$ to be used as transistors manufactured in low-temperature processes. Table 1.3 shows a comparison of the channel materials of TFT. [1-29~1-36] Poly-Si TFT has already realized n-type and p-type conductions. With its bandgap of 1.1 eV, the ρ_c can be small and a high current density (J) can be obtained at the cost of low breakdown voltage. Ge-TFT is a promising candidate to overcome the Si scaling limit due to its higher mobility than that of Si.

However, the formation of the high-quality interface of Ge/Ge oxide is difficult due to the chemically and thermally instability of Ge oxide. [1-29, 1-30] Recently, the In-Ga-Zn-O (IGZO) TFT has attracted attention as BEOL-transistor because of its advantages such as the low off leakage current, [1-31] with a high breakdown voltage. [1-32] However, IGZO-TFT has several disadvantages. Firstly, the ρ_c is relatively high due to its wide bandgap. Secondly, IGZO-TFT suffers from the effective channel length shortening caused by the reduction reaction between IGZO and metal electrodes. [1-33] And finally, only n-type conduction is realized, [1-34] limiting the use of IGZO-TFT for CMOS circuit.

$Al_{1-x}Sc_xN$-TFT can be estimated to have similar properties (low off-leakage current, high breakdown voltage, high ρ_c) to IGZO-TFT due to its similar bandgap values. However, there is a possibility that n-type/p-type conduction can be obtained with a high tolerance to the thermal budget.

Table 1.3 Comparison of channel materials for TFT.

	Poly Si	Poly Ge	OS(IGZO)	$Al_{1-x}Sc_xN$
Bandgap (eV)	1.1	0.66	3.2	4.2(x=0.2)
Process Temp.(°C)	~500	~500	RT~400	~400 (unknown for doping)
CMOS Fabrication	○	○	× n-type only	? ?
Mobility (cm^2/Vs)	120	140	10~30(IGZO)	? ?
Memory function	By circuit	By circuit	By circuit	Ferroelectricity
Features	・High current density ・Low breakdown voltage	・High current density ・Low breakdown voltage	・Low leakage current ・High breakdown voltage ・Poor thermal tolerance (Form O vacancy) ・Low current density	・Low leakage current ・High breakdown voltage ・Thermally stable ・High ρ_c due to wide bandgap

OS: oxide semiconductor

1.2.2 Ferroelectric semiconductor-FET [1-10]

As a non-volatile memory application, it has been demonstrated that a field-effect transistor using a ferroelectric semiconductor material as a channel. [1-10] Si *et al.* reported that the ferroelectric semiconductor-FET using the two-dimensional ferroelectric semiconductor α-In_2Se_3 as a channel. $Al_{1-x}Sc_xN$ is a promising candidate for channel material of ferroelectric semiconductor-FET due to its several advantages of the large P_r, and the high breakdown voltage.

1.2.3 Comparison for the ferroelectric semiconductor materials

Table 1.4 shows the comparison of the ferroelectric semiconductor materials. [1-9, 1-10, 1-37~1-43] From the viewpoint of application to the non-volatile memory, α-In_2Se_3 is promising material compared to $Cd_{1-x}Zn_xTe$ or $Zn_{1-x}Li_xO$ because of its high P_r and ferroelectricity even 10nm thickness. However, since α-In_2Se_3 is a two-dimensional material, there is an issue of the application for the channel material of 3D devices. The $Al_{1-x}Sc_xN$ film has many advantages such as the larger P_r than α-In_2Se_3, ferroelectricity even in a thin film of about 9 nm, the large bandgap, and no restriction of the growth substrate.

Table 1.4 Comparison of the ferroelectric semiconductor materials.

	$Cd_{1-x}Zn_xTe$	$Zn_{1-x}Li_xO$	α-In_2Se_3	$Al_{1-x}Sc_xN$
Bandgap (eV)	1.53	3.2	1.39	4.2(x=0.2)
Process Temp.(°C)	600~	500	540~670	RT~400
n/p type conduction	○ n-type : In, I p-type : P (CdTe)	n-type	unknown	unknown
P_r (μC/cm²)	0.6(x=0.04)	0.09(x=0.25, 300nm) 0.044(x=0.3, bulk)	25 (sim)	100
Thickness scaling < 100nm	Bulk (900μm)	△300nm	○ 10nm	○ 9nm
Features	p-type, (100 cm²/Vs)	・Unstable resistance for impurities	・2D-material ・Growth on graphene or fluorophlogopite mica ([$KMg_3(AlSi_3O_{10})F_2$]) is required.	・Thermally stable ・Large P_r ・No restriction of growth sub.

1.3 Issues of applying $Al_{1-x}Sc_xN$ for the channel of BEOL transistor or ferroelectric semiconductor-FET

To apply $Al_{1-x}Sc_xN$ for the channel of BEOL transistor or ferroelectric semiconductor-FET, there are some issues. First, n-type and/or p-type conduction of the $Al_{1-x}Sc_xN$ film is required. Also, the reduction of the ρ_c and the increase in the channel mobility are required to obtain a large on-current. Besides, it is necessary to form a good interface with the insulator. This study focused on the realization of n-type conduction and the reduction of the ρ_c.

1.3.1 Realization of n-type and/or p-type conduction of $Al_{1-x}Sc_xN$

To date, there are no reports of achieving the n-type or p-type conduction of $Al_{1-x}Sc_xN$ film. As Si atoms are commonly used as n-type dopants of AlGaN [1-44~1-48] and AlN [1-49~1-52], the dopant is also a promising candidate for the donor impurities of $Al_{1-x}Sc_xN$ films. Mg is a promising candidate for the acceptor impurities because Mg atoms are used as p-type dopants of AlGaN [1-53, 1-54], AlN [1-55], and ScN [1-56].

Table 1.5 Typical donor and acceptor impurities of AlN and ScN films.

	AlN	ScN
Crystal structrue	Wurtzite	Rock-salt
n-type	Si	-
p-type	Mg	Mg

1.3.2 Reduction of the contact resistance of $Al_{1-x}Sc_xN$

The ρ_c based on the thermionic-emission (TE) model can be expressed in the following equation: [1-57, 1-58]

$$\rho_c = \frac{k}{q\,A^*\,T} \exp\left(\frac{q\,\phi_B}{k\,T}\right) , \qquad (1.1)$$

where q is the elementary charge, A^* is the effective Richardson constant, k is the Boltzman's constant, T is the absolute temperature, and ϕ_B is the Schottky barrier height, respectively. With a high doping level, the ρ_c based on the thermionic field emission (TFE) model can be expressed in the following equation: [1-57, 1-58]

$$\boldsymbol{\rho_c = \frac{k\sqrt{E_{00}}}{qA^*T\sqrt{\pi(\phi_B + u_f)}}\, cosh\left(\frac{E_{00}}{kT}\right) coth\left(\frac{E_{00}}{kT}\right) exp\left(\frac{\phi_B + u_f}{E_0} - \frac{u_f}{kT}\right)} \qquad (1.2)$$

$$\boldsymbol{E_0 = E_{00}\, coth\left(\frac{E_{00}}{kT}\right)} \qquad (1.3)$$

$$\boldsymbol{E_{00} = \frac{q\hbar}{2}\sqrt{\frac{N}{m^*_{tun}\mathcal{E}_s}}} \qquad (1.4)$$

$$\boldsymbol{A^* = \frac{M4\pi m^* q k^2}{h^3}} \qquad (1.5)$$

, where u_f is the Fermi level to the band edge, N is the carrier concentration, E is the electric field in an insulator, ε_s is the permittivity of the semiconductor, m^* is the effective mass, m^*_{tun} is the tunneling effective mass, and M is the number of equivalent ellipsoids corresponding to the minimum tunneling effective mass, respectively.

With a higher doping level, the ρ_c based on the field emission (FE) model can be expressed in the following equation: [1-57, 1-58]

$$\rho_c \propto exp\left\{\frac{2\sqrt{\mathcal{E}_s\, m^*}}{\hbar}\left(\frac{\phi_B}{N}\right)\right\} , \qquad (1.6)$$

where $\hbar$ is the Dirac's constant. These formulas indicate that lowering the ϕ_B and increasing in the N are effective to obtain the low ρ_c as shown in fig. 1.4. However, many semiconductor materials suffer from the Fermi-level pinning, [1-59~1-63] suggest that the ϕ_B

cannot be lowered by optimizing the ϕ_M of the electrode material. In such a case, it is necessary to select another method such as increasing the N of the $Al_{1-x}Sc_xN$ film for reducing the ρ_c.

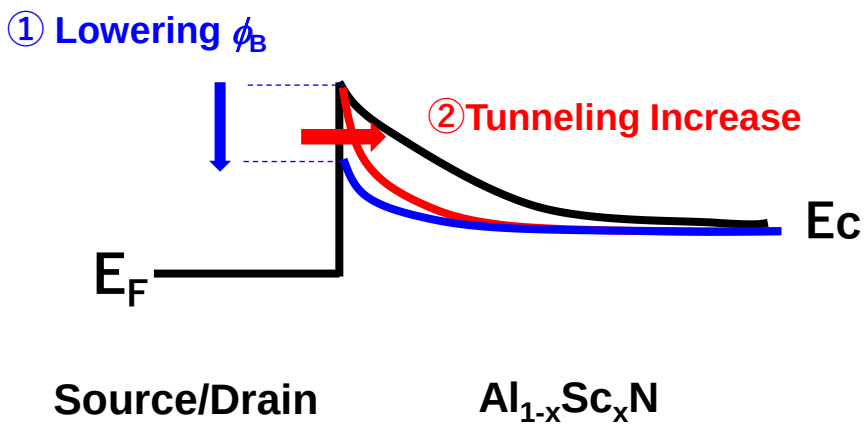

Fig. 1.4 Schematic band diagram at the interface between source/drain electrode and $Al_{1-x}Sc_xN$ film.

Here, a large leakage current of the $Al_{1-x}Sc_xN$ capacitor was reported. [1-64] This high leakage current in the $Al_{1-x}Sc_xN$ film can, in turn, be used for low Ohmic contact resistance. Therefore, clarification of the origin of the high leakage current is important.

The target value of the ρ_c is set to 1×10^{-4} Ωcm^2. For liquid crystal application, the required on-current of TFTs is the order of 1×10^{-6} A. When displaying a moving image, rewriting in the cells within 16 msec is required. If one line consists of 1080 pixels, one cell is required to be rewritten within about 15 μsec (16 msec/1080). Assuming that the capacitance to be rewritten is 5 pF, the required current is 3.3×10^{-7} A (5 pF/15 μsec).

Figure 1.5 shows the resistance model in the $Al_{1-x}Sc_xN$-FET. The total resistance (R_{on}) of the $Al_{1-x}Sc_xN$-FET is expressed as the following equation:

$$R_{on} = 2\,\rho_C + R_{ch} \quad , \qquad (1.7)$$

where R_{ch} is the channel resistance. In the linear region and low V_d case, the R_{ch} and the drain current I_d are expressed as (1.8) and (1.9). [1-65]

$$\frac{1}{R_{ch}} = \mu_{eff}\, C_{ox}\, \frac{W}{L}\,(V_g - V_{th}) \quad , \qquad (1.8)$$

$$I_d = \frac{V_d}{(R_{ch} + 2\rho_c)} \, , \qquad (1.9)$$

where μ_{eff} is the effective mobility, W is the channel width, L is the channel length, and V_{th} is the threshold voltage, respectively.

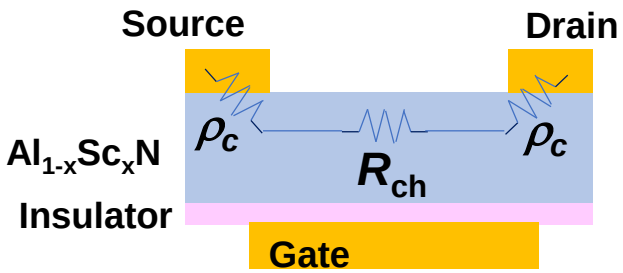

Fig. 1.5 Resistance model of the $Al_{1-x}Sc_xN$-TFTs.

Figure 1.6 shows the ρ_c dependence of the I_d calculated by eq. (1.8) and eq. (1.9) as a function of L. When the ρ_c is lower than 1×10^{-4} Ωcm^2, the I_d of 1×10^{-6} A can be obtained.

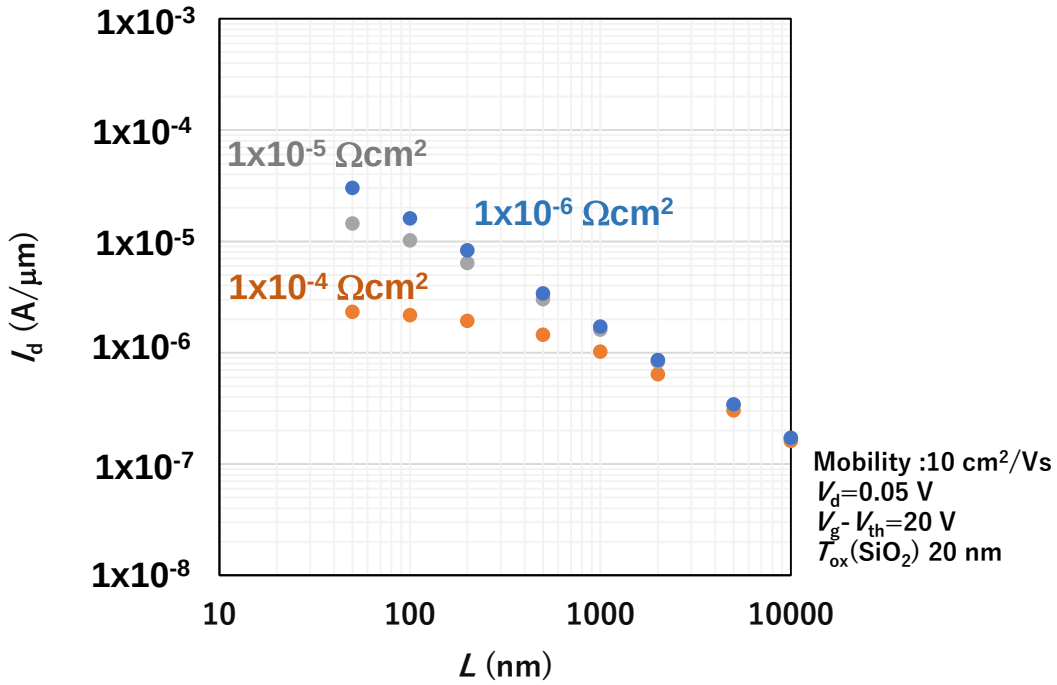

Fig. 1.6 ρ_c dependence of I_d as a function of L.

1.4 Objective of this thesis

The purpose of this study is the extraction of band alignment of metal/$Al_{1-x}Sc_xN$ interface and propose a guideline and demonstrate the n-type conduction for low Ohmic contact resistance. Figure 1.7 shows the outline of this thesis. In chapter 1, the feature of $Al_{1-x}Sc_xN$, the proposal of a new device using $Al_{1-x}Sc_xN$ as the channel, and how to realize it are summarized. In chapter 2, the physical and electrical characterization methods are described. In chapter 3, the extraction results of the band alignment at the metal/$Al_{0.78}Sc_{0.22}N$ are described. In chapter 4, the achievement of n-type conduction of $Al_{1-x}Sc_xN$ by Si ion doping and the properties of n-type $Al_{1-x}Sc_xN$ are described. In chapter 5, the issue of Si-doped $Al_{1-x}Sc_xN$ films, "sheet resistance instability" is described and its solution is proposed. In chapter 6, the summary and the future perspective of this thesis are described.

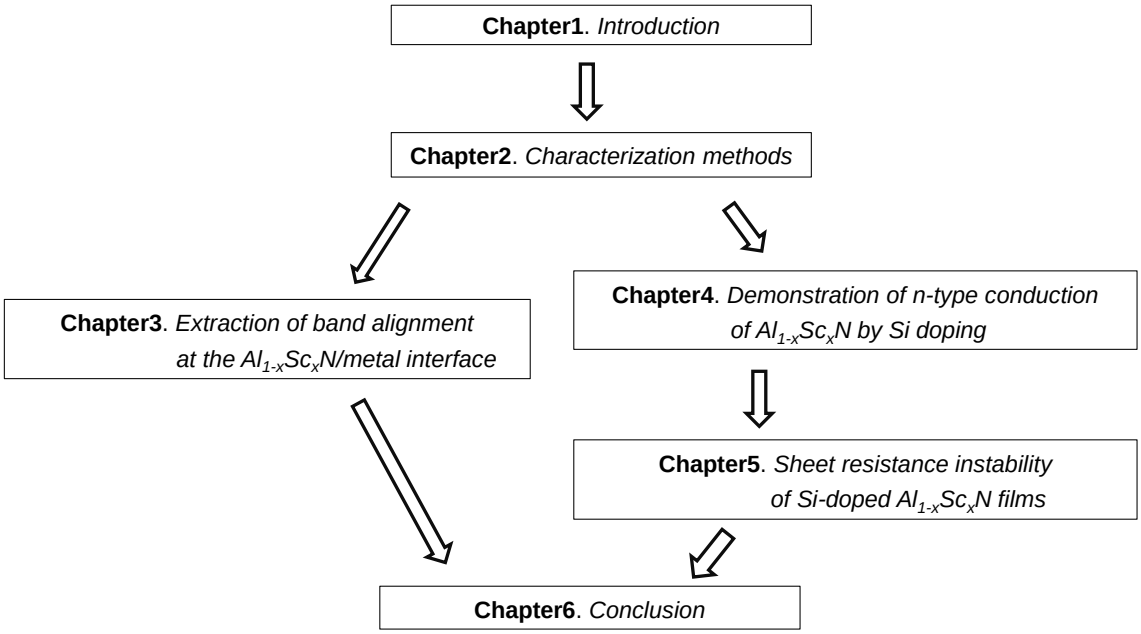

Fig. 1.7 Outline of this thesis.

References

[1-1] T. Naito, T. Ishida, T. Onoduka, M. Nishigoori, T. Nakayama, Y. Ueno, Y. Ishimoto, A. Suzuki, W. Chung, R. Madurawe, S. Wu, S. Ikeda, and H. Oyamatsu, Tech. Dig. VLSI, 2010, p. 219.

[1-2] S. Jeon, ECS Transactions, **64**, 175 (2014).

[1-3] https://www.j-display.com/english/technology/jdinew/ultralowp.html

[1-4] N. A. Clark and S. T. Lagerwall, Appl. Phys. Lett., **36**, 899 (1980).

[1-5] K. Kondo, H. Takezoe, A. Fukuda and E. Kuze, Jpn. J. Appl. Phys., **22**, L85 (1983).

[1-6] https://en.wikipedia.org/wiki/Ferroelectric_liquid_crystal_display

[1-7] https://www.jstage.jst.go.jp/article/yukigoseikyokaishi1943/47/6/47_6_568/_pdf

[1-8] https://www.fujitsu.com/downloads/JP/archive/imgjp/jmag/vol49-3/paper07.pdf

[1-9] S. Fichtner, N. Wolff, F. Lofink, L. Kienle, and B. Wagner, J. Appl. Phys., **125**,

114103 (2019).

[1-10] M. Si, A. K. Saha, S. Gao, G. Qiu, J. Qin, Y. Duan, J. Jian, C. Niu, H. Wang, W. Wu, S. K. Gupta, P. D. Ye, Nat. Electron., **2**, 580 (2019).

[1-11] W. M. Yim, E. J. Stofko, P. J. Zanzucchi, J. I. Pankove, M. Ettenberg, and S. L. Gilbert, J. Appl. Phys., **44**, 292 (1973).

[1-12] Z. Gu, J. Pomeroy, M. Kuball, and D. W. Coffey, J. Mater. Sci-Mater. Electron., **15**, 555 (2004).

[1-13] N. Takeuchi, Phys. Rev., B **65**, 045045204 (2002).

[1-14] M. Akiyama, T. Kamohara, K. Kano, A. Teshigahara, Y. Takeuchi, and N. Kawahara, Adv. Mater., **21**, 593 (2009).

[1-15] M. Akiyama, K. Kano, and A. Teshigahara, Appl. Phys. Lett., **95**, 162107 (2009).

[1-16] F. Tasnádi, B. Alling, C. Höglund, G. Wingqvist, J. Birch, L. Hultman, and I. A. Abrikosov, Phys. Rev. Lett., **104**, 137601 (2010).

[1-17] S. Barth, H. Bartzsch, D. Gloess, P. Frach, T. Herzog, S. Walter, and H. Heuer, IEEE trans. Ultrason. Ferroelectr. Freq. Control, **61**, 1329 (2014).

[1-18] D. Jena, R. Page, J. Casamento, P. Dang, J. Singhal, Z. Zhang, J. Wright, G. Khalsa, Y. Cho, and H. G. Xing, J. Jpn. Appl. Phys., **58**, SC0801 (2019).

[1-19] S. Yasuoka, T. Shimizu1, A. Tateyama, M. Uehara, H. Yamada, M. Akiyama, Y. Hiranaga, Y. Cho, and H. Funakubo, J. Appl. Phys., **128**, 114103 (2020).

[1-20] S. Zhang, D. Holec, W. Y. Fu, C. J. Humphreys, and M. A. Moram, J. Appl. Phys., **114**, 133510 (2013).

[1-21] D. J. Kim, J. Y. Jo, Y. S. Kim, Y. J. Chang, J. S. Lee, Jong-Gul Yoon, T. K. Song, and T. W. Noh, Phys. Rev. Lett., **95**, 237602 (2005).

[1-22] P. Maksymovych, M. Huijben, M. Pan, S. Jesse, N. Balke, Ying-Hao. Chu, H. J. Chang, A. Y. Borisevich, A. P. Baddorf, G. Rijnders, D. H. A. Blank, R. Ramesh, and S. V. Kalinin, Phys. Rev., B **85**, 014119 (2012).

[1-23] A. G. Zembilgotov, N. A. Pertsev, H. Kohlstedt, and R. Waser, J. Appl. Phys., **91**,

2247 (2002).

[1-24] S. Tsai, T. Hoshii, H. Wakabayashi, K. Tsutsui, and K. Kakushima, Int. Conf. on Solid State Devices and Materials, p17 (2020).

[1-25] A. P. Shah, A. A. Rahman, and A. Bhattacharya, Semicond. Sci. Technol., **30**, 015021 (2015).

[1-26] J. Wang, M. Park, S. Mertin, T. Pensala, F. Ayazi, and A. Ansari, J. Microelectromech. Syst., **29**, 741 (2020).

[1-27] J. R. Rumble (ed.) *CRC Handbook of Chemistry and Physics* (CRC Press, Boca Raton, FL, 2019) 100th ed.

[1-28] R. Deng, S. R. Evans, and D. Gall, Appl. Phys. Lett., **102**, 112103 (2013).

[1-29] K. Prabhakaran, F. Maeda, Y. Watanabe, and T. Ogino, Thin Solid Films, **369**, 289 (2000).

[1-30] K. Prabhakaran and T. Ogino, Surf. Sci., **325**, 263 (1995).

[1-31] H. Inoue, T. Matsuzaki, S. Nagatsuka, Y. Okazaki, T. Sasaki, K. Noda, D. Matsubayashi, T. Ishizu, T. Onuki, A. Isobe, Y. Shionoiri, K. Kato, T. Okuda, J. Koyama, and S. Yamazaki, IEEE J. Solid-State Circuits, **47**, 2258 (2012).

[1-32] K. Kaneko, N. Inoue, S. Saito, N. Furutake, and Y. Hayashi, Tech. Dig. VLSI, 2011, p. 120.

[1-33] J. Kataoka, N. Saito, T. ueda, T. Tezuka, T. Sawabe, and K. Ikeda, Jpn. J. Appl. Phys., **58**, SBBJ03 (2019).

[1-34] T. Kamiya and H. Hosono, NPG Asia Mater., **2**, 15 (2010).

[1-35] T. Nishimura, K. Kita, and A. Toriumi, Appl. Phys. Lett., **91**, 123123 (2007).

[1-36] K. Nomura, H. Ohta, A. Takagi, T. Kamiya, M. Hirano and H. Hosono, Nature, **432**, 488 (2004).

[1-37] D. J. Fu, J. C. Lee, S. W. Choi, S. J. Lee, T. W. Kang, M. S. Jang, H. I. Lee, and Y. D. Woo, Appl. Phys. Lett., **81**, 5207 (2002).

[1-38] D. B.-L. Cunff, B. Daudin, and J. L. Rouvière, Appl. Phys. Lett., **69**, 514 (1996).

[1-39] J. J. McCoy, S. K. Swain, J. R. Sieber, D. R. Diercks, B. P. Gorman, and K. G. Lynn, J. Appl. Phys., **123**, 161579 (2018).

[1-40] Dhananjay, J. Nagaraju, P. R. Choudhury, and S. B. Krupanidhi, J. Phys., D **39**, 2664 (2006).

[1-41] M. Joseph, H. Tabata, and T. Kawai, Appl. Phys. Lett., **74**, 2534 (1999).

[1-42] https://www.jstage.jst.go.jp/article/butsuri1946/53/4/53_4_282/_pdf/-char/ja

[1-43] Y. Zhou, D. Wu, Y. Zhu, Y. Cho, Q. He, X. Yang, K. Herrera, Z. Chu, Y. Han, M. C. Downer, H. Peng, and K. Lai, Nano Lett., **17**, 5508 (2017).

[1-44] I. Akasaki and H. Amano, Jpn. J. Appl. Phys., **36**, 5393 (1997).

[1-45] J. Hwang, W. J. Schaff, L. F. Eastman, S. T. Bradley, L. J. Brillson, D. C. Look, J. Wu, W. Walukiewicz, M. Furis, and A. N. Cartwright, Appl. Phys. Lett., **81**, 5192 (2002).

[1-46] M. L. Nakarmi, K. H. Kim, K. Zhu, J. Y. Lin, and H. X. Jiang, Appl. Phys. Lett., **85**, 3769 (2004).

[1-47] K. Takeda, M. Iwaya, T. Takeuchi, S. Kamiyama, and I. Akasaki, Jpn. J. Appl. Phys., **55**, 05FE02 (2016).

[1-48] A.Y. Polyakov, N.B. Smirnov, A.V. Govorkov, M.G. Mil'vidskii, J.M. Redwing, M. Shin, M. Skowronski, D.W. Greve,and R.G. Wilson, Solid-State Electron., **42**, 627 (1998).

[1-49] J. S. Harris, J. N. Baker, B. E. Gaddy, I. Bryan, Z. Bryan, K. J. Mirrielees, P. Reddy, R. Collazo, Z. Sitar, and D. L. Irving, Appl. Phys. Lett., **112**, 152101 (2018).

[1-50] Y. Taniyasu, M. Kasu, and T. Makimoto, Appl. Phys. Lett., **85**, 4672 (2004).

[1-51] Y. Taniyasu, M. Kasu, and T. Makimoto, Appl. Phys. Lett., **89**, 182112 (2006).

[1-52] C. R. Miskys, J. A. Garrido, C. E. Nebel, M. Hermann, O. Ambacher, M. Eickhoff, and M. Stutzmann, Appl. Phys. Lett., **82**, 290 (2003).

[1-53] T. Kinoshita, T. Obata, H. Yanagi, and S. Inoue, Appl. Phys. Lett., **102**, 012105 (2013).

[1-54] S.-R. Jeon, Z. Ren, G. Cui, J. Su, M. Gherasimova, J. Han, H.-K. Cho, and L. Zhou, Appl. Phys. Lett., **86**, 082107 (2004).

[1-55] K. B. Nam, M. L. Nakarmi, J. Li, J. Y. Lin, and H. Jiang, Appl. Phys. Lett., **83**, 878 (2003).

[1-56] B. Saha, M. Garbrecht, J. A. Perez-Taborda, M. H. Fawey, Y. R. Koh, A. Shakouri, M. Martin-Gonzalez, L. Hultman, and T. D. Sands, Appl. Phys. Lett., **110**, 252104 (2017).

[1-57] S. M. Sze and K. K. Ng, *Physics of Semiconductor Devices*, 3rd ed. (John Willy & Sons, 2007).

[1-58] K. K. NG and R. Liu, IEEE Trans. Electron Devices, **37**, 1536 (1990).

[1-59] S. Kurtin, T. C. McGill, and C. A. Mead, Phys. Rev. Lett., **22**, 1433 (1969).

[1-60] M. Schlüter, Phys. Rev., B **17**, 5044 (1978).

[1-61] T. Nishimura, K. Kita, and A. Toriumi, Appl. Phys. Lett., **91**, 123123 (2007).

[1-62] S. Wahid, N. Chowdhury, M. K. Alam, and T. Palacios, Appl. Phys. Lett., **116**, 213506 (2020).

[1-63] P. Bampoulis, R. V. Bremen, Q. Yao, B. Poelsema, H. J. W. Zandvliet, and K. Sotthewes, ACS Appl. Mater. Interfaces, **9**, 19278 (2017).

[1-64] S. Fichtner, N. Wolff, F. Lofink, L. Kienle, and B. Wagner, J. Appl. Phys., **125**, 114103 (2019)., suppl. material.

[1-65] Y. Taur and T. H. Ning, *Fundamentals of Modern VLSI Devices*, 2nd ed. (Cambridge University Press, 2009).

Chapter 2. Experimental methods

In this chapter, physical and electrical characterization methods are described.

2.1 Physical Characterizations of $Al_{1-x}Sc_xN$ film

2.1.1 X-ray photoelectron spectroscopy

X-ray photoelectron spectroscopy (XPS) is most widely used for surface analysis because it can identify the elements composed of the materials and evaluate not only the elemental composition but also their chemical state. Figure 2.1 shows the basic components of the XPS measurement system. [2-1] A sample is irradiated with a monochromatic X-ray to provoke the photoelectron effect. As a result, photoelectrons are emitted from the sample surface and are introduced into the detector through the input lens towards the energy analyzer for measuring the photoelectron energy distribution. With this configuration, the energy spectrum of the emitted photoelectron is obtained.

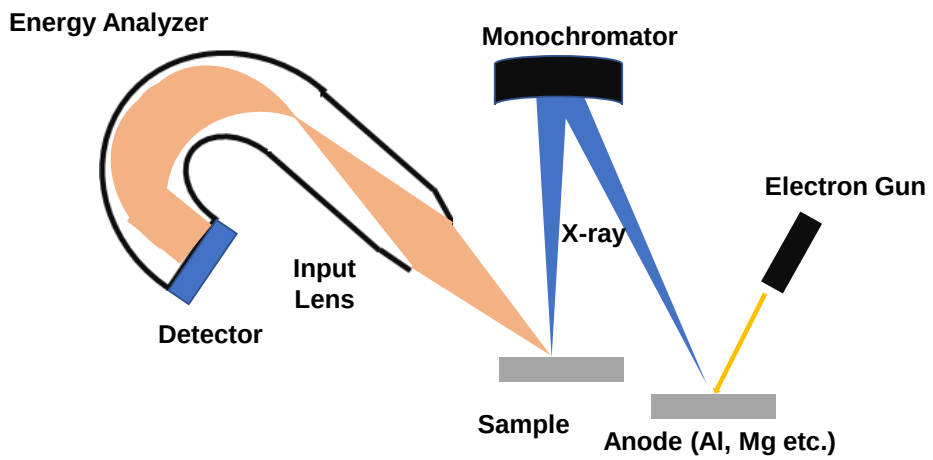

Fig. 2.1 Basic components of XPS measurement system.

Figure 2.2 shows the schematic of the photoemission process. In XPS analysis, the kinetic energy (E_k) of the emitted photoelectron is measured. The binding energy (E_b) is determined as the following equation:

$$E_b = h\upsilon - \phi_{work} - E_k \ , \qquad (2.1)$$

where $h\nu$ is the energy of irradiated X-ray, and ϕ_{work} is the instrument-specific work function. Here, the $h\nu$ is known, and the ϕ_{work} can be obtained from the reference measurement. Therefore, E_b is obtained by measuring the E_k. The chemical bonding states can be diagnosed by the energy shift of the E_b.

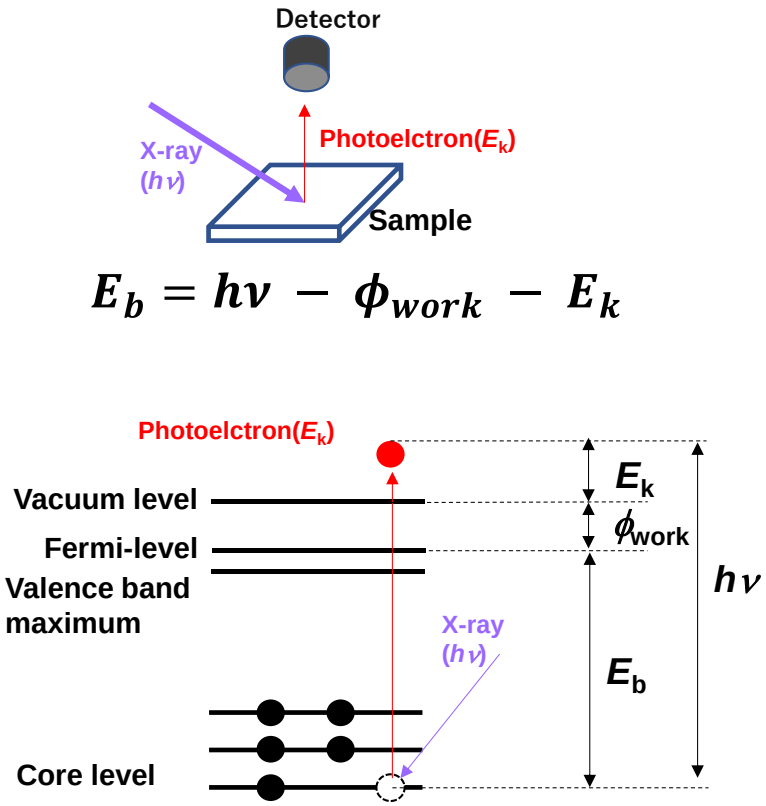

Fig. 2.2 Schematic of the photoemission process.

2.1.2 X-ray diffraction

X-ray diffraction (XRD) is commonly used for determining the crystal structure, crystal orientation, and crystal quality. X-ray irradiated into the crystal is diffracted into many specific directions following Bragg's law,

$$2d\ sin\theta = n\ \lambda, \qquad (2.2)$$

where d is the spacing between atom layers, θ is the incident angle of the X-ray, n is an integer multiple, and λ is the wavelength of the X-ray, respectively. When the difference path ($2d\sin\theta$) of X-rays diffracted on the different surfaces becomes $n\lambda$, the diffraction occurs, and the intensity of the outgoing X-ray increases as shown in fig. 2.3. By scanning the sample through a range of 2θ angles, the diffraction pattern is obtained (2θ-θ scan). Since the X-ray diffraction pattern is unique to each material, the identification of polycrystalline phases can be done.

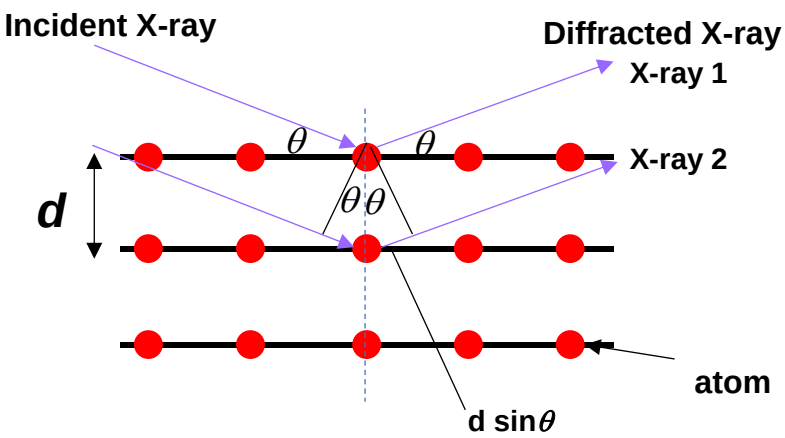

Fig. 2.3 Schematic of Bragg diffraction.

X-ray rocking curve (XRC) method is used to evaluate the crystal quality such as crystal distortion and defect. The 2θ is fixed at a specific diffraction position, and the θ slightly changed. The disorder of the crystal arrangement due to the distortion and the defect in the crystal causes a widening of the diffraction peak. Therefore, the crystal quality can be determined from the full-width at half-maximum (FWHM) of the diffraction peak.

2.1.3 Transmission electron microscope

Transmission electron microscopes (TEM) can observe microstructures with extremely high spatial resolution. Figure 2.4 shows the basic components of a TEM system. [2-2] An accelerated electron beam is irradiated to an ultra-thin sample and the electron beam is transmitted through the sample with atomistic interaction. The obtained image is the results of the interaction. The spatial resolution δ is given as

$$\boldsymbol{\delta} = \frac{\mathbf{0.61}\,\boldsymbol{\lambda}}{\boldsymbol{n\,sin\beta}} \quad , \qquad (2.3)$$

where λ is the wavelength of the electron beam, n is the refractive index of the medium, and β is the semi-angle of collection of the subtended angle from the lens. [2-3] From eq. (2.3), the spatial resolution can be improved to decrease the wavelength of the electron beam. Generally, the electron beam is accelerated at 100~200 keV for TEM analysis, the wavelength of the electron beam is about 0.0037 nm~0.0025 nm, leading to a high spatial resolution.

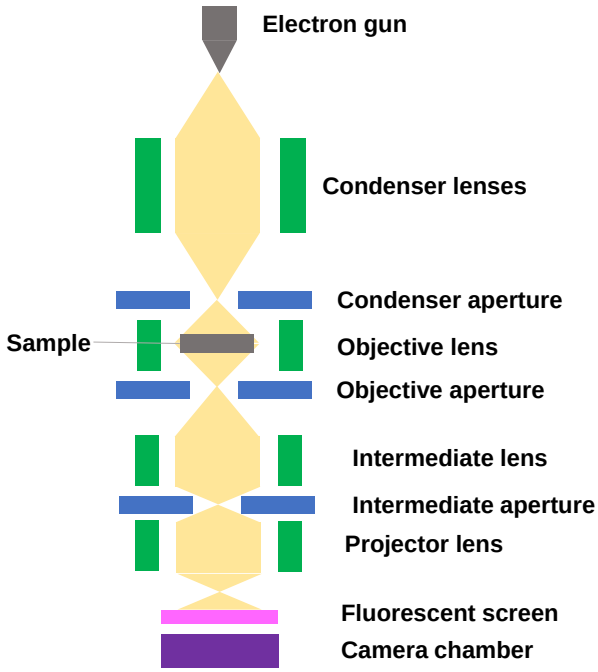

Fig. 2.4 basic components of TEM system.

2.2 Electrical Characterizations of $Al_{1-x}Sc_xN$ film

2.2.1 Extraction of the sheet resistance

The sheet resistance (R_s) of the semiconductor film is measured by the four-point probe method as shown in fig. 2.5. The resistivity (ρ) is expressed following equation: [2-4]

$$\rho = \frac{V}{I} W\ CF\ (\Omega\ cm), \qquad (2.4)$$

where V is a voltage measured between the inner two probes, I is the current through the outer two probes, W is a thickness of semiconductor film, and CF is a correction factor, respectively. The correction factor is determined by the ratio of d/s, where d is the diameter of the semiconductor sample, and s is the space of two probes. When the d/s is

over 20, *CF* can approximate about 4.54. Here, the R_s of the semiconductor film is given by the following equation.

$$R_s = \frac{V}{I}\ 4.54\ (\Omega/sq.) \qquad (2.5)$$

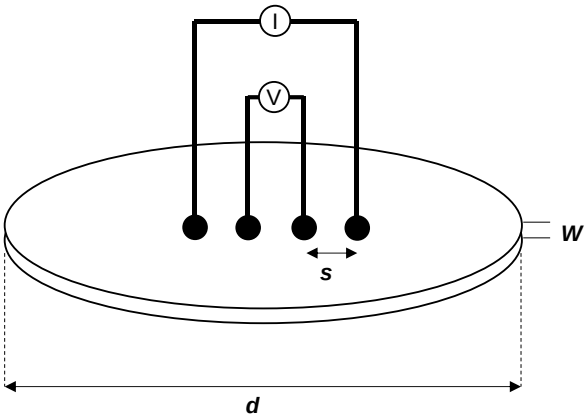

Fig. 2.5 Schematic of the four-point probe measurement.

2.2.2 Hall-effect measurement

Hall-effect measurement can evaluate a carrier type, the carrier concentration (*N*), and the Hall-mobility (μ_{Hall}) of the semiconductor. Figure 2.6 shows the schematic of the Hall-effect measurement. [2-5] When a magnetic field is applied vertically to the semiconductor in which a current is flowing, the magnetic field exerts a transverse force on a flowing electron, and the electron is accumulated to the one side of the semiconductor. As a result, an electric field (*E*) is established in the direction perpendicular to both the current and the magnetic field. When the *E* and magnetic field is balanced, producing a measurable voltage called a Hall-voltage (V_H) between the two sides of the semiconductor. Considering the n-type semiconductor, the V_H is expressed as the following equation, [2-4]

$$V_H = \frac{1}{e\,n}\frac{I\,B}{t} = R_H\,\frac{I\,B}{t}\ (V), \qquad (2.6)$$

where e is an elementary charge, n is a carrier concentration, I is current, B is the magnetic flux density, t is the thickness of the semiconductor, and R_H is the Hall coefficient, respectively.

The carrier type can be identified from whether the R_H is positive or negative. The n is obtained from the (2.6) equation because V_H, I, B, and t can be measured.

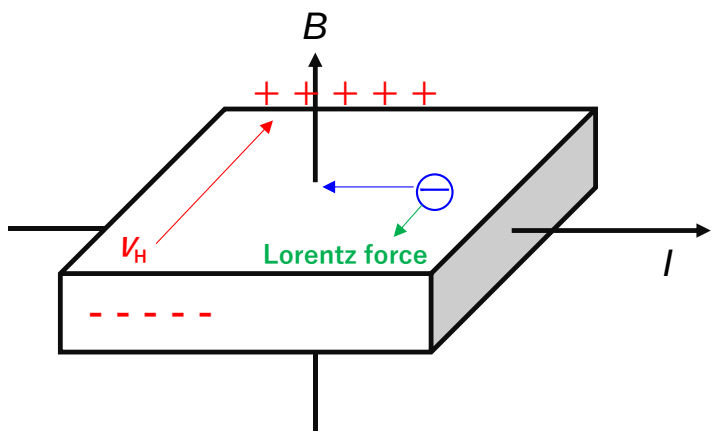

Fig. 2.6 Schematic of Hall-effect measurement.

2.2.3 Extraction of the contact resistance by transmission line model

In measuring the R_s by the four-point probe method, the four probes are used to minimize the effect of the contact resistance (ρ_c). However, the evaluation of the ρ_c is necessary to improve device performance. The transmission line model (TLM) method is commonly used to extract the ρ_c. Figure 2.7 shows the extraction of the ρ_c by the TLM method. The total resistance (R_T) of the measurement sample is expressed as (2.7). [2-6]

$$R_T = 2\rho_c + R_{semi} = 2\rho_c + \frac{d}{W}\,R_s\,, \qquad (2.7)$$

where d is the distance between two electrodes, W is the width, R_s is the sheet resistance

of semiconductor, and R_{semi} is the resistance of the semiconductor, respectively. Plotting the R_T measured by the samples with different d, the ρ_c can be obtained by the intersection to y-axis as shown in fig. 2.7 (c).

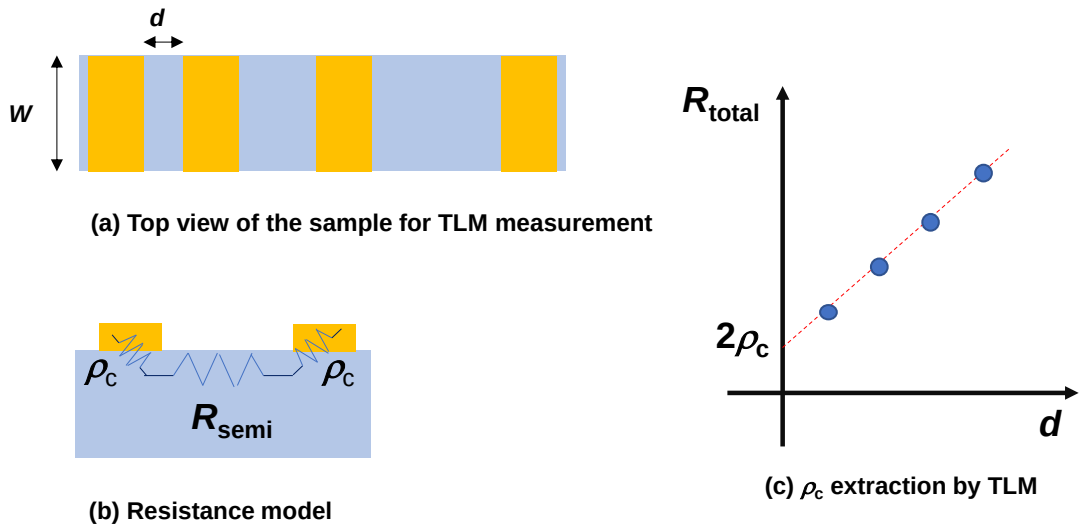

Fig. 2.7 Extraction of the ρ_c by the TLM method.

2.3 Summary

In this chapter, the physical and electrical characterization methods used in this thesis are briefly introduced.

References

[2-1] https://www.phi.com/surface-analysis-techniques/xps-esca.html

[2-2] http://www.biosciencenotes.com/transmission-electron-microscope-tem/

[2-3] N. Tanaka, *Densisen nano imeijingu* (nano-imaging using electron beam), (Uchida Rokakuho, 2009).

[2-4] S. M. Sze and M. K. Lee, *Semiconductor Devices Physics and Technology*, 3rd ed. (John Wiley & Sons, 2013).

[2-5] https://detail-infomation.com/hall-effect/

[2-6] http://tuttle.merc.iastate.edu/ee432/topics/metals/tlm_measurements.pdf

Chapter 3. Extraction of band alignment at $Al_{1-x}Sc_xN$/metal interface

Formation of the low ρ_c at the $Al_{1-x}Sc_xN$/electrode is required to improve the performance of the device which uses the $Al_{1-x}Sc_xN$ film as a channel. As described at "*1.3.2*", Schottky barrier height (ϕ_B) lowering is effective to reduce the ρ_c. At the n-type semiconductor and metal interface, the ϕ_B is lowered by using the metal with the low work function (ϕ_M). On the other hand, many semiconductor materials suffer from the Fermi-level pinning. [3-1~3-5] Therefore, it is important to know ϕ_B at the $Al_{1-x}Sc_xN$/metal interface.

As the bandgap (E_g) of $Al_{1-x}Sc_xN$ films is empirically expressed as $E_g(x)= -9.5x+6.2$ eV, under $0<x<0.34$, [3-6] $Al_{1-x}Sc_xN$ films with x from 0.2 to 0.3 exhibit E_g of 4.3 to 3.4 eV, respectively, and can be regarded as insulators with a wide bandgap. Besides, the valence band offset between $Al_{0.72}Sc_{0.28}N$ (E_g=3.5 eV) and TiN electrode is reported to be 1.8 eV, [3-7] therefore, the conduction band offset, or the ϕ_B, should be the order of 1.7 eV, which is generally high enough to suppress the leakage current. However, the leakage current through the $Al_{1-x}Sc_xN$ films is unexpectedly large, [3-8, 3-9] and the physical reason has not been clarified yet. [3-10] It is reported that the leakage current increases due to the microstructural change in the high-temperature (>400°C) grown $Al_{0.7}Sc_{0.3}N$ films. [3-11] However, a high leakage current is still reported with low-temperature (350°C) deposited $Al_{0.68}Sc_{0.32}N$ films. [3-12] This large leakage current in the $Al_{1-x}Sc_xN$ film can, in turn, be used for the low Ohmic contact resistance. To do this, we need to find the origin of the high leakage current.

I-V measurement is commonly used for the evaluation of the ϕ_B. At the Schottky contact interface, the leakage current density (J) based on the Schottky emission model is expressed as the following equation, [3-13]

$$J = A^* T^2 exp\left[-\frac{q}{k_B T}\left(\phi_B - \sqrt{\frac{qE}{4\pi\varepsilon_s\varepsilon_0}}\right)\right], \quad (3.1)$$

where A^* is the Richardson constant, T is the absolute temperature, k_B is the Boltzmann's

constant, q is the elementary charge, ϕ_B is the Schottky barrier height, E is the electric field, ε_s is the optical dielectric constant, and ε_0 is the vacuum permittivity, respectively.

On the contrary, J based on the Poole-Frenkel model is expressed as the following equation, [3-13]

$$J = qn_0\mu E\ exp\left[-\frac{q}{k_BT}\left(\phi_t - \sqrt{\frac{qE}{\pi\varepsilon_s\varepsilon_0}}\right)\right], \quad (3.2)$$

where n_0 is carrier density and μ is the effective mobility.

XPS measurement is also commonly used to determine the ϕ_B because it can evaluate the valence band level (E_v) and ϕ_M of metal directly. [3-14~3-19]. However, in the case of measure the ferroelectric film, the peak shift caused by the band bending due to the polarization in the ferroelectric film is reported. [3-20] This suggests that the accurate evaluation of the band structure of the ferroelectric film is difficult by XPS. Therefore, in this study, to determine the ϕ_B at the $Al_{1-x}Sc_xN$/metal more accurately, the leakage current analysis of the $Al_{0.78}Sc_{0.22}N$ capacitor was performed.

3.1 Experimental details

Metal-ferroelectric-metal (MFM) capacitors with a 50-nm-thick $Al_{0.78}Sc_{0.22}N$ layer are fabricated with either TiN or W top and bottom electrodes on the high conductive n^+ Si wafer. The thickness of the top and the bottom metal are both set to 30 nm. The sample fabrication process is as follows. The n^+ Si wafer was cleaned by a mixture of H_2SO_4 and H_2O_2 for 10 min, and 1% HF for 1min. Next, the 30nm-thick bottom electrode, the 50nm-thick $Al_{0.78}Sc_{0.22}N$ film, and the 30nm-thick top electrode were in-situ deposited on the n^+ Si wafer by reactive sputtering in Ar and N_2 mixture for $Al_{0.78}Sc_{0.22}N$ and TiN, and in Ar for W at a substrate temperature of 400°C. After that, the top electrode was patterned for the shape of a square with an area of 2.5×10^{-5} cm^2 by lithography and wet etching process of a mixture of 29% NH_4OH: H_2O_2:H_2O = 1:5:5. Figure 3.1 shows the sample fabrication

flow and table 3.1 shows the sputtering conditions. The films were characterized by X-ray diffraction (XRD) under a source of the X-ray of Cu$K\alpha$ with a divergence angle of 0.04° and the transmission electron microscope (TEM).

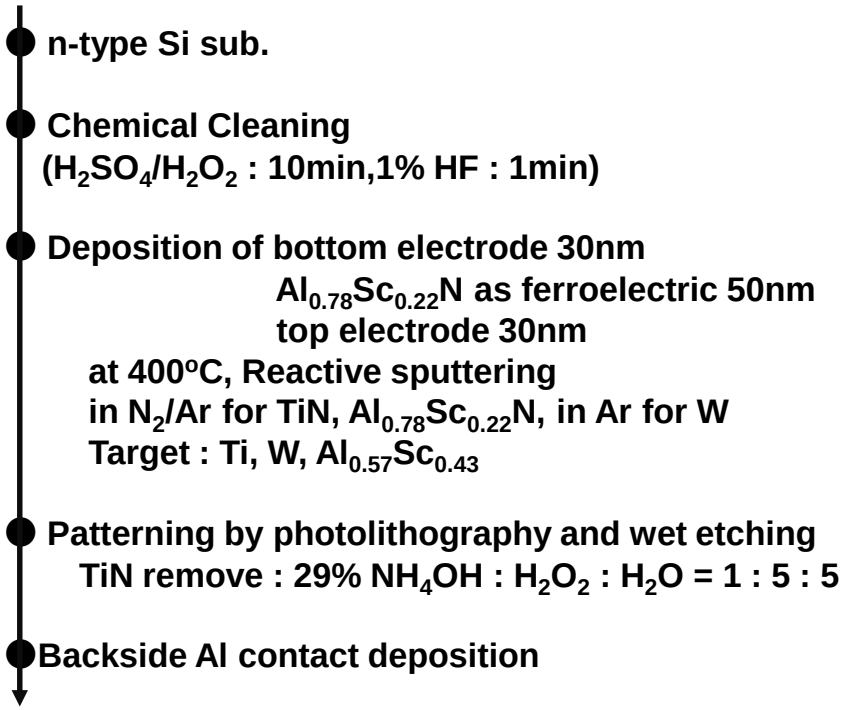

Fig. 3.1 Sample fabrication flow of the MFM capacitors.

Table 3.1 Details of the deposition conditions

	power (W)	Ar (sccm)	N_2 (sccm)	Pressure (Pa)	Temp. (°C)
$Al_{0.78}Sc_{0.22}N$	DC 300	5	10	0.7	400
TiN	RF 300	4	6	0.22	400
W	RF 150	7	-	0.55	400

Figure 3.2 (a) shows the bright-field TEM image near the interface between the $Al_{0.78}Sc_{0.22}N$ layer and the TiN electrode. From a closeup view of the image, we can see continuous lattice patterns toward the TiN layer with a sharp interface without any intermixing layer. However, a weak contrast with a thickness of about 2 nm in the $Al_{0.78}Sc_{0.22}N$ layer at the interface can be seen dimly. The integral of the brightness in the lateral direction is shown in fig. 3.2 (b), where we can see a small peak near the interface.

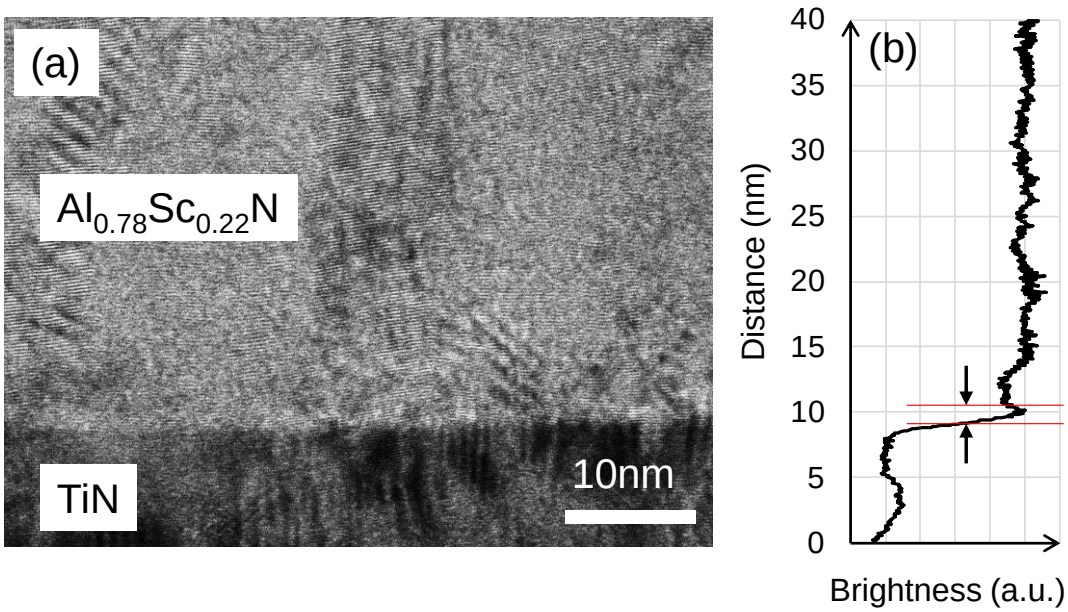

Fig. 3.2 (a) Bright-field TEM image near the interface between the $Al_{0.78}Sc_{0.22}N$ layer and the TiN electrode, and (b) Brightness profile to the vertical direction of the TEM image.

Figure 3.3 shows the XRD rocking curve spectra of the wurtzite (002) reflection of the $Al_{0.78}Sc_{0.22}N$ film on the TiN electrode shown in the red line and on the W electrode shown in the black line. The c-axis orientation was confirmed for both $Al_{0.78}Sc_{0.22}N$ films and a better full-width at half-maximum (FWHM) of 7.3° with the W electrode compared to 9.7° of the TiN electrode can be shown.

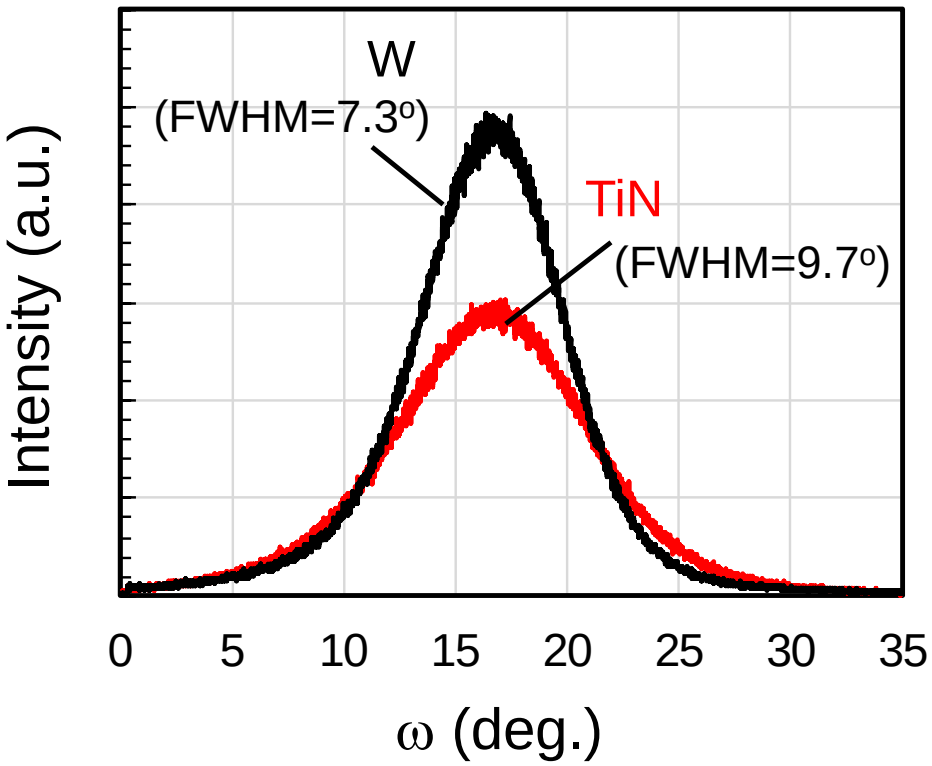

Fig. 3.3 X-ray rocking curve spectra of the $Al_{0.78}Sc_{0.22}N$ films deposited on the TiN electrode (shown in red line) and on the W electrode (shown in black line).

3.2 Leakage current analysis of $Al_{0.78}Sc_{0.22}N$ capacitors

Firstly, the variability of the leakage current within the sample was checked. Figure 3.4 shows the initial *J-V* characteristics of 7 capacitors of the TiN/$Al_{0.78}Sc_{0.22}N$/TiN sample. The leakage current showed good repeatability among the electrodes. From this result, we can confirm that the measured leakage current is not affected by the variability within the MFM capacitor.

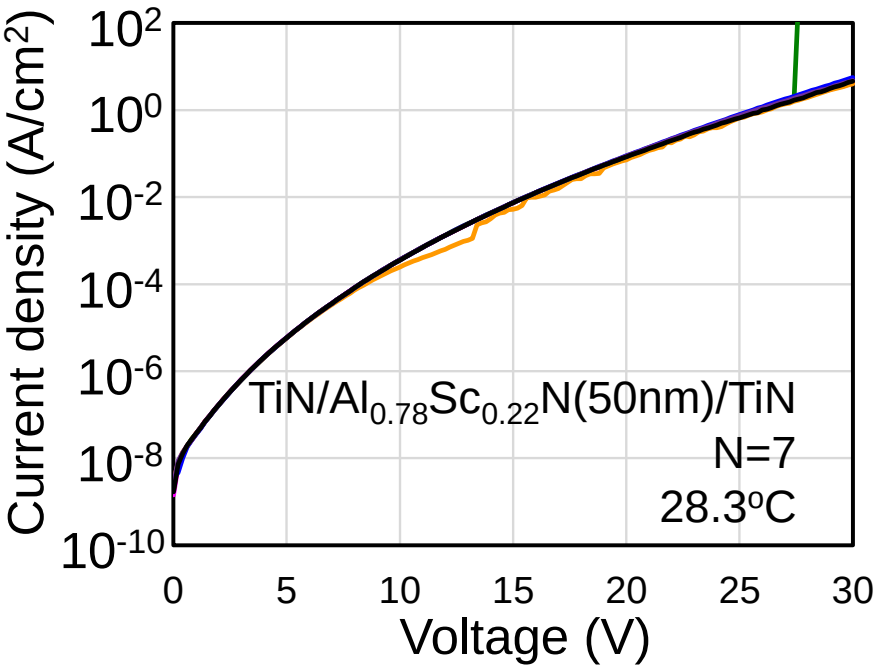

Fig. 3.4 *J-V* characteristics of 7 measurements of the TiN/$Al_{0.78}Sc_{0.22}N$/TiN capacitor.

The leakage current was measured with a measurement delay time of 0.1 s by applying a DC voltage to the top electrode. As the $Al_{0.78}Sc_{0.22}N$ layer is already poled in the downward direction, a positive voltage was first applied. [3-21] Figure 3.5 shows the J/T^2 on the $E^{0.5}$ characteristics of the TiN/$Al_{0.78}Sc_{0.22}N$/TiN capacitor measured at 40°C. The relationship of the J/T^2 on the $E^{0.5}$ characteristics shows good linearity, indicating that the leakage current conduction follows the Schottky emission model in the applied voltage

range. Therefore, the effect of grain boundary leakage current can be neglected. [3-22~3-24] The voltage sweeping sequence is as follows: firstly, a double voltage sweep was applied to the positive direction, from 0 to 30 V and back to 0 V (shown in black line), then to the negative direction from 0 to –30 V and back to 0 V (shown in blue line), finally to the positive direction again (shown in red line). At the first positive voltage sweep, the leakage current showed no difference between the forward and reverse sweeping, indicating that charge trapping to the $Al_{0.78}Sc_{0.22}N$ layer is negligible. When sweeping the voltage to the negative direction, a gradual increase in the leakage current higher than the expected Schottky emission model was observed in the E range from 3.8 to 4.2 MV/cm ($E^{0.5}$ from 1950 to 2060 $V^{0.5}/cm^{0.5}$) during the forward sweep. Above this electric field, the leakage current again followed the Schottky emission model but with a different slope and intercept. The leakage current during the reverse sweeping followed the same Schottky emission model level, indicating that there has been a change in the ϕ_B near the interface. The gradual increase in the leakage current at this region corresponds to the initial ferroelectric polarization switching of the $Al_{0.78}Sc_{0.22}N$ film. The electric field region for the gradual change in the leakage current was found to decrease at elevated temperature, shown in the inset of fig. 3.5, indicating that the gradual increase in the leakage current is a thermally activated process. During the final voltage sweep to the positive direction, the leakage current followed the same level for both forward and reverse sweeping, except for the small hump at 3.6 MV/cm (1900 $V^{0.5}/cm^{0.5}$) only observed during the forward sweep due to the ferroelectric switching. Further leakage current measurements either to the positive or negative direction result in the same leakage level, indicating that the ϕ_B is almost the same whether the polarization of $Al_{0.78}Sc_{0.22}N$ film is N-face or metal-face.

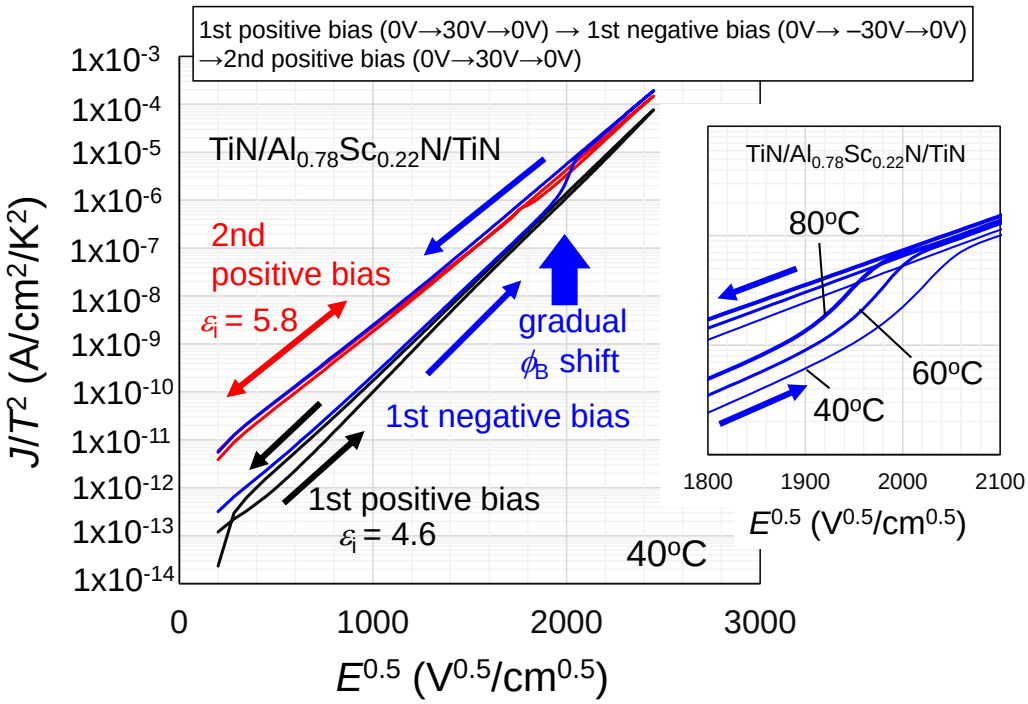

Fig. 3.5 J/T^2 on $E^{0.5}$ characteristics of the TiN/$Al_{0.78}Sc_{0.22}$N/TiN capacitor. The temperature dependence of the electric field region for the gradual change in the leakage current at the negative bias application was shown in the inset.

As for the W/$Al_{0.78}Sc_{0.22}$N/W capacitor, the same leakage current behavior can be observed before and after the initial switching. Figure 3.6 shows the J/T^2 on $E^{0.5}$ characteristics of the W/$Al_{0.78}Sc_{0.22}$N/W capacitor measured at 40°C. At the first voltage sweep to the positive direction, the leakage current showed no difference between the forward and reverse sweeping. And then, by applying the voltage to the negative direction, the leakage current showed a gradual increase during the forward sweep, and the leakage current kept the same level during the reverse sweeping. During the 2nd voltage sweep to the positive direction, the leakage current followed the same level for both forward and reverse sweeping. In this way, the same tendency of the leakage current can be seen in different electrode metals. This fact suggests that the behavior can be regarded as a

universal phenomenon for ferroelectric $Al_{1-x}Sc_xN$ films.

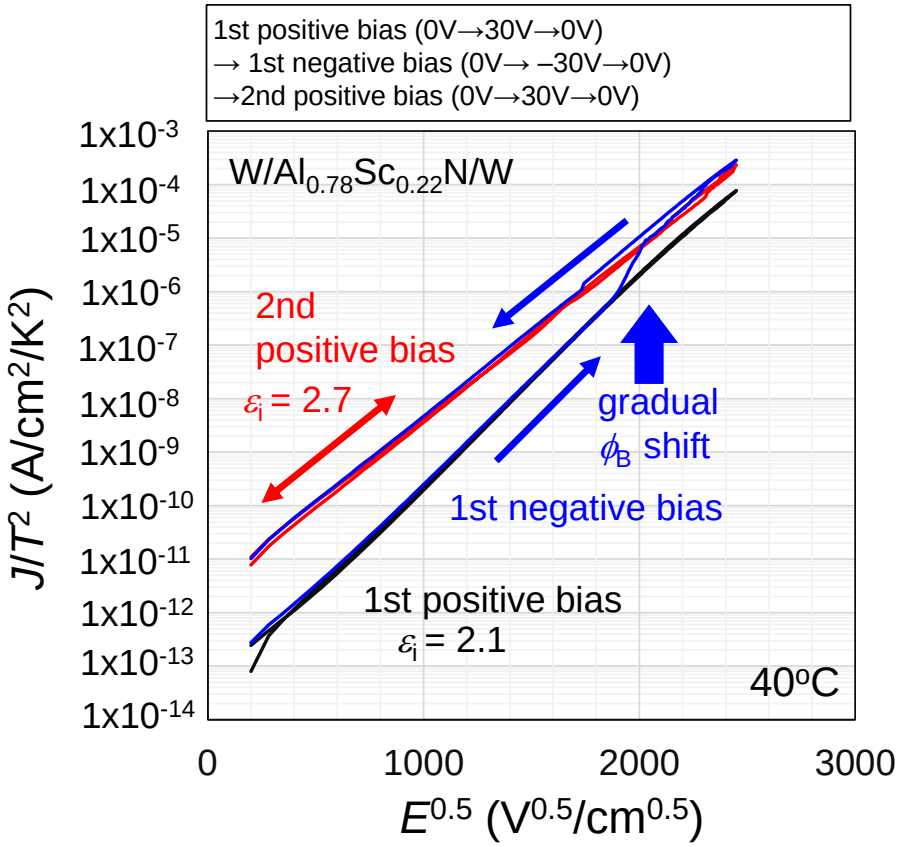

Fig. 3.6 J/T^2 on $E^{0.5}$ characteristics of the $W/Al_{0.78}Sc_{0.22}N/W$ capacitor measured at 40°C.

The change in the slope in fig. 3.5 and fig. 3.6 represents the change in the ε_i, where 4.6 and 5.8 were extracted for the slope before and after the initial switching of the $TiN/Al_{0.78}Sc_{0.22}N/TiN$ capacitor. The tendency is in good agreement with the dielectric constant of 18 and 21 before and after initial switching, respectively, extracted from capacitance-voltage measurement in the same voltage application sequence. [3-21] As for

the W/$Al_{0.78}Sc_{0.22}N$/W capacitor, the ε_i values were extracted of 2.1 and 2.7 before and after the initial switching, respectively.

From the intercept of the Schottky emission plot in fig. 3.5 and 3.6 with its temperature dependence, the ϕ_B can be extracted from each leakage current and is shown in fig. 3.7. A ϕ_B of 0.46 and 0.55 eV for TiN and W electrode, respectively, was changed to the same ϕ_B of 0.36 eV after the initial switching. The reason for the high leakage current for $Al_{1-x}Sc_xN$ ferroelectric capacitors may be due to this low effective ϕ_B and the further ϕ_B decrease by the initial ferroelectric polarization switching.

The A^* values, extracted from the intercept in fig. 3.7, were 5.3×10^{-7} and 1.5×10^{-5} $Acm^{-2}K^{-2}$ before initial switching and 6.1×10^{-7} and 1.4×10^{-6} $Acm^{-2}K^{-2}$ after the initial switching for TiN and W electrode, respectively. The A^* value kept the same value after further subsequent switching cycles. These values are far smaller than the value calculated from the theoretical value of A^* ($=4\pi m^* q k_B^2/h^3$) to be the order of 58 $Acm^{-2}K^{-2}$, [3-25~3-27] when citing a value of $m^*=0.48m_0$ for AlN films, [3-27] where h is the Plank's constant and m^* and m_0 are the effective electron and electron masses, respectively.

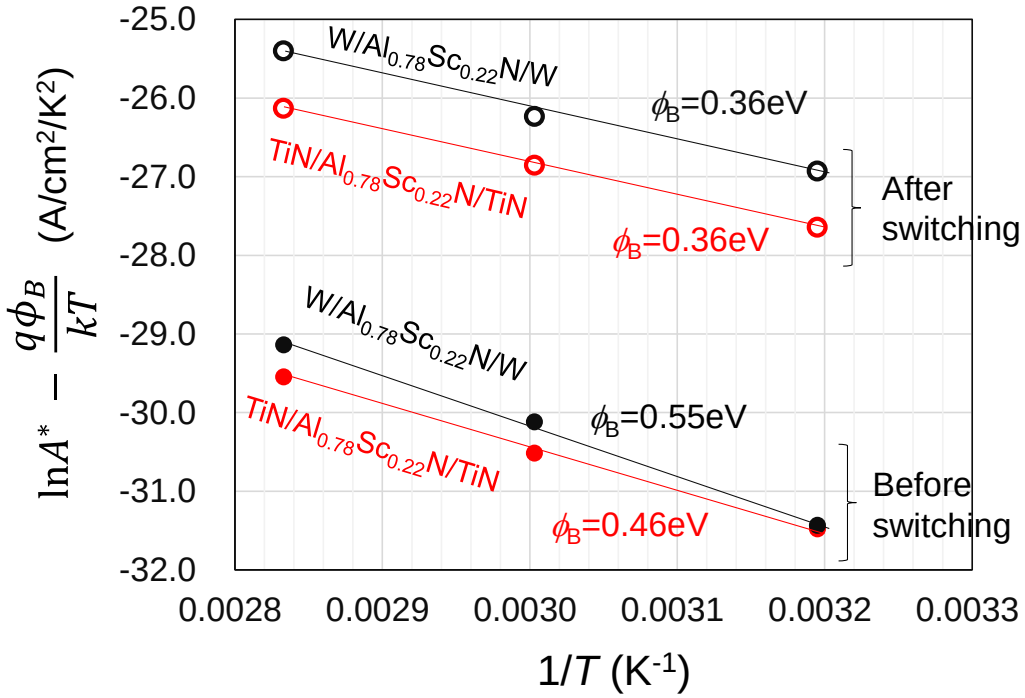

Fig. 3.7 ϕ_B extractions of TiN/$Al_{0.78}Sc_{0.22}N$/TiN capacitor and W/$Al_{0.78}Sc_{0.22}N$/W capacitor before and after the initial polarization switching.

The small A^* values can be explained if we assume the presence of a tunneling barrier layer at the $Al_{0.78}Sc_{0.22}N$/metal interface as shown in fig. 3.8. [3-28] With a conduction band difference between the tunneling barrier and the $Al_{0.78}Sc_{0.22}N$ layer ($\Delta\phi_B$) with a tunneling distance of d, the transmission probability (T_t) of a rectangular energy barrier can be approximated as

$$\ln T_t \simeq -2d\sqrt{\frac{2m^* q\Delta\phi_B}{\hbar^2}}, \qquad (2)$$

where $\hbar$ is the Dirac's constant. Under this model, the A^* in eq (1) can be replaced by the apparent Richardson constant A^*_{app} ($=A^*T_t$). Here, the origin of the tunneling barrier is

supposed to be the interface dipole layer due to the presence of nitrogen vacancies (V_N) near the interface. Since the V_N is positively charged, [3-29, 3-30] a sharp triangular-like shape potential barrier is created and to effectively reduce the conduction band of the bulk $Al_{0.78}Sc_{0.22}N$ layer. With this configuration, the ϕ_B will be seen to be reduced from the metal side accompanied by small A^*_{app} values. From the change in the A^*_{app}, it can be understood that a high concentration of V_N is already created at the interface and further increases to increase the T_t after the initial switching.

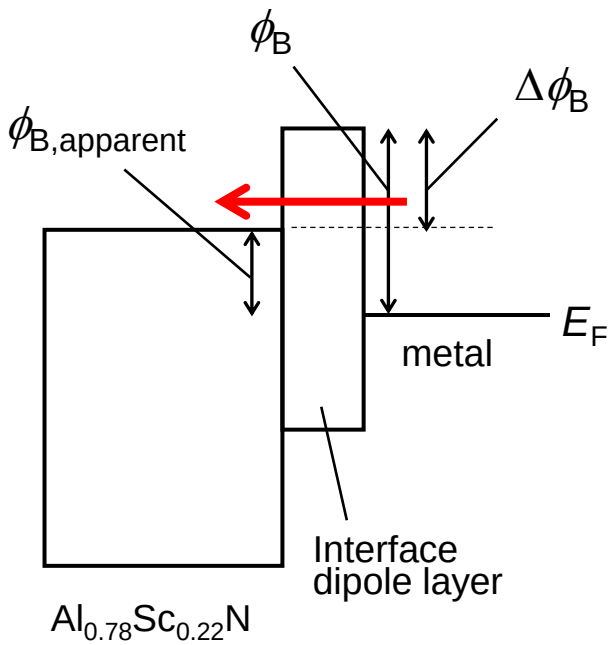

Fig. 3.8 Schematic of the presence of a tunneling barrier layer at the $Al_{0.78}Sc_{0.22}N$/metal interface.

The switching of $Al_{1-x}Sc_xN$ films is based on the movement of N atoms within the wurtzite crystal, changing the polarity between metal-face to N-face via layered hexagonal BN-type structure. [3-31] With this switching mechanism, it is indispensable to remove the N atoms that reside in the target place before moving the N atoms to the position. As a result, the switching occurs simultaneously throughout the film or within the grains, resulting in box-like shapes in the polarization-electric field (PE) curves. Therefore, to facilitate the switching, a space of V_N should be located at or near the $Al_{1-x}Sc_xN$ and metal interface for both top and bottom electrode regions as shown in fig. 3.9. V_N may also be located at grain boundaries, but the effect can be minor due to the columnar growth of the crystals.

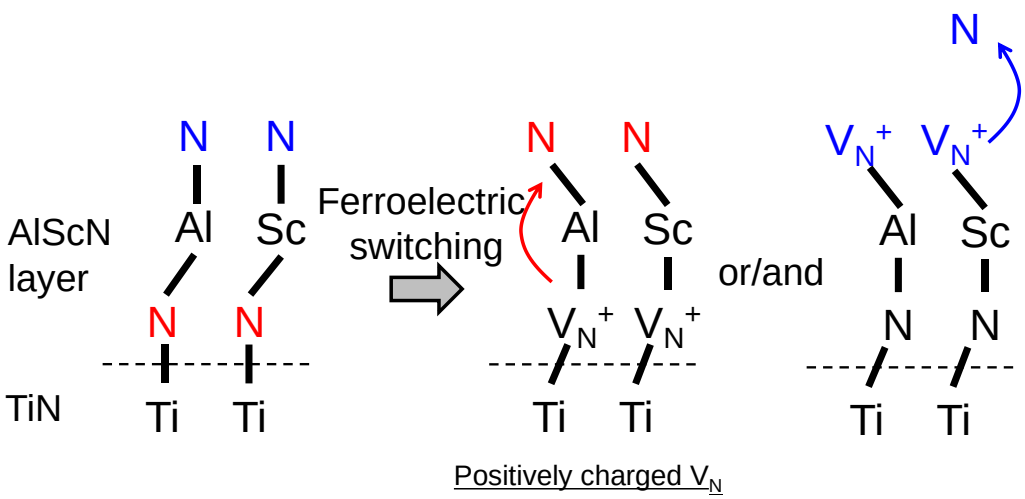

Fig. 3.9 Schematic diagram of V_N formation at the interface by initial switching.

Figure 3.10 shows the estimated $\Delta\phi_B$ and the d of the tunneling barrier layer to fit the extracted A^*_{app}. As the m^* of the $Al_{1-x}Sc_xN$ is unknown, the A^* is assumed to present in the range of 10 to 50 $Acm^{-2}K^{-2}$. We also assume a rectangular barrier for simplicity in this calculation. Here, the ϕ_B of $Al_{0.78}Sc_{0.22}N$/TiN is fixed to be 2.3 eV from an experimental

report with an E_g of 4.1 eV. [3-6] As a consequence, $\Delta\phi_B$ values of 1.84 and 1.75 eV for TiN and W electrode before the initial switching and 1.94 eV for TiN and W electrode after the initial switching were extracted with the same d of about 3 nm for both before and after the initial switching for both TiN/$Al_{0.78}Sc_{0.22}N$/TiN and W/$Al_{0.78}Sc_{0.22}N$/W capacitors. The obtained d is in good agreement with the weak contrast region dimly seen near the $Al_{0.78}Sc_{0.22}N$/TiN interface seen in fig. 3.2. The thickness is also in good agreement with a recent atomistic study on the switching of $Al_{1-x}Sc_xN$ film analysis, where a non-switching thin layer was found at the metal interface. [3-32] Under a uniform distribution of V_N in the tunneling barrier layer, the potential profile becomes quadratic dependent on the d to further increase the T_t. Under this condition, the V_N concentrations ($N_{VN}=2\varepsilon_i\Delta\phi_B/qd^2$) of the TiN/$Al_{0.78}Sc_{0.22}N$/TiN capacitor can be roughly estimated, and N_{VN} of 3.3×10^{20} and 3.5×10^{20} cm^{-3} before and after the initial switching for a singly charged V_N. Note that, the N_{VN} becomes one third for triply charged V_N. [3-29, 3-30] As for the W/$Al_{0.78}Sc_{0.22}N$/W capacitor, the N_{VN} before and after the initial switching were estimated at 3.9×10^{20} and 4.0×10^{20} cm^{-3}, respectively.

The tunneling barrier layer was already formed at the interface at the as-deposited condition and was further grown after the initial switching. The gradual increase in the leakage current can be originated from the bond breakage of Al-N or Sc-N bonds near the interface. Indeed, the measured reduction in the E at elevated temperature with an activation energy of 0.02 eV is comparable to the bond breakage value of Si-O bonds in SiO_2. [3-33] Although a physical analysis to detect the reduction in the nitrogen concentration near the interface needs to be done, our model quantitatively fulfills a realistic view of the potential shift at the interface. For TiN/$Al_{0.78}Sc_{0.22}N$ case, the difference of the V_N densities before and after the initial switching are estimated about

2.0×10^{19} cm^{-3}. For example, the changes in the band bending near the TiN/$Al_{0.78}Sc_{0.22}N$ interface may be possibly confirmed by the hard X-ray photoelectron spectroscopy (HAXPES).

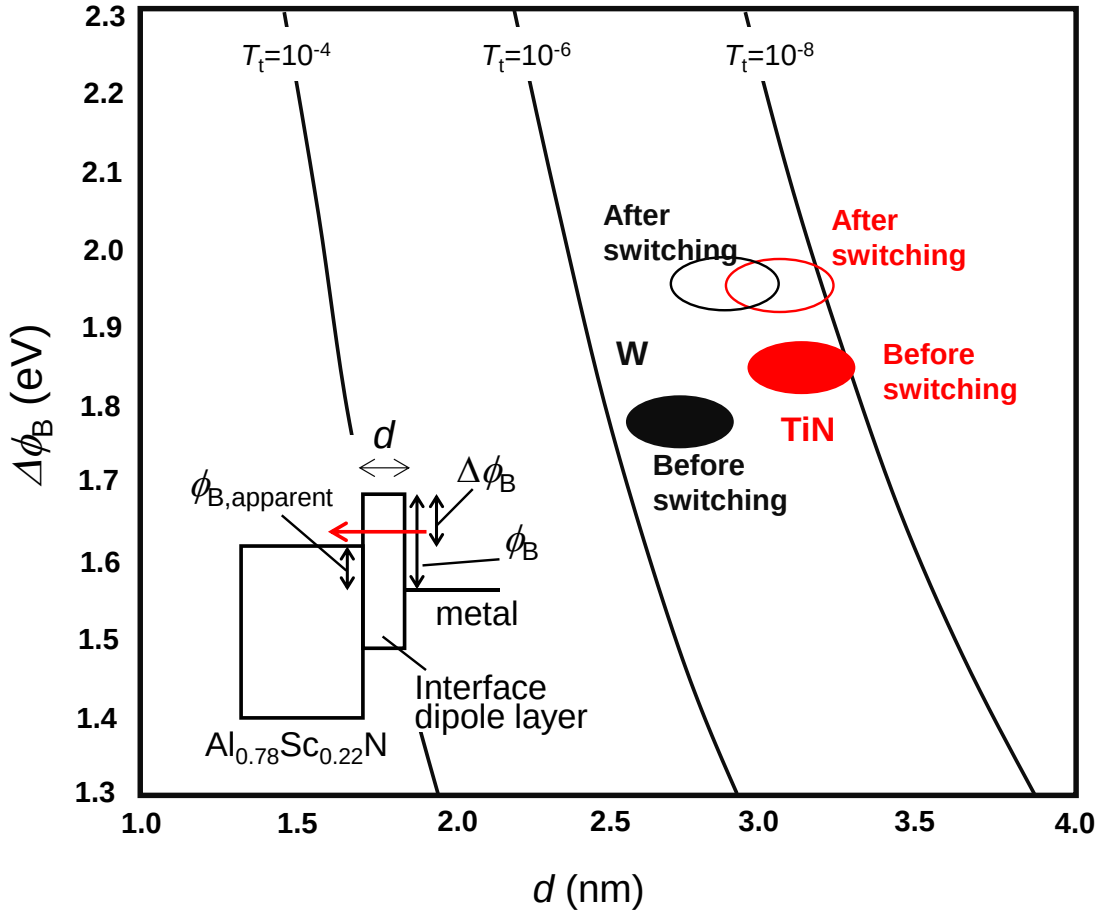

Fig. 3.10 Estimated $\Delta\phi_B$ and the d of the tunneling barrier layer to fit the extracted A^*_{app}.

Figure 3.11 shows the band alignment of the TiN/$Al_{0.78}Sc_{0.22}N$/TiN determined by the leakage current analysis. The potential level of the $Al_{0.78}Sc_{0.22}N$ film lowered due to the existence of the positively charged V_N. Therefore, the apparent ϕ_B ($\phi_{B,app}$) was seen to be lowered. The V_N increase caused by the initial switching led to the further reduction of $\phi_{B,app}$.

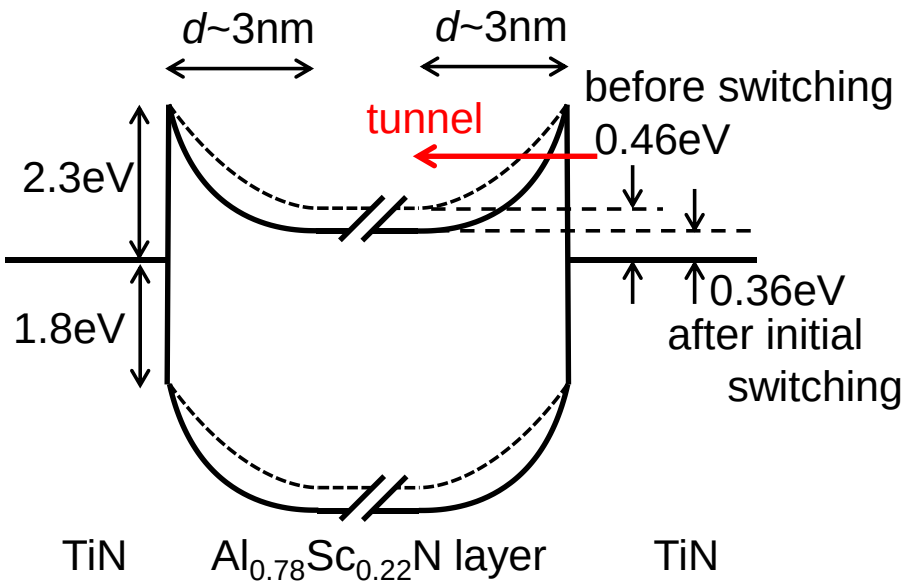

Fig. 3.11 Band alignment of the TiN/$Al_{0.78}Sc_{0.22}N$/TiN determined by the leakage current analysis.

The ϕ_M of TiN is reported of 4.55~4.77 eV (7~20 nm), [3-34] and the electron affinity and the E_g of AlN are reported of 1.4 eV and 6.1 eV. [3-35] Therefore, the valence band offset (ΔE_v) and the ϕ_B at the TiN/AlN interface are estimated at 2.8 eV and 3.3 eV as shown in fig. 3.12 (a). The E_g of the $Al_{0.78}Sc_{0.22}N$ is 4.1 eV, [3-6], which is 2 eV smaller than that of AlN. Assuming that the E_g is narrowed by 1 eV on both edges of E_c and E_v, the ΔE_v and the ϕ_B at the TiN/$Al_{0.78}Sc_{0.22}N$ interface is estimated at 2.3 eV and 1.8 eV as shown in fig. 3.12 (b). This value is in good agreement with the extracted value shown in fig. 3.11.

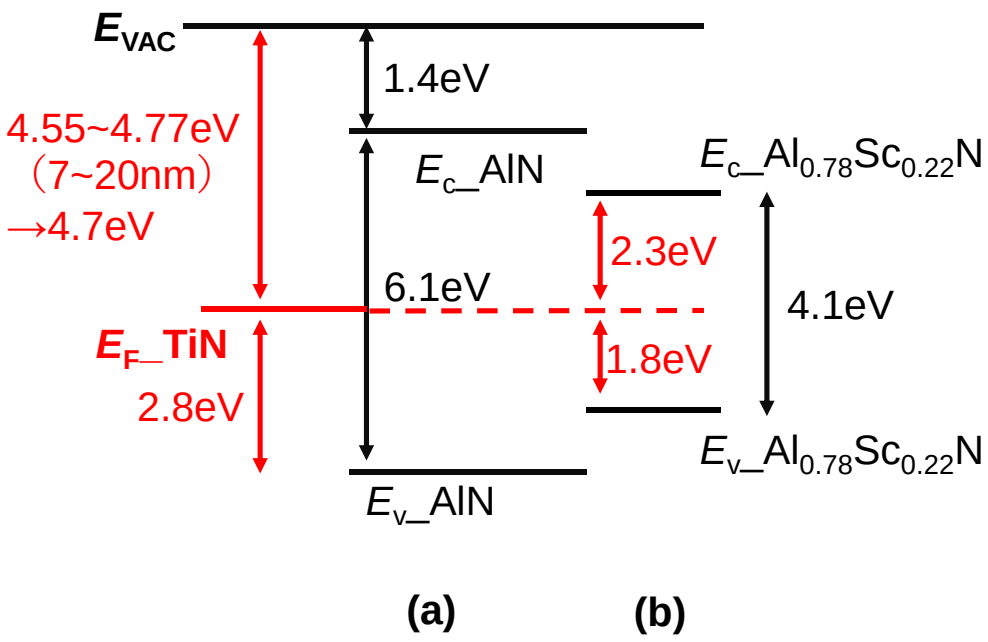

Fig. 3.12 Band alignment of the (a) TiN/AlN and (b) TiN/$Al_{0.78}Sc_{0.22}N$ interface deduced by the ϕ_M of TiN, and the electron affinity and E_g of AlN.

The interface at the metal/$Al_{1-x}Sc_xN$ film has two features; firstly the ϕ_B decreases with the initial ferroelectric polarization switching and secondly the ϕ_B does not change with the polarization direction during subsequent switching. The former is due to the movement of atoms in $Al_{1-x}Sc_xN$ film during the switching. Most of the ferroelectric material is switched by the movement of specific atoms in the unit cell, and there is no change at the metal/ferroelectric interface during the subsequent ferroelectric polarization switching. On the other hand, the $Al_{1-x}Sc_xN$ is switched by the N atoms movement simultaneously throughout the film. Therefore, V_N is formed at the metal/$Al_{1-x}Sc_xN$ interface during the initial switching as shown in fig. 3.9, leading to the irreversible changes occur at the interface. The latter is probably due to the low dielectric constant of the $Al_{1-x}Sc_xN$ film. At the metal/$Al_{1-x}Sc_xN$ interface, a voltage drop (ΔV) occurs in the ferroelectric layer due to the screening effect, and the amount of the ΔV is small due to the relatively low dielectric constant of the $Al_{1-x}Sc_xN$ film. Since the ΔV is small enough, there is almost no change in the ϕ_B depending on the direction of polarization.

Table 3.2 Comparison of the ferroelectric materials. [3-36~3-40]

Ferroelectric material	PZT (Pb (ZrxTi1-x) O_3)	HfO_2	$Al_{1-x}Sc_xN$
Movement of atoms	Ti atom in unit cell	O atoms in unit cell	N atoms in all the layer
Ferro/metal interface	Metal-O-Pb-O-Ti	Metal-O-Hf-O	Metal-N-Al/Sc Metal-V_N-Al/Sc Metal-N-Al/Sc-V_N
Dielectric constant	600	18	20
Remnant polarization	20 μC/cm^2	20 μC/cm^2	100 μC/cm^2
Voltage drop across ferroelectric layer	Large	Small	Small

The ρ_c of the TiN/$Al_{0.78}Sc_{0.22}N$ was estimated by the TFE model as expressed eq. (1.2~1.5). Figure 3.13 shows the carrier concentration dependence of the ρ_c of the TiN/$Al_{0.78}Sc_{0.22}N$. To achieve the target value, the carrier concentration of the $Al_{0.78}Sc_{0.22}N$ film is required to be 4.8×10^{18} cm^{-3} or more.

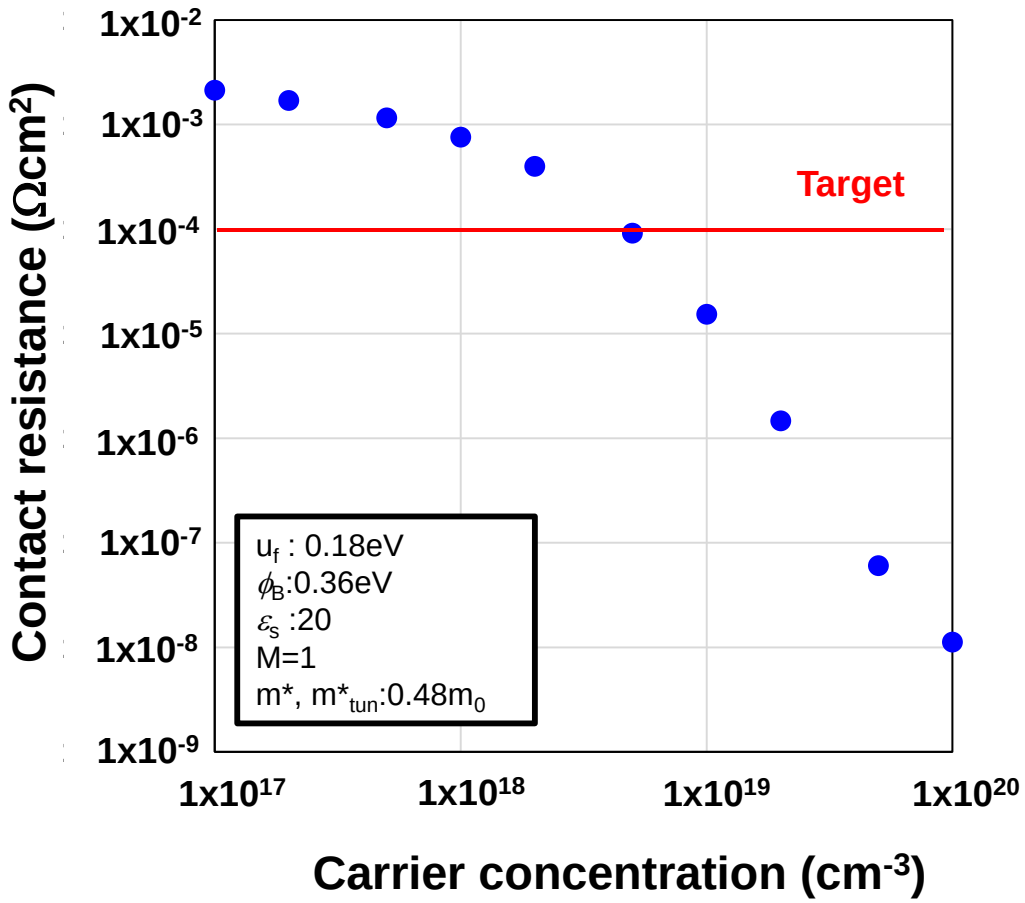

Fig. 3.13 Carrier concentration dependence of the ρ_c of TiN/$Al_{0.78}Sc_{0.22}N$ calculated by TFE model.

3.3 Summary

Leakage current analysis on 50-nm-thick ferroelectric $Al_{0.78}Sc_{0.22}N$ films with TiN and W electrodes has been performed. The electron conduction followed the Schottky emission with an initial ϕ_B of 0.46 eV and 0.55eV for TiN and W electrode. During the initial switching, a gradual shift in the leakage current was observed, changing the ϕ_B to 0.36 eV for both TiN and W electrode, and stayed constant for further switching cycles. This result indicates that the ϕ_B is almost the same whether the metal-face or N-face of the polarization of $Al_{0.78}Sc_{0.22}N$ film after the initial ferroelectric polarization switching. The small A^* was well explained by introducing a tunnel barrier layer at the interface representing a V_N-rich $Al_{0.78}Sc_{0.22}N$ layer. We infer that the reduced ϕ_B to increase the leakage current after the initial switching is inevitable to realize the ferroelectric switching in $Al_{0.78}Sc_{0.22}N$ layers.

As for the ρ_c of the $Al_{0.78}Sc_{0.22}N$/TiN, the extracted ϕ_B is relatively small for a wide bandgap material. Therefore, low contact resistance can be obtained by increasing the carrier concentration. In the calculation based on the TFE model, it is expected that the target ρ_c can be achieved by increasing the carrier concentration up to 4.8×10^{18} cm^{-3}.

References

[3-1] S. Kurtin, T. C. McGill, and C. A. Mead, Phys. Rev. Lett., **22**, 1433 (1969).

[3-2] M. Schlüter, Phys. Rev., B **17**, 5044 (1978).

[3-3] T. Nishimura, K. Kita, and A. Toriumi, Appl. Phys. Lett., **91**, 123123 (2007).

[3-4] S. Wahid, N. Chowdhury, M. K. Alam, and T. Palacios, Appl. Phys. Lett., **116**, 213506 (2020).

[3-5] P. Bampoulis, R.v. Bremen, Q. Yao, B.Poelsema, H. J. W. Zandvliet, and K. Sotthewes, ACS Appl. Mater. Interfaces, **9**, 19278 (2017).

[3-6] R. Deng, S. R. Evans, and D. Gall, Appl. Phys. Lett., **102**, 112103 (2013).

[3-7] S. Nayak, S. Acharya, M. Baral, M. Garbrecht, T. Ganguli, S. M. Shivaprasad, and B. Saha, Appl. Phys. Lett., **115**, 251901 (2019).

[3-8] S. Fichtner, F. Lofink, B. Wagner, G. Schönweger; T.-N. Kreutzer; A. Petraru, and H. Kohlstedt, "Ferroelectricity in AlScN: Switching, Imprint and sub-150 nm Films" 2020 Joint Conf. of the IEEE Int. Frequency Control Symp. and Int. Symp. on Applications of Ferroelectrics, 2020.

[3-9] S. Fichtner, N. Wolff, F. Lofink, L. Kienle, and B. Wagner, J. Appl. Phys., **125**, 114103 (2019)., suppl. material.

[3-10] D. Wang, J. Zheng, Z. Tang, M. D'Agati, P. S. M. Gharavi, X. Liu, D. Jariwala, E. A. Stach, R. H. Olsson, V. Roebisch, M. Kratzer, B. Heinz, M-G. Han, K. Kisslinger, " Ferroelectric C-Axis textured aluminum scandium nitride thin films of 100 nm thickness" 2020 Joint Conf. of the IEEE Int. Frequency Control Symp. and Int. Symp. on Applications of Ferroelectrics, 2020.

[3-11] A. Zukauskaite, G. Wingqvist, J. Palisaitis, J. Jensen, P. O. A. Persson, R. matloub, P. muralt, Y. Kim, J. Birch, L. Hultman, J. Appl. Phys., **111**, 093527 (2012).

[3-12] D. Wang, J. Zheng, P. musavigharavi, W. Zhu, A. C. Foucher, S. E. Trolier-McKinstry, E. A. Stach, R. H. Olsson, IEEE Electron Dev. Lett., **41**, 1774 (2020).

[3-13] Y. Li, G. I. Ng, S. Arulkumaran, G. Ye, Z. H. Liu, K. Ranjan, and K. S. Ang, J.

Appl. Phys., **121**, 044504 (2017).

[3-14] G. Martin, A. Botchkarev, A. Rockett, and H. Morkoç, Appl. Phys. Lett., **68**, 2541 (1996).

[3-15] J. R. Waldrop, and R. W. Grant, Appl. Phys. Lett., **68**, 2879 (1996).

[3-16] M. Akazawa, T. Matsuyama, T. Hashizume, M. Hiroki, S. Yamahata, and N. Shigekawa, Appl. Phys. Lett., **96**, 132104 (2010).

[3-17] H. C. L. Tsui, L. E. Goff, R. G. Palgrave, H. E. Beere, I. Farrer, D. A. Ritchie, and M. A Moram, J. Phys., D **49**, 265110 (2016).

[3-18] M. Akazawa, and T. Nakano, Appl. Phys. Lett., **101**, 122110 (2012).

[3-19] S. W. King, R. J. Nemanich, and R. F. Davis, Appl. Phys. Lett., **105**, 081606 (2014).

[3-20] N. G. Apostol, L.E. Stoflea, G. A. Lungu, C. A. Tache, D. G. Popescu, L. Pintilie, and C. M. Teodorescu, Mater. Sci. Eng., B **178**, 1317 (2013).

[3-21] S.-L Tsai, T. Hoshii, H. Wakabayashi, K. Tsutsui, T.-K. Chung, E. Y. Chang, K. Kakushima, Appl. Phys. Lett., doi:10.1063/5.0035335 (2021).

[3-22] C. C. Lee, J.-M. Wu, Electrochemical and Solid-State Lett., **10**, G58 (2007).

[3-23] H.-J. Cho, W. Jo, T. W. Noh, Appl. Phys. Lett., **65**, 1525 (1994).

[3-24] Y. Wang and J. Wang, J. Phys., D **42**, 162001 (2009).

[3-25] K. K. Ng and R. Liu, IEEE Trans. Electron Devices, **37**, 1536 (1990).

[3-26] Q. Zhou, H. Wu, H. Li, X. Tang, Z. Qin, D. Dong, Y. Lin, C. Lu, R. Qiu, R. Zheng, J. Wang, and B. Li, IEEE J. Electron Dev. Soc., **7**, 662 (2019).

[3-27] T. Kinoshita, T. Nagashima, T. Obata, S. Takashima, R. Yamamoto, R. Togashi, Y. Kumagai, R. Schlesser, R. Collazo, A. Koukitu, and Z. Sitar, Appl. Phys. Express, **8**, 061003 (2015).

[3-28] T. J. Vink, K. J. B. M. Nieuwesteeg, and G. Oversluizen, J. Appl. Phys., **71**, 4399 (1992).

[3-29] K. Atobe, M. Honda, N. Fukuoka, M. Okada, and M. Nakagawa, Jpn. J. Appl. Phys., **29**, 150 (1990).

[3-30] T. Koppe, H. Hofsass, and U. Vetter, J. lumin., **178**, 267 (2016).

[3-31] S. Fichtner, N. Wolff, F. Lofink, L. Kienle, and B. Wagner, J. Appl. Phys., **125**, 114103 (2019).

[3-32] N. Wolff, S. Fichtner, B. Haas, M. R. Islam, F. niekiel, M. Kessel, O. Ambacher, C. Koch, B. Wagner, F. loflnk, L. Klenle, J. Appl. Phys., **129**, 034103 (2021).

[3-33] H. Zhou, F. G. Shi, B. Zhao, and J. Yota, Appl. Phys., A **81**, 767 (2005).

[3-34] S. A. Vitale, J. Kedzierski, P. Healey, P. W. Wyatt, and C. L. Keast, IEEE Trans. Electron Devices, **58**, 419 (2011).

[3-35] H. Sun, C. G. T. Castanedo, K. Liu, K.-H. Li, W. Guo, R. Lin, X. Liu, J. Li, and X. Li, Appl. Phys. Lett., **111**, 162105 (2017).

[3-36] D. S. L. Pontes, L. Gracia, F. M. Pontes, A. Beltran, J. Andresa and E. Longo, J. Mater. Chem., **22**, 6587 (2012).

[3-37] T. Shimizu, J. Ceram. Soc. Jpn., **126**, 667 (2018).

[3-38] T. S. Böscke1, J. Müller, D. Bräuhaus, U. Schröder, and U. Böttger, Appl. Phys. Lett., **99**, 102903 (2011).

[3-40] D. Fischera and A. Kersch, Appl. Phys. Lett., **92**, 012908 (2008).

Chapter 4. Demonstration of n-type conduction of $Al_{1-x}Sc_xN$ by Si doping

In this chapter, the demonstration for the n-type conductor of $Al_{1-x}Sc_xN$ film by Si ion doping and a subsequent activation annealing was described. Si ion doping into the $Al_{1-x}Sc_xN$ film was carried out either by the ion implantation process or in-situ doping. The in-situ doping was performed by $Al_{1-x}Sc_xN$ deposition from an AlScSi sputtering target.

4.1 Ion implantation design for TiN/$Al_{1-x}Sc_xN$ structure

The ion implantation process has many advantages such as selectable any ion species, high-level control of doping location (lateral and depth direction) and ion composition, and so on. However, implantation damages to the crystal may be introduced by the collision of high energy ions.

4.1.1 Experimental details

Samples were fabricated by the following process as shown in fig. 4.1. First, a thermal oxidized Si wafer was cleaned by a mixture of H_2SO_4 and H_2O_2 for 10 min to remove the organic residues, and then by 1% HF for a short time. Then, a 50-nm-thick $Al_{0.78}Sc_{0.22}N$ and a 30-nm-thick TiN were in-situ deposited on a cleaned thermal oxidized Si wafer by reactive sputtering with $Al_{0.57}Sc_{0.43}$ compound target and Ti target in Ar and N_2 mixture at a substrate temperature of 400°C. The thickness of the TiN layer was selected to set the projection range of the following Si ion implantation (I/I) to be at the middle of the $Al_{0.78}Sc_{0.22}N$ layer. The thickness of the TiN layer was determined by TRIM/SRIM simulation as shown in fig. 4.2. Next, Si ions were implanted through the TiN film at an acceleration energy of 60 keV with a dose of 2×10^{15} cm^{-2}. After the ion implantation, TiN electrodes were patterned by lithography and wet etching process of a mixture of 29% NH_4OH: H_2O_2:H_2O = 1:5:5. Figure 4.3 shows the results of the secondary ion mass spectroscopy (SIMS) measurement. SIMS measurement revealed that the concentration of Si dopants in the Si-implanted (Si-I/I) $Al_{0.78}Sc_{0.22}N$ film ($Al_{0.78}Sc_{0.22}N$ with Si I/I) was

4.1×10^{20} cm^{-3}. Furthermore, no change in the Si concentration was shown even after 900°C annealing.

After sample fabrication, the sheet resistance (R_s), the contact resistance (ρ_c), and Hall mobility (μ_{Hall}) with carrier (donor) concentration (N_d) were extracted by the four-point probe, TLM method, and van der Pauw based Hall-effect measurements, respectively. Forming gas (FG, 3%H_2/97%N_2) annealing (FGA) processes were used to confirm the activation of the dopants from 500°C up to 900°C with a 100°C step for 3 min. To prevent the unintentional surface oxidation of the TiN layer, activation annealing was performed in FG. The films were also characterized by X-ray diffraction (XRD) under a source of the X-ray of Cu$K\alpha$ with a divergence angle of 0.04° and the transmission electron microscope (TEM).

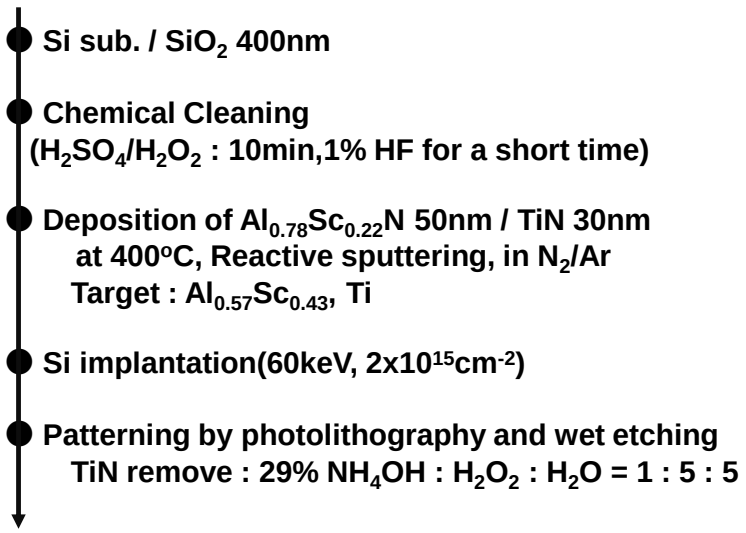

Fig. 4.1 Sample fabrication flow of Si-implanted $Al_{0.78}Sc_{0.22}N$ films.

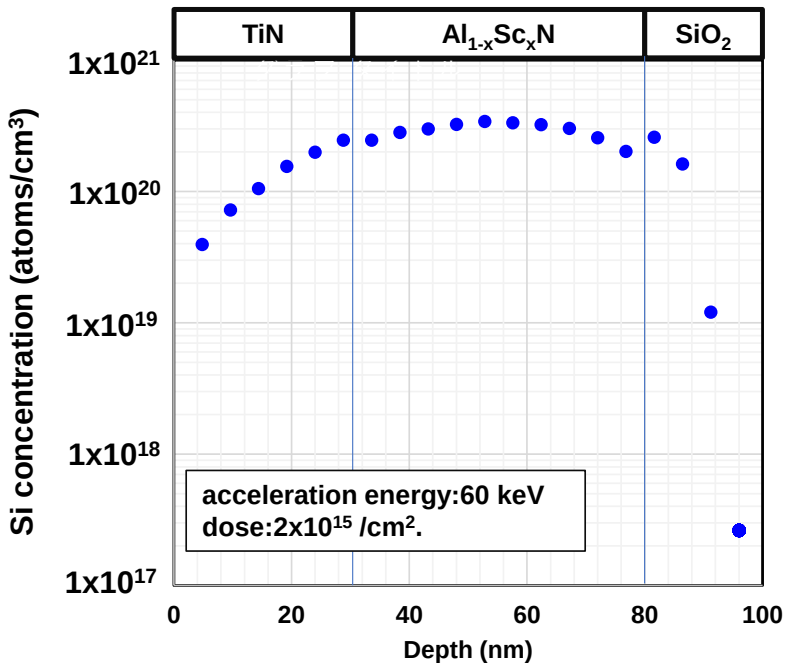

Fig. 4.2 Si atom distribution in the TiN/$Al_{0.78}Sc_{0.22}N$/SiO_2 stacked film calculated by TRIM/SRIM simulation.

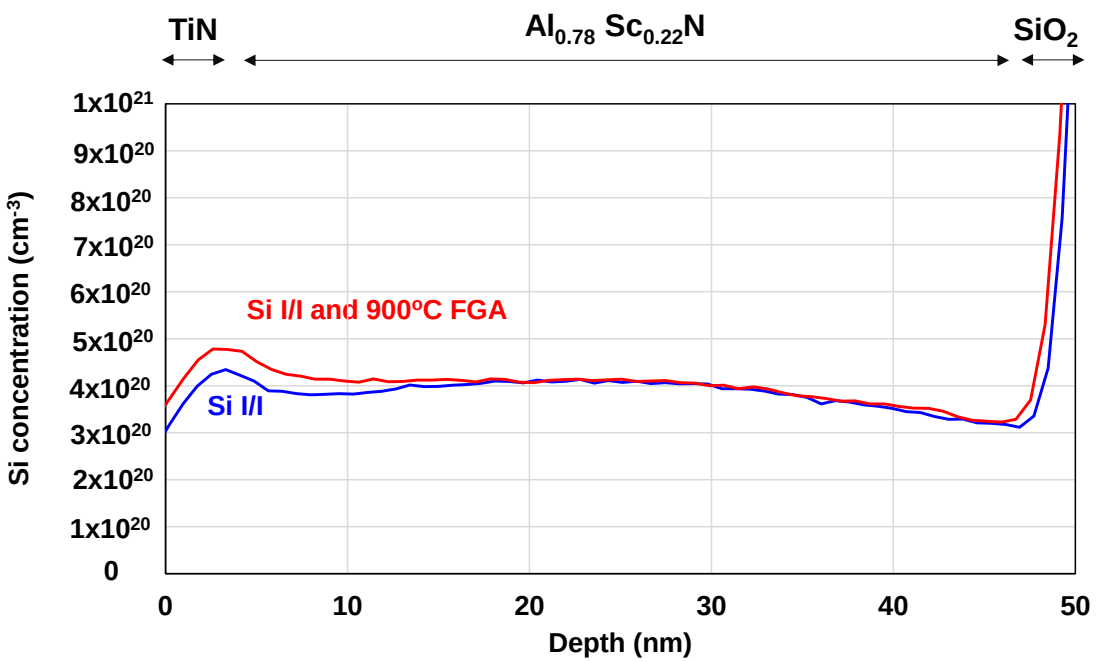

Fig. 4.3 Si concentration measured by SIMS measurement before and after annealing.

4.2 Implantation damage and thermal treatment

Figure 4.4 shows the XRD 2θ-θ patterns of the TiN (30 nm)/$Al_{0.78}Sc_{0.22}N$ with Si I/I (50 nm)/SiO_2 (400 nm)/Si substrate stacked films (a) before I/I, (b) with Si I/I, and (c) with Si I/I followed by 900°C FGA. Here, the TiN thickness of the before Si-I/I sample is about 5 nm due to a mistake in the sample making process, so the peak of TiN was not observed. As (002) peaks are only visible for all $Al_{0.78}Sc_{0.22}N$ films, it can be concluded that all the $Al_{0.78}Sc_{0.22}N$ films are in the wurtzite structure with c-axis orientation. Indeed, the XRD rocking curves of the (002) $Al_{0.78}Sc_{0.22}N$ with Si I/I reflection, shown in fig. 4.5, clearly indicate the c-axis oriented growth for all the films. The obtained full-width at half-maximum (FWHM) values of the (002) Si-I/I $Al_{0.78}Sc_{0.22}N$ reflections before I/I, after Si I/I, and Si I/I followed by 900°C FGA were 8.2°, 8.3°, and 7.4°, respectively. Although the high dose Si atoms were implanted into the $Al_{0.78}Sc_{0.22}N$ films, the implantation damage to the polycrystalline $Al_{0.78}Sc_{0.22}N$ films was not apparent from the rocking curve measurements. This might be caused by a dynamic annealing effect during the ion implantation process. The dynamic annealing effect means that the implant damage is healed by the applied heat during the ion implantation process. [4-1] S.O. Kucheyev *et al.* reported that the lattice amorphization was not observed in AlN film even after high doses of heavy-ion implantation due to its strong dynamic annealing effect. [4-2] In the AlGaN study, this dynamic annealing effect was enhanced strongly as the increase in the Al composition of AlGaN film. [4-3] $Al_{0.78}Sc_{0.22}N$ may also have the strong dynamic annealing effect due to its high Al composition ratio. The decrease in the FWHM value after 900°C FGA indicated better orientation to the c-axis.

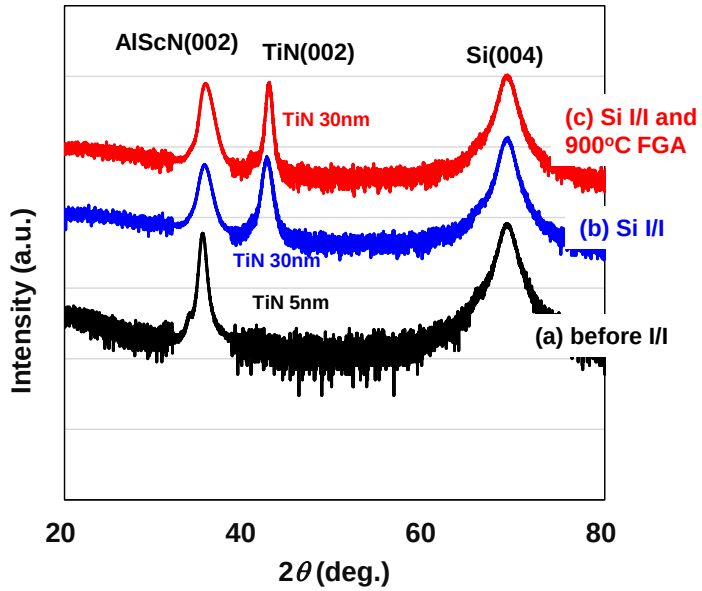

Fig. 4.4 XRD 2θ-θ patterns of the TiN/$Al_{0.78}Sc_{0.22}N$ with Si I/I/SiO_2/Si sub. with various conditions of (a) before I/I, (b) Si/I/I, (c)Si I/I, and 900°C FGA.

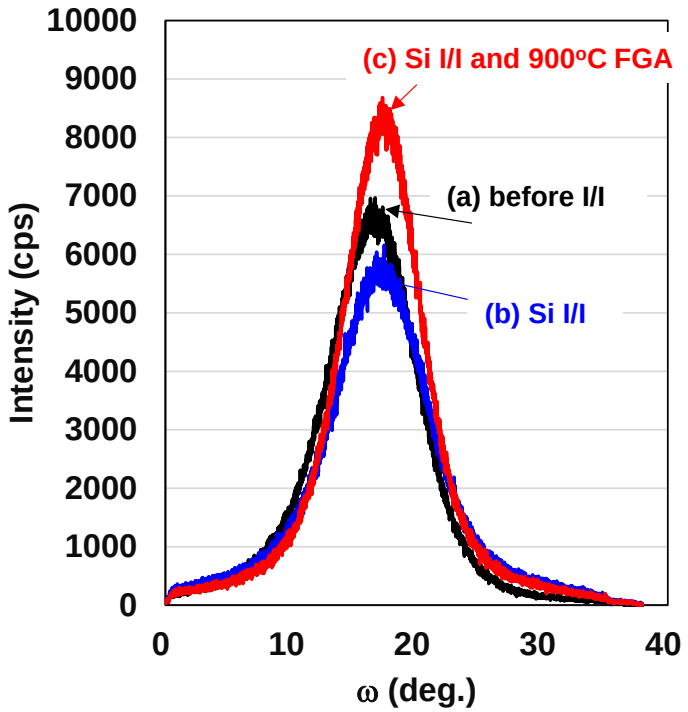

Fig. 4.5 XRD rocking curve of the (002) $Al_{1-x}Sc_xN$ with Si I/I reflection.

Cross-sectional TEM images of the Si I/I sample with before I/I (a, b), after I/I (c, d), and Si I/I and 900ºC FGA (e, f) are shown in fig. 4.6. The TiN thickness of the sample before I/I is thin but this sample is used only for TEM and XRD measurement purposes. The columnar growth of $Al_{0.78}Sc_{0.22}N$ grains in the dark-field image from the bottom to the TiN interface with a width of about 50 nm was observed in the samples of before I/I, and after Si I/I with 900ºC FGA. The grain size of the Si I/I sample became small in the vertical direction, which might be due to the implantation damage. The high-resolution image revealed the presence of lattice images throughout the grains in every sample, indicating that the $Al_{1-x}Sc_xN$ film did not amorphized by the ion implantation process. Also, the interface reaction between the $Al_{0.78}Sc_{0.22}N$ and SiO_2 layers to form an amorphous layer was found for every film. The presence of the interface layer was observed with the sample before I/I, suggesting that the layer was formed during the $Al_{0.78}Sc_{0.22}N$ deposition. The fast-Fourier transform (FFT) of the $Al_{0.78}Sc_{0.22}N$ layer from high-resolution images revealed that every film is c-axis oriented as was observed from the XRD measurements. No apparent change in the $Al_{0.78}Sc_{0.22}N$ layer was found before and after Si I/I, and before and after 900ºC FGA.

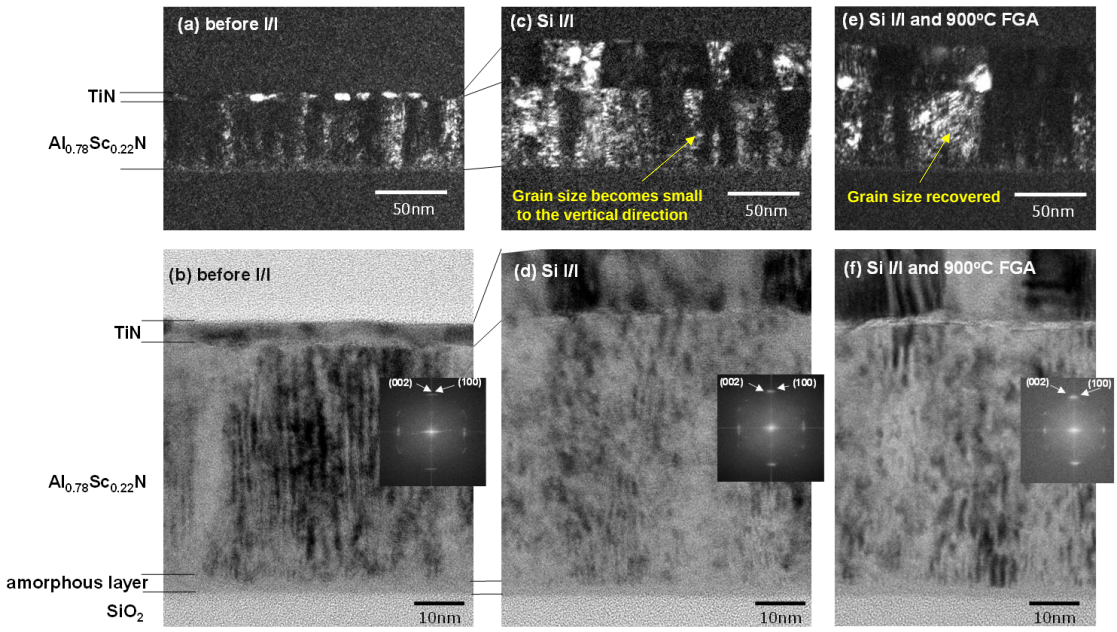

Fig. 4.6 Dark-field (a, c, e) and high-resolution (b, d, f) TEM images of the before I/I, the Si I/I, and Si I/I and 900°C FGA.

FFT images of the $Al_{0.78}Sc_{0.22}N$ layer are shown in the inset.

4.3 Annealing process for dopant activation

Figure 4.7 shows the current-voltage (*I-V*) characteristics of each FGA processed samples. Small and nonlinear *I-V* curves were obtained at 600 and 700°C FGA samples. On the contrary, a large increase in the current, as well as the Ohmic relationship, was obtained when the FGA temperature is higher than 800°C. Figure 4.8 shows the R_s of the $Al_{0.78}Sc_{0.22}N$ with Si I/I film as a function of FGA temperature. The high R_s of the order of 10^9 Ω/sq. was kept constant up to the FGA temperature of 700°C and showed a sudden decrease when annealed over 800°C. The smallest R_s of 3.2×10^5 Ω/sq. was obtained at 900°C FGA. The drop in the R_s after annealing above 800°C might be originated from the

activation of the Si atoms in the $Al_{0.78}Sc_{0.22}N$ layer. TEM and XRC measurements show the grain of the $Al_{0.78}Sc_{0.22}N$ grew to the vertical direction and the FWHM of (002) reflection decreased after 900°C FGA. These results suggest that the lattice rearrangement has occurred, and Si atoms might have replaced Al or Sc atom and bonded to N.

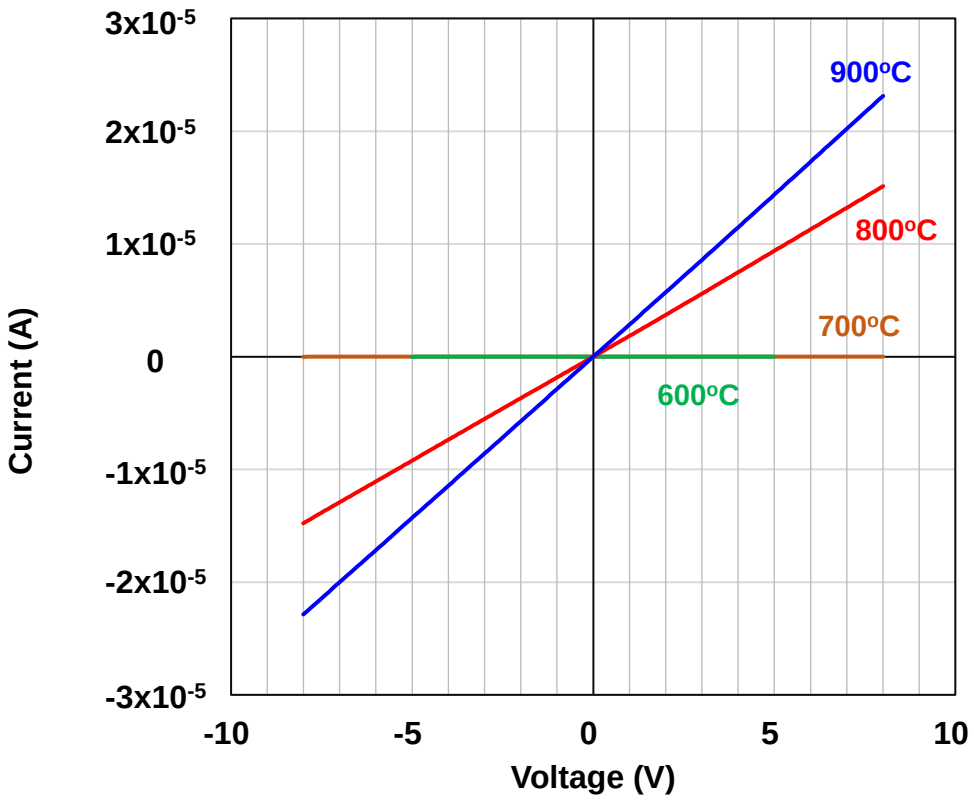

Fig. 4.7 *I-V* characteristics of the Si-I/I films after annealing at various temperatures.

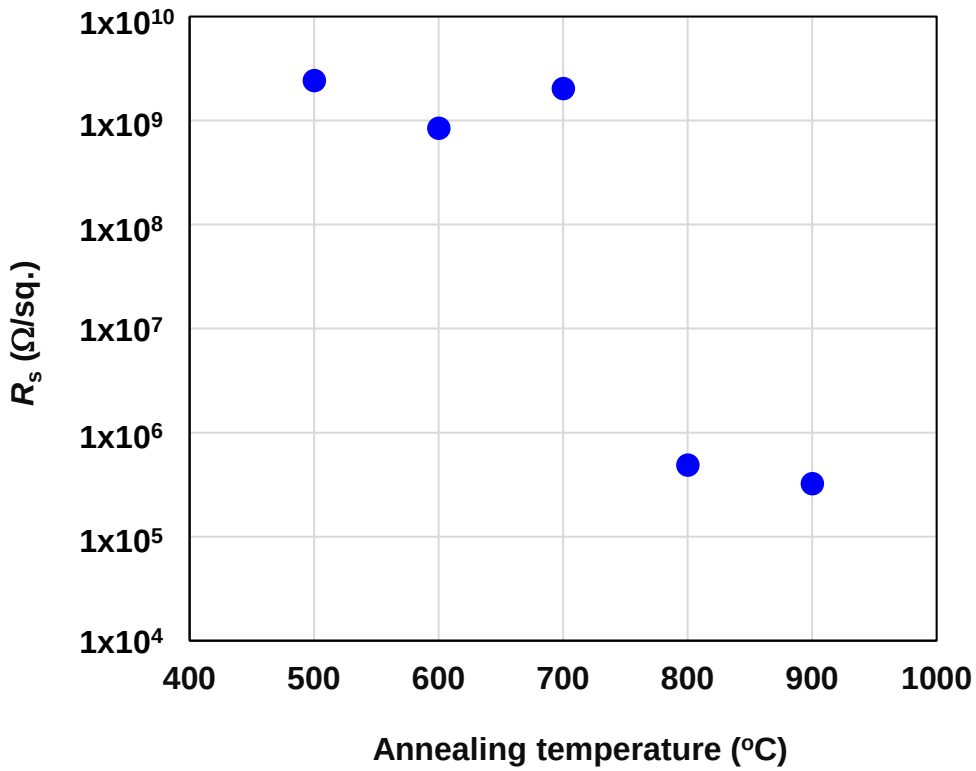

Fig. 4.8 R_s of the Si-I/I films as a function of annealing temperature in FG for 3min.

The Hall-effect measurement revealed that the $Al_{0.78}Sc_{0.22}N$ with Si I/I film after FGA at 900°C was n-type, with a μ_{Hall} and an N_d of 8.6 cm^2/Vs and 8.9×10^{18} cm^{-3}, respectively. These results indicate that the reduction in the R_s over 800°C FGA is originated from the activation of the Si atoms in the $Al_{0.78}Sc_{0.22}N$ films. The concentration of Si atom in the $Al_{0.78}Sc_{0.22}N$ films was 4.1×10^{20} cm^{-3} by SIMS measurement. Therefore, the activation ratio is estimated at 2.2%.

The activation annealing temperature of implanted Si atoms in $Al_{0.78}Sc_{0.22}N$ films was relatively low compared to those implanted into the AlN or AlGaN film. Many works of literature report that the annealing temperatures above 1100°C are required for optimal activation of Si ions in AlGaN [4-4~4-6] or AlN. [4-7] For example, Irokawa *et al*. reported the Si ion with a dose of 1×10^{15} cm^{-2} to $Al_{0.13}Ga_{0.87}N$ was activated above a temperature

of 1150°C, [4-6] and Kanechika *et al.* also reported a Si dose of 5×10^{15} cm^{-2} to AlN was activated at 1400°C. [4-7] The dissociation energies of the Al-N bond, Sc-N bond, and Si-N bond are 368±15 kJ/mol, 464±84 kJ/mol, and 437.1±9.9 kJ/mol, respectively. [4-8] Also, as $Al_{1-x}Sc_xN$ films with x>0.2 show ferroelectric switching properties, the bonding configuration becomes somewhat flexible than AlN ones. [4-9] Therefore, the dissociation of Al-N and Sc-N bonds is likely to happen to replace with Si-N bonds. To prove this model, a detailed physical analysis is required. For example, the increase in the Si-N bond might be confirmed by XPS after the activation annealing. It is reported that the DX center in AlN compensates for the free electron. [4-10] So, if both a decrease in the R_s and an increase in the Si-N bonds after the activation annealing can be confirmed, it can be inferred that Si occupied the Al site. To confirm the site occupied by Si directly, the X-ray absorption fine structure (XAFS) analysis is required.

Figure 4.9 shows the distance of electrodes dependence of the total resistance measured by the TLM method. The value of the extracted ρ_c was an unreliable value of -6.7×10^{-1} Ωcm^2. The accurate extraction of the ρ_c by TLM method was difficult due to the R_s increase by air exposure described in the next chapter.

The ρ_c was calculated using the experimentally obtained μ_{Hall} and N_d from the following equations.

$$V = IR_{total} \tag{4.1}$$

$$R_{total} = R_{se} + 2\rho_c = \frac{d}{W}\frac{1}{\mu_{Hall} N_d q} + 2\rho_c, \tag{4.2}$$

where W is the channel width (200 μm), d is the distance between two electrodes (40, 90, 140, 190, 240, 290 μm). Figure 4.10 shows the relationship between the calculated ρ_c and the distance of two electrodes. The ρ_c values were not constant and increased in proportion to the value of d, suggesting that the ρ_c could not be calculated accurately. The extracted ρ_c increases depending on d, suggesting that it is affected by the increase in the series resistance over time as described in the next chapter.

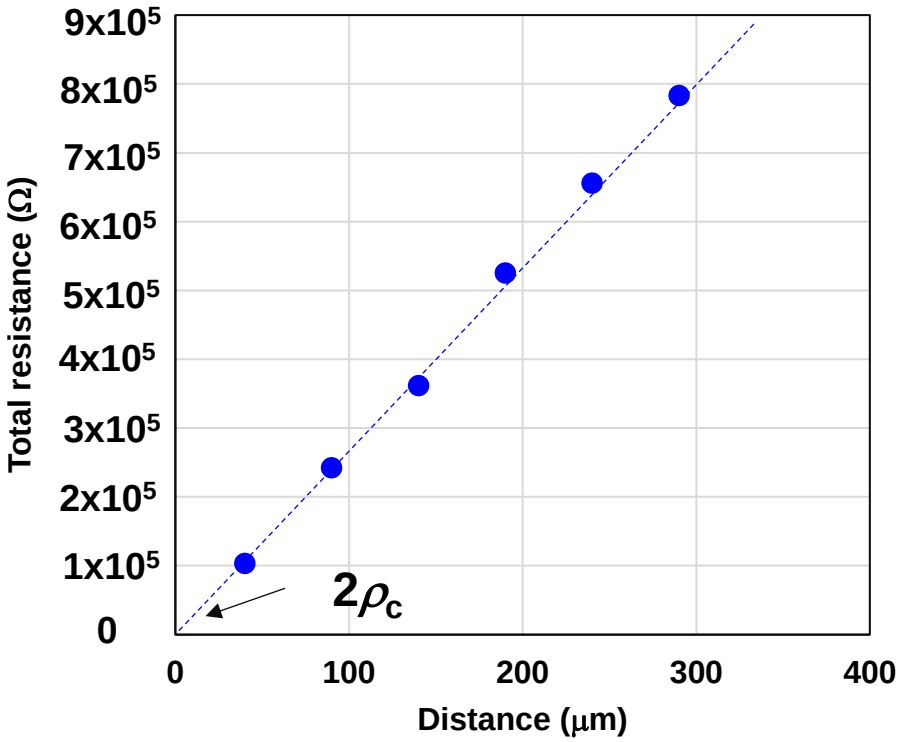

Fig. 4.9 Distance of electrodes dependence

of the total resistance measured by the TLM method.

The electrical characteristics evaluated by the TLM method were strongly influenced by the change of the series resistance over time, and it was difficult to accurately extract the ρ_c. Therefore, the ρ_c was calculated from eq. (1.2~1.5). Figure 4.11 shows the carrier concentration dependence of the ρ_c calculated by the TFE model. The carrier concentration of the $Al_{0.78}Sc_{0.22}N$ with Si I/I film after 900°C FGA is 8.9×10^{18} cm^{-3}, so the ρ_c is estimated at 2.2×10^{-5} Ωcm^2, the target ρ_c value is achieved.

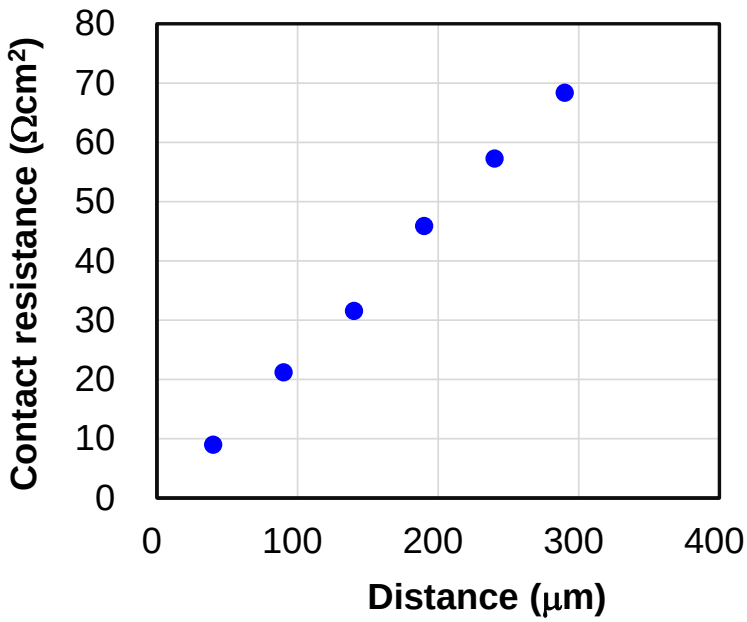

Fig. 4.10 Calculated ρ_c as a function of the distance between two electrodes.

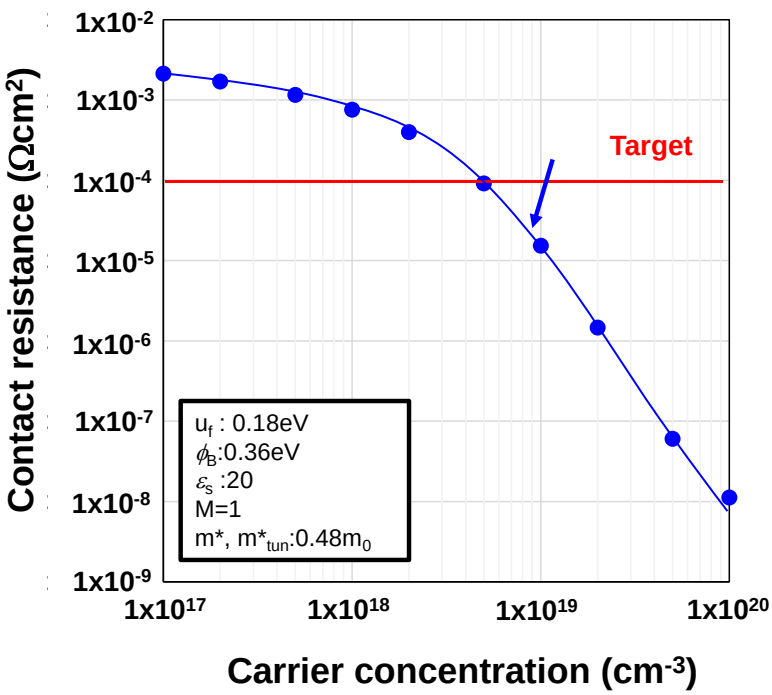

Fig. 4.11 Carrier concentration dependence of the ρ_c calculated by the TFE model.

4.4 In-situ doping with Si-doped target

The in-situ doping has an advantage of damage less but has a disadvantage in that the doping location is uncontrollable. Since this method does not cause lattice defects, it may be possible to lower the temperature of the activation annealing. For example, it was reported that the Mg-doped GaN prepared by pulsed sputtering deposition (PSD) method exhibited the p-type conduction without the activation annealing due to the low concentration of the residual hydrogen and the threading dislocation densities which compensate Mg acceptors. [4-11]

The sample fabrication flow was almost the same except for using the Si-doped target at the sputtering process and omitting the ion implantation process as shown in fig. 4.12. In-situ Si-doped AlScN (in-situ Si-doped AlScSiN) film was deposited from an $Al_{0.5675}Sc_{0.4275}Si_{0.05}$ target. Figure 4.13 shows the result of SIMS measurement. The concentration of Si dopants was 2.1×10^{19} cm^{-3}.

Figure 4.14 shows the XRD 2θ-θ patterns of the TiN (30 nm)/ in-situ Si-doped AlScSiN (50 nm)/SiO_2 (400 nm)/Si substrate stacked film. Like the $Al_{0.78}Sc_{0.22}N$ with Si I/I film, the (002) peak is only visible, indicating that the in-situ Si-doped AlScSiN film is the wurtzite structure with c-axis orientation too. Figure 4.15 shows the result of the XRC measurement. The FWHM value of the (002) reflection was 7.1°.

The *I-V* characteristics after various annealing temperatures and the R_s change as a function of FGA temperature are shown in fig. 4.16 and fig. 4.17. In the same tendency as the $Al_{0.78}Sc_{0.22}N$ with Si I/I films, the current suddenly increased and the resistance decreased after annealing at 800°C. The R_s of the in-situ Si-doped AlScSiN film was about an order of magnitude higher than that of the Si-I/I $Al_{0.78}Sc_{0.22}N$ film due to its low Si concentration of about one-twentieth.

- Si sub. / SiO_2 400nm
- Chemical Cleaning
  (H_2SO_4/H_2O_2 : 10min,1% HF for a short time)
- Deposition of in-situ Si doped AlScN 50nm / TiN 30nm
  at 400°C, Reactive sputtering, in N_2/Ar
  Target : $Al_{0.567}Sc_{0.4275}Si_{0.05}$, Ti
- Patterning by photolithography and wet etching
  TiN remove : 29% NH_4OH : H_2O_2 : H_2O = 1 : 5 : 5

Fig. 4.12 Sample fabrication flow.

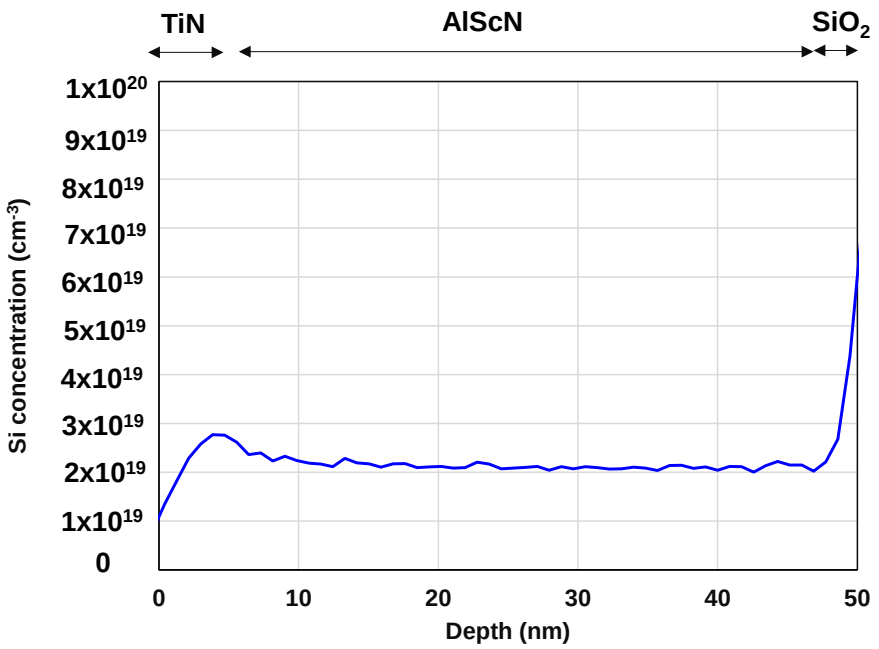

Fig. 4.13 Si concentration in the in-situ Si-doped AlScSiN film measured by SIMS measurement.

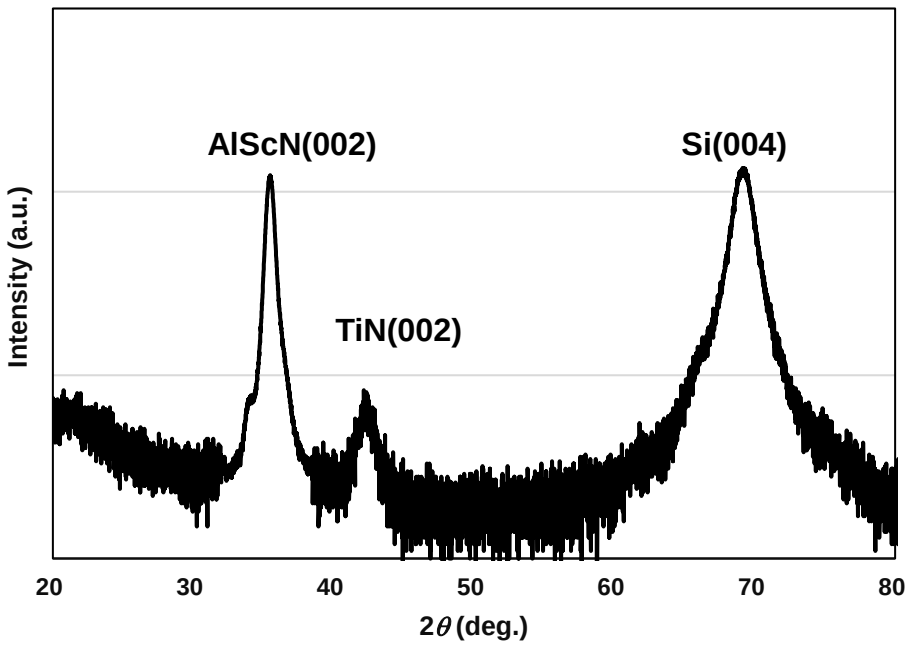

Fig. 4.14 XRD 2θ-θ patterns of the TiN/in-situ Si-doped AlScSiN/SiO_2/Si sub.

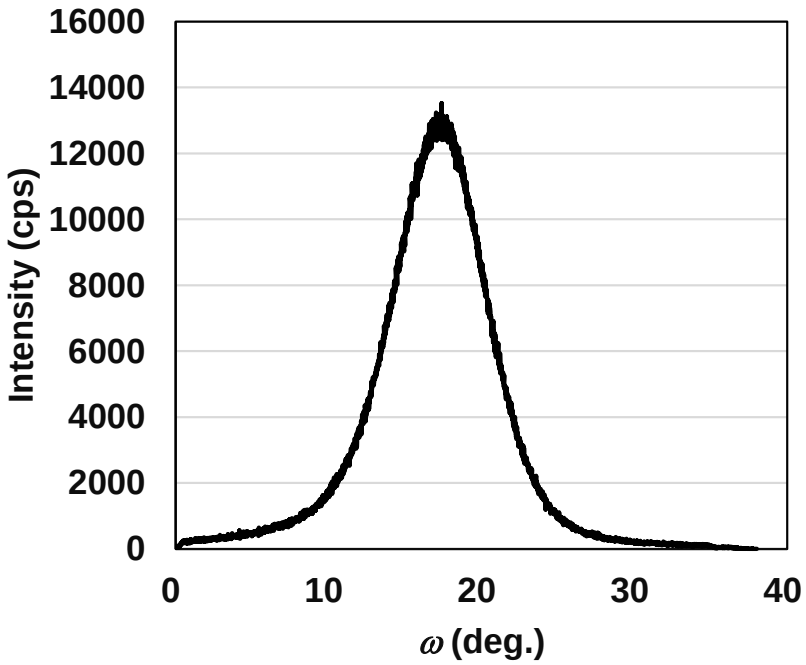

Fig. 4.15 XRD rocking curve of the (002) in-situ Si-doped AlScSiN reflection.

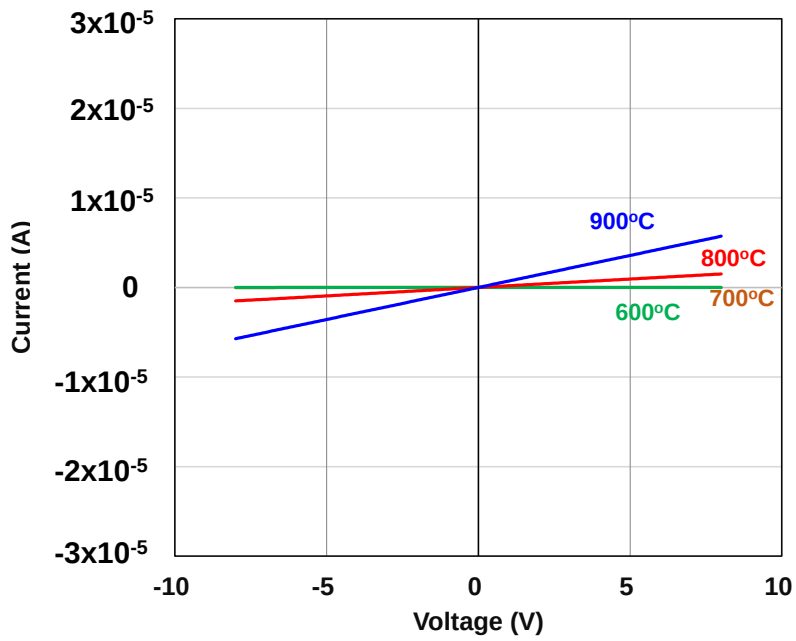

Fig. 4.16 *I-V* characteristics of the in-situ Si-doped AlScSiN films after annealing at various temperatures.

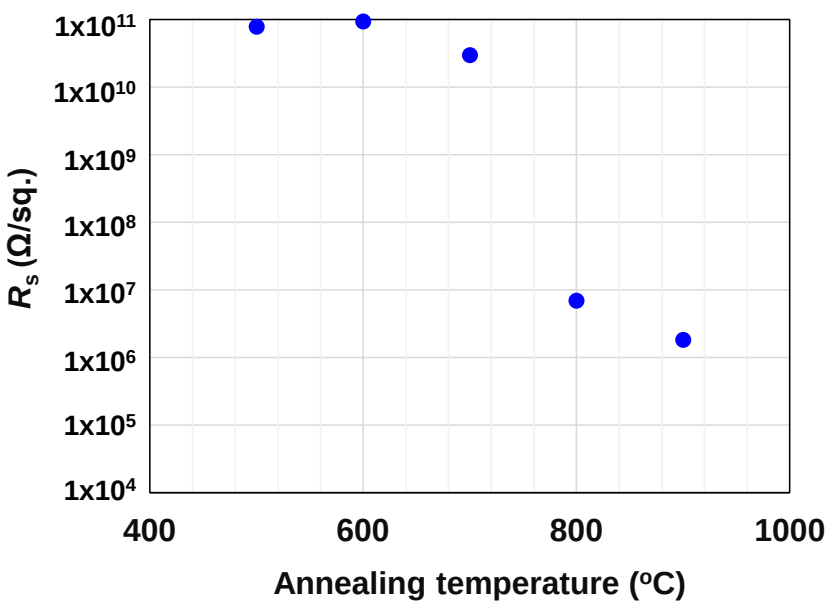

Fig. 4.17 R_s of the in-situ Si-doped AlScSiN films as a function of annealing temperature in FG for 3min.

Figure 4.18 shows the Si dose dependence (5×10^{14}, 1×10^{15}, 2×10^{15} cm^{-2}) of (a) *I-V* curve, and (b) R_s of the Si-implanted $Al_{0.78}Sc_{0.22}N$ film after 900°C FGA for 3min (using a different electrode pattern compared to the above experiment). A small and nonlinear *I-V* curve was observed with the Si dose of 5×10^{14} cm^{-2}. On the contrary, a large increase in the current and the Ohmic like behavior was obtained with the Si dose of 1×10^{15} cm^{-2}, and 2×10^{15} cm^{-2} samples. The smallest R_s of 2.0×10^{6} Ω/sq. was obtained at the Si dose of 1.0×10^{15} cm^{-2}, the R_s increased slightly as the dose increased to 2×10^{15} cm^{-2}. Since the R_s of the $Al_{0.78}Sc_{0.22}N$ film with the low Si dose of 5×10^{14} cm^{-2} does not decrease after 900°C FGA, it is deduced that the cause of the decrease in the R_s is not the defect states but the activation of Si. With the low dose case, the density of Si atoms that occupies the group III site might have decreased, and the N_d is not increased enough. With the high dose case, the mobility might have been decreased due to the increase in the impurity scattering or the cluster formation of excess Si ions.

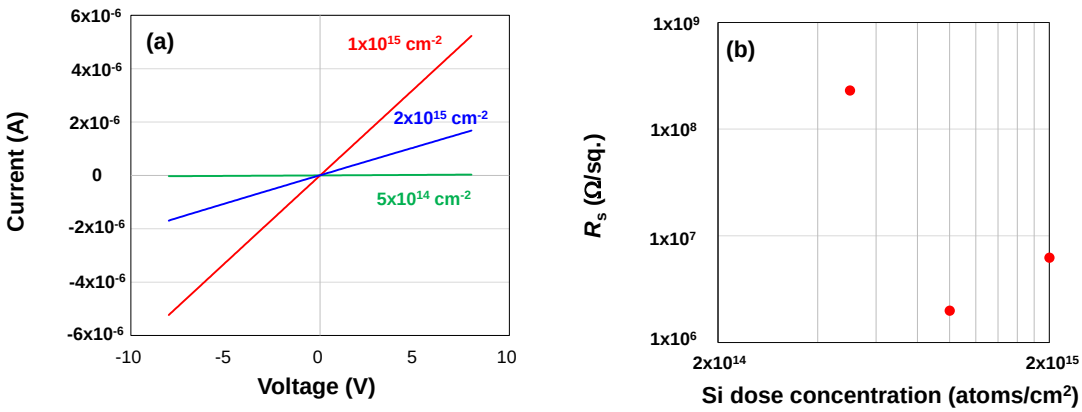

Fig. 4.18 Si dose dependence of (a) *I-V* curve and (b) R_s of the Si-implanted $Al_{0.78}Sc_{0.22}N$ film.

In this study, the activation temperature of the in-situ Si-doped AlScSiN film was the same compared to the $Al_{0.78}Sc_{0.22}N$ with Si I/I film, and the activation temperature could not be lowered by in-situ Si doping. This result differs from the reported result of the in-situ doping by the PSD. This difference may be caused by the differences in the crystal quality between both deposition methods. It is reported that the decrease in the carrier concentrations in Si-doped AlN may be caused by the compensation due to the high threading dislocation densities. [4-12] In this study, the high dislocation densities in the in-situ Si-doped AlScSiN films were probably causing no activation of Si at the low-temperature annealing. The crystal quality of the in-situ Si-doped AlScSiN film used in this study is relatively poor with the FWHM of XRC (002) reflection is 7.1°. On the other hand, the crystal quality of the film deposited by the PSD is high because the migration of metal precursors is enhanced due to the pulsed supply as shown in table 4.1. [4-11, 4-13, 4-14] Furthermore, in the case of in-situ doping by the PSD method, the enhancement of the migration of precursors caused by the pulse supply has probably assisted the replacement of Si atoms with the Al or Sc site during the deposition process.

Finally, the comparison of the $Al_{0.78}Sc_{0.22}N$ with Si I/I and in-situ Si-doped AlScSiN was summarized in table 4.2.

Table 4.1 Summary of the properties of the film deposited by the pulse sputtering.

	Method	FMHM of (002) reflection (degree)	Activation temp (^oC)	Hall mobility (cm^2/Vs)	Reference
Si-doped AlScN	reactive sputering	7.1	800-900	8.6 @ $8.9x10^{18}$ cm^{-3}	This work
Mg-doped GaN	pulse sputtering	0.089	as deposited	34 @ $7.9x10^{17}$ cm^{-3}	[4-11]
Si-doped GaN	pulse sputtering	Not mentioned	Not mentioned	110 @ $2x10^{20}$ cm^{-3}	[4-13]
Si-doped AlN	pulse sputtering	0.013	Not mentioned	44 @ $2.1x10^{14}$ cm^{-3}	[4-14]

Table 4.2 Comparison of the characteristics of the Si-I/I $Al_{0.78}Sc_{0.22}N$ film and in-situ Si-doped AlScSiN film.

	Si-I/I	in-situ Si doping
Activation temp.	~ 800 ^oC	~ 800 ^oC
Si concentration	4.1 x $10^{20}cm^{-3}$	2.1 x $10^{19}cm^{-3}$
R_s after 900^oC FGA	3.2 x 10^5(Ω/sq.)	1.8 x 10^6(Ω/sq.)
FWHM of (002) (deg.)	8.2 (as depo.) 8.3 (Si I/I) 7.4 (Si I/I and FGA)	7.1 (as depo.)
TEM	①No apparent change in the $Al_{0.78}Sc_{0.22}N$ layer was found. ②Grain size becomes small to the vertical direction after Si I/I and recovered after 900^oC FGA.	-

4.5 Summary

In this chapter, the n-type conduction of $Al_{1-x}Sc_xN$ film was demonstrated by Si doping and subsequent activation annealing above 800°C. In the case of the Si-I/I, under a dose of 2×10^{15} cm^{-2} with the activation annealing at 900°C, n-type conduction was obtained with Hall mobility and the carrier concentration of 8.6 cm^2/Vs and 8.9×10^{18} cm^{-3}, respectively. The contact resistance is estimated at 2.2×10^{-5} Ωcm^2. In the case of in-situ Si-doping, the activation temperature was found to be the same as $Al_{0.78}Sc_{0.22}N$ with Si I/I. The n-type conduction was realized in a relatively low-temperature process. This can be an advantage for applications such as the ferroelectric semiconductor-FET.

References

[4-1] https://www.eesemi.com/implant-annealing.htm

[4-2] S. O. Kucheyev, J. S.Williams, J. Zou, C. Jagadish, M. Pophristic, S. Guo, I. T. Ferguson, and M. O. Manasreh, J. Appl. Phys., **92**, 3554 (2002).

[4-3] S. O. Kucheyev, J. S. Williams, J. Zou, G. Li, C. Jagadish, M. O. Manasreh, M. Pophristic, S. Guo, and I. T. Ferguson, Appl. Phys. Lett., **80**, 787 (2002).

[4-4] Y. Irokawa, O. Ishiguro, T. Kachi, S. J. Pearton, and F. Ren, Appl. Phys. Lett., **88**, 182106 (2006).

[4-5] A. Y. Polyakov, M. Shin, M. Skowronski, R. G. Wilson, D. W. Greve, and S. J. Pearton, Solid-State Electron., **41**, 703 (1997).

[4-6] Y. Irokawa, O. Fujishima, T. Kachi, S. J. Pearton, and F. Ren, Appl. Phys. Lett., **86**, 192102 (2005).

[4-7] M. Kanechika and T. Kachi, Appl. Phys. Lett., **88**, 202106 (2006).

[4-8] J. R. Rumble (ed.) *CRC Handbook of Chemistry and Physics* (CRC Press, Boca Raton, FL, 2019) 100th ed.

[4-9] R. Deng, K. Jiang, and D. Gall, J. Appl. Phys., **115**, 013506 (2014).

[4-10] R. Zeisel, M. W. Bayerl, S. T. B. Goennenwein, R. Dimitrov, O. Ambacher, M. S.

Brandt, and M. Stutzmann, Phys. Rev., B **61**, R16283 (2000).

[4-11] Y. Arakawa, K. Ueno, A. Kobayashi, J. Ohta, and H. Fujioka, APL Mater., **4**, 086103 (2016).

[4-12] I. Bryan, Z. Bryan, S. Washiyama, P. Reddy, B. Gaddy, B. Sarkar, M. H. Breckenridge, Q. Guo, M. Bobea, J. Tweedie, S. Mita, D. Irving, R. Collazo, and Z. Sitar, Appl. Phys. Lett., **112**, 062102 (2018).

[4-13] K. Ueno, T. Fudetani, Y. Arakawa, A. Kobayashi, J. Ohta, and H. Fujioka, APL Mater., **5**, 126102 (2017).

[4-14] Y. Sakurai, K. Ueno, A. Kobayashi, J. Ohta, H. Miyake, and H. Fujioka, APL Mater., **6**, 111103 (2018).

Chapter 5. Sheet resistance instability of Si-doped $Al_{1-x}Sc_xN$ films

5.1 Sheet resistance instability

The n-type Si-doped $Al_{0.78}Sc_{0.22}N$ films turned out to be unstable as the R_s increased under air exposure, and two orders of magnitude increase in the R_s shown by exposure to air. Figure 5.1 shows the R_s overtime under air exposure with 40% relative humidity (RH). Immediately after the FGA at 900°C, the R_s of 1×10^5 Ω/sq. showed a sharp increase along with the exposure time and started to saturate, reaching two orders of magnitude higher value of the R_s of 1×10^7 Ω/sq.

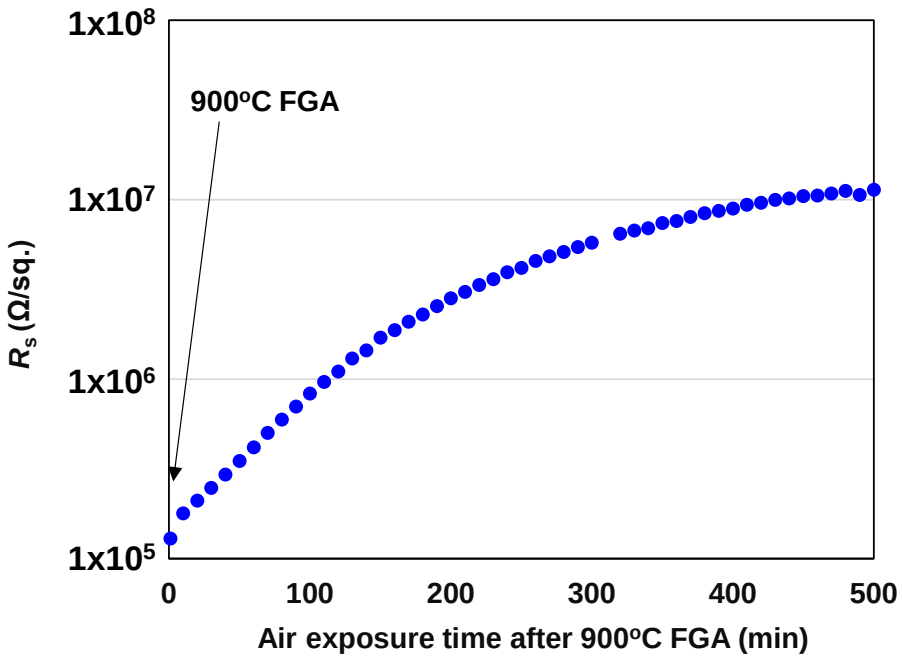

Fig. 5.1 R_s of the $Al_{0.78}Sc_{0.22}N$ with Si I/I film as a function of the air exposure time.

The cause of the R_s increase may be (1) desorption of H that terminated the dangling bond in the $Al_{0.78}Sc_{0.22}N$ film, and/or (2) adsorption of the ionic molecules in the air to the $Al_{0.78}Sc_{0.22}N$ surface. To understand the cause of R_s increase, the effect of H contained

in the annealing atmosphere and the exposed atmosphere after annealing on the increase in the R_s were investigated. H in the semiconductor forms a complex center with deep level impurities and defects, and electrically inactivating it. [5-1] Therefore, desorption of H bonded to the dangling bond in the $Al_{1-x}Sc_xN$ film may lead to deterioration of the R_s. Adsorption of ions to the surface of the $Al_{1-x}Sc_xN$ film can also degrade the R_S. It is reported that the adsorption of negative ion to the surface of n-type semiconductor causes an increase in resistivity. [5-2]

Figure 5.2 shows the R_s overtime under air exposure with 40%RH after various annealing conditions of (a) 900°C FG, (b) 900°C Ar, and (c) 300°C Ar. The increased R_s can be reset back to the initial low R_s again after 900°C annealing in Ar ambient. After that, the R_s also showed an increase with the same behavior under subsequent air exposure, indicating that H atoms in the FG are not the origin of the R_s instability. Moreover, the reset in the R_s can be done even at a temperature as low as 300°C, though not back to the initial value, suggesting that absorbates to the surface of $Al_{0.78}Sc_{0.22}N$ with Si I/I films can be desorbed at around this temperature. Table 5.1 shows the components of air. [5-3] Among them, the effects of O_2, Ar, and NO on R_s were investigated. Also, the effect of humidity was investigated.

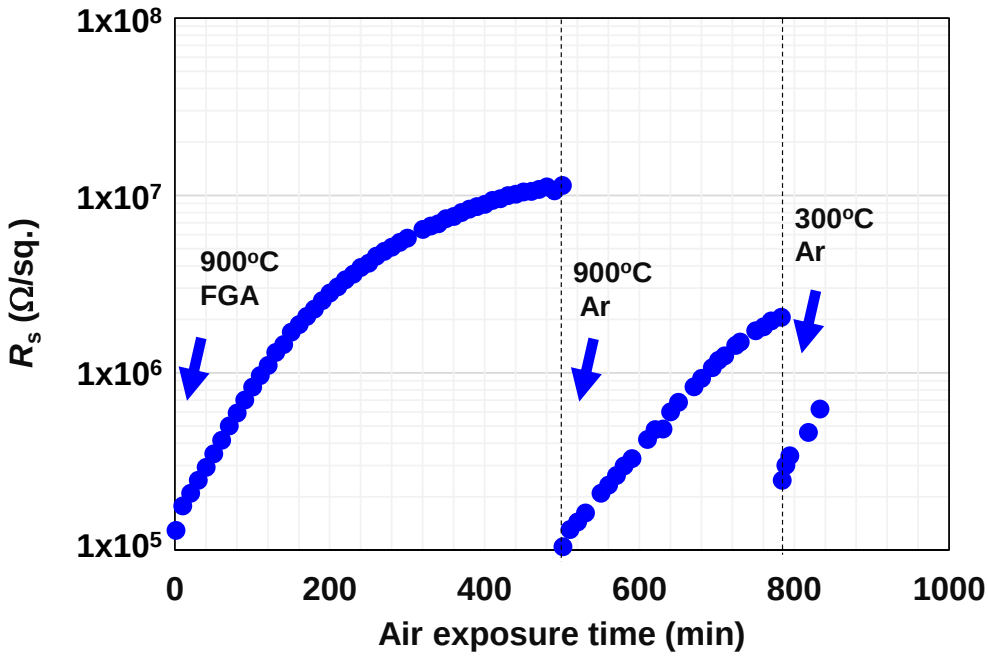

Fig. 5.2 Air exposure time on R_s of the $Al_{0.78}Sc_{0.22}N$ with Si I/I film after various annealing conditions of (a) 900°C FG, (b) 900°C Ar, and (c) 300°C Ar.

Table 5.1 Components of air.

	vol %
N_2	78.084
O_2	20.9476
Ar	0.934
CO_2	0.0314
Ne	0.001818
He	0.000524
Kr	0.000114
Xe	0.0000087
H_2	0.00005
CH_4	0.0002
N_2O	0.00005

5.2 Effect of humidity and gas on the sheet resistance

The exposure time dependence of the R_s of the $Al_{0.78}Sc_{0.22}N$ films with Si I/I films was investigated under the various environments of humid air (45%RH, 100%RH), dry air with a dew point of -20ºC, 100%Ar, mixed-NO/N_2(20%/80%), and 100%O_2. The $Al_{0.78}Sc_{0.22}N$ with Si I/I films were reset back by FGA at 900ºC and stored in a chamber under these gases ambient, except for the electrical measurement for a short period. Figure 5.3 shows the change in the R_s of the $Al_{0.78}Sc_{0.22}N$ with Si I/I film under air with different humidity, O_2, Ar, or NO exposure. A large increase in the R_s was found only under the storage conditions of air with 40%RH and 100%RH. Therefore, the change in the R_s can be originated by H_3O^+ adsorption by the self-ionization of water in the air to the surface of the $Al_{0.78}Sc_{0.22}N$ with Si I/I films. The same trend in the R_s increase between stored in 40%RH air and 100%RH air can be understood from the adsorption limited process. In other words, the increase in the R_s was dominated not by the adsorption of moisture to the exposed $Al_{1-x}Sc_xN$ surface but by the generation of H_3O^+ from H_2O at the surface of the $Al_{0.78}Sc_{0.22}N$ films.

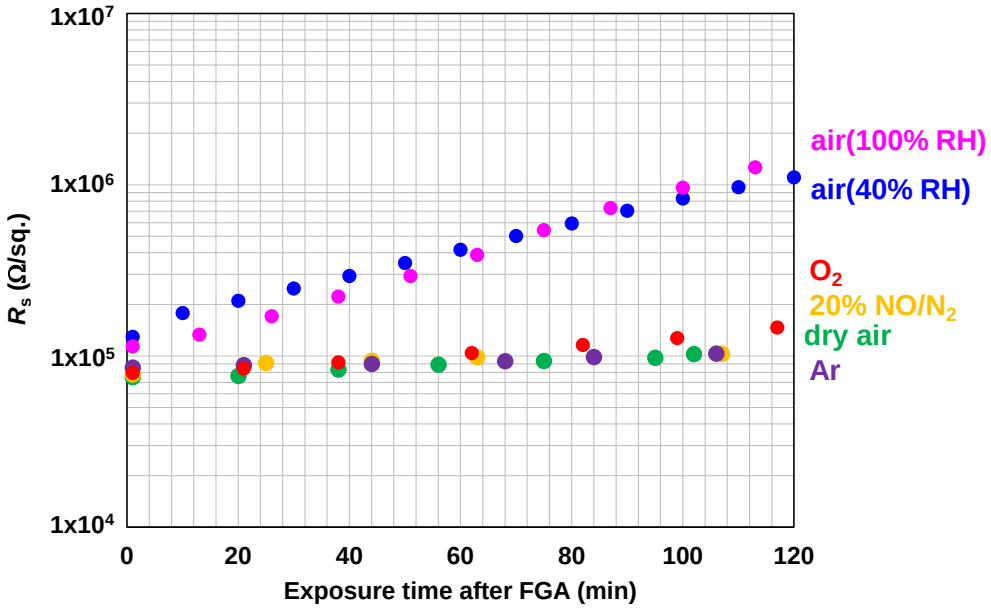

Fig. 5.3 Change in the R_s over time

under air with different humidity, O_2, Ar, or NO exposure.

5.3 Proposed model for the sheet resistivity change

The change in the R_s by exposure to air can be inferred to be caused by the high P_r (~100 μC/cm^2) of the $Al_{1-x}Sc_xN$ films. Since the surface is electrically open (floating), the potential of the surface is initially negative and gradually moves to 0 V by the molecule adsorption to the Si-doped $Al_{0.78}Sc_{0.22}N$ surface. By annealing at high temperatures above the Curie point (T_C) of the Si-I/I $Al_{0.78}Sc_{0.22}N$ film, the P_r decreases due to the pyroelectric effect, desorbing the molecules adsorbed to the surface. T_C is unknown at present but is estimated slightly higher than 300°C because of the insufficient reset of the R_s after 300°C annealing in Ar.

The model of R_s deterioration of Si-doped $Al_{0.78}Sc_{0.22}N$ film is as follows as shown in fig. 5.4. The Si-doped $Al_{0.78}Sc_{0.22}N$ film immediately after annealing above T_C has no

charges at the surface, so the potential of the surface is negative (fig. 5.4 (a)A). Under this condition, the whole $Al_{0.78}Sc_{0.22}N$ layer is conductive. As time passes, the potential of the surface gradually shifts to 0 V due to the adsorption of H_3O^+ generated by the self-ionization of H_2O. As a result, electrons from the backside of the $Al_{0.78}Sc_{0.22}N$ film start to fall to the surface and a depletion layer is formed from the backside of the film (fig. 5.4 (a)B). Therefore, the conduction path is limited to the quasi-neutral region in the film as shown in fig. 5.4 (c), leading to the apparent increase in the R_s. Once the surface potential of the $Al_{0.78}Sc_{0.22}N$ layer reaches 0 V, the system is at the thermal equilibrium state in the vertical direction, and no further increase in the R_s is shown (fig. 5.4 (a)C). Once the surface charges reach a value of P_r, the adsorption will stop.

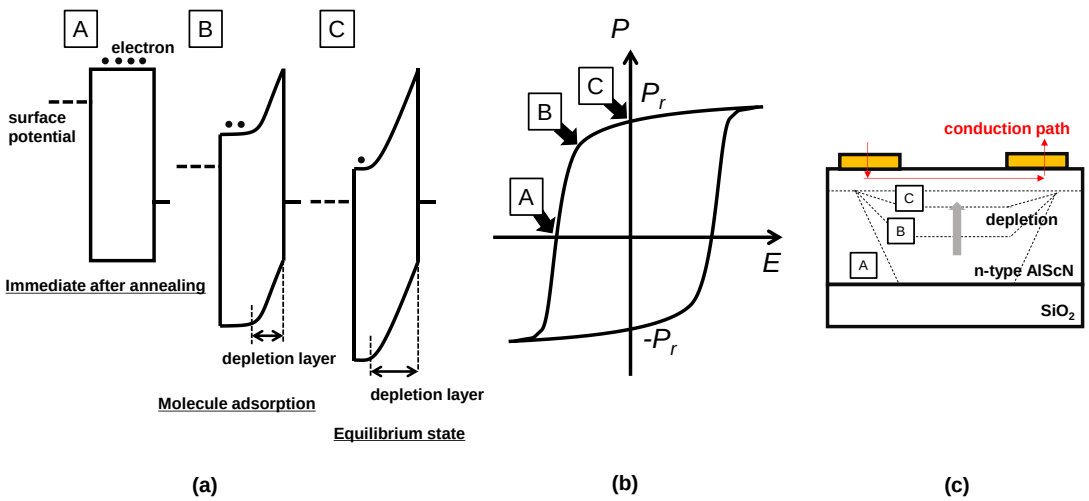

Fig. 5.4 Model of R_s deterioration of Si-doped $Al_{0.78}Sc_{0.22}N$ film. (a) Change in the band diagram of the Si-doped $Al_{0.78}Sc_{0.22}N$ film by adsorbed H_2O. “A” immediately after annealing at high temperature, “B” during molecule adsorption to the surface, and “C” at equilibrium state. (b) The ferroelectric *P-E* curve. The corresponding states are indicated by the symbol of "A", "B", and "C". (c) Formation of the depletion layer in the n-type $Al_{0.78}Sc_{0.22}N$ film.

The effect of the formation of the depletion layer on the R_s was estimated. The conductivity (σ) of the semiconductor is expressed as (5.1),

$$\boldsymbol{\sigma = \mu N_d q} \ , \qquad (5.1)$$

where μ is mobility, N_d is carrier concentration, q is the elemental charge. Figure 5.5 shows the depletion layer thickness dependence of the R_s. The R_s of the $Al_{0.78}Sc_{0.22}N$ layer increases in about two orders of magnitude by the formation of the depletion layer to the whole $Al_{0.78}Sc_{0.22}N$ layer.

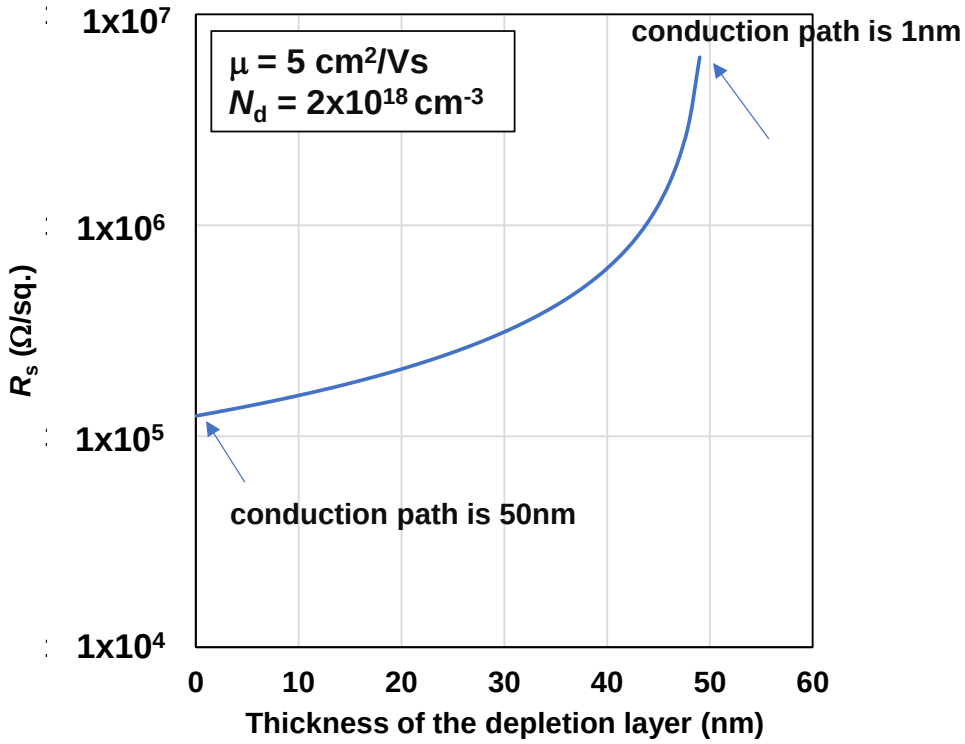

Fig. 5.5 Depletion layer thickness dependence of the R_s.

Figure 5.6 shows the relationship between the thickness of the formed depletion layer by the adsorption of H_3O^+ to the $Al_{1-x}Sc_xN$ surface and the N_d of $Al_{1-x}Sc_xN$ film. By adsorbing the H_3O^+ to the $Al_{1-x}Sc_xN$ surface, the positive charges of 6.2×10^{14} cm^{-2} (P_r/q=100 μC/cm^2) can be generated. The depletion layer formed in the $Al_{0.78}Sc_{0.22}N$ film can be estimated from the N_d (6.2×10^{14} cm^{-2}/N_d). Due to the large P_r of $Al_{1-x}Sc_xN$, the depletion layer spreads to the order of μm when the N_d is low.

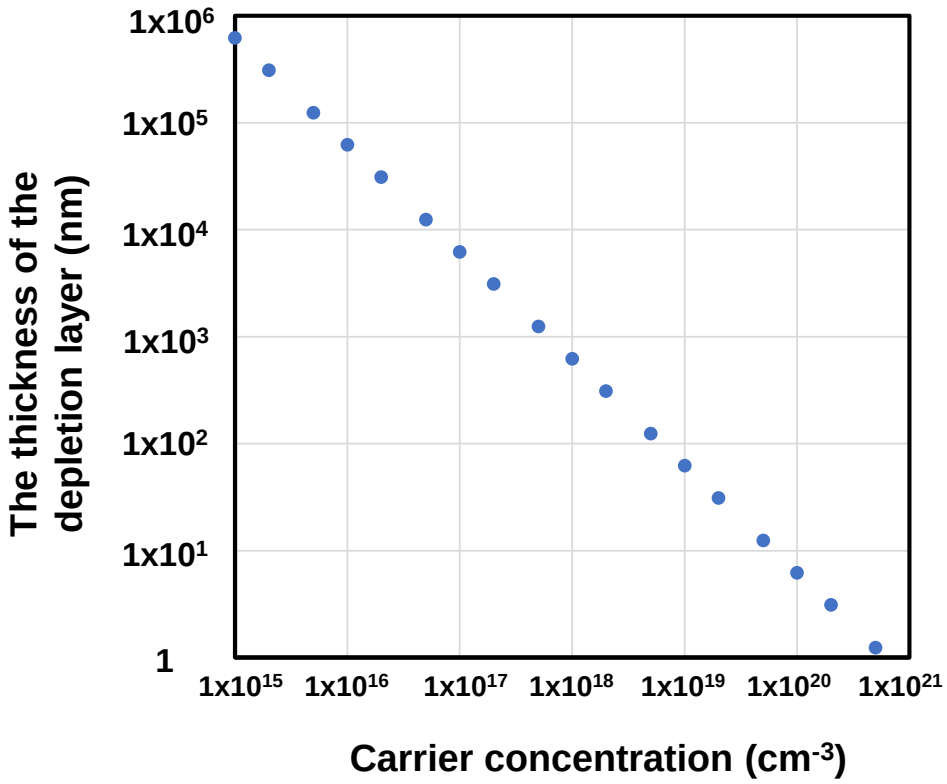

Fig. 5.6 Relationship between the thickness of the formed depletion layer by the adsorption of H_3O^+ to the $Al_{1-x}Sc_xN$ surface and the carrier concentration of $Al_{1-x}Sc_xN$ film.

It was found that the surface of the $Al_{0.78}Sc_{0.22}N$ film was sensitive to the humidity, and the R_s increased two orders of magnitude by the exposure to air. To overcome this issue, it is considered effective to deposit a proper passivation layer on the $Al_{0.78}Sc_{0.22}N$ film. The passivation layer deposited on the $Al_{0.78}Sc_{0.22}N$ film is required to have a high water barrier property. There are many reports on water vapor barrier films in the field of organic electroluminescence (EL). [5-4~5-6] The water vapor transmission rate (WVTR) of the reported films is summarized in table 5.2. SiN and Al_2O_3 films are preferable in terms of water barrier due to their lower WVTR. By the way, in the field of organic EL, the temperature of the deposition process of the barrier film is limited to around 100°C. SiO_2 film deposited at higher temperatures may also have sufficient water barrier properties.

Table 5.2 Comparison of the reported water vapor barrier films.

	WVTR ($g/m^2/day$)	reference
SiO_2	0.31 @ 100nm	[5-4]
SiN	0.012~0.003 @ 120nm	[5-5]
Al_2O_3	0.001 @ 25nm	[5-6]

5.4 Summary

In this chapter, the issue of the n-type $Al_{0.78}Sc_{0.22}N$ film was described. The surface of the $Al_{0.78}Sc_{0.22}N$ with Si I/I film was sensitive to the humidity, and the R_s increased gradually by the exposure to air due to the adsorption of H_2O. The mechanism of the R_s increase was modeled by the formation of the depletion layer at the backside of the n-type $Al_{0.78}Sc_{0.22}N$ film. To overcome this issue, the deposition of the passivation film with high water barrier properties such as SiN or Al_2O_3 to the surface was proposed. It may be effective to thicker the $Al_{0.78}Sc_{0.22}N$ film sufficiently, to increase the carrier concentration, and to protect it with an appropriate passivation film.

References

[5-1] K. Murakami, J. Vac. Soc. Jpn., **53**, 265 (2009). (in Japanese).

[5-2] Tanaka and Z. Huruhata, J. Electrochem. Soc. Jpn., **37**, 133 (1969).

[5-3] https://www.hakko.co.jp/qa/qakit/html/h01090.htm

[5-4] D. S. Wuua, W. C. Loa, L. S. Changa, and R. H. Horng, Thin Solid Films, **468**, 105 (2004).

[5-5] S. J. Kim, S. H. Yong, H. J. Ahn, Y. Shin, and H. Chae, Surf. Coat. Technol., **383**, 125210 (2020).

[5-6] M. D. Groner, S. M. George, R. S. McLean, and P. F. Carcia, Appl. Phys. Lett., **88**, 051907 (2016).

6. Conclusion

6.1 Conclusion of this thesis

In this study, characterization of the band alignment at the metal/ $Al_{1-x}Sc_xN$ interface, demonstration of the n-type conduction in $Al_{1-x}Sc_xN$ films, and the identification of the origin of the n-type $Al_{1-x}Sc_xN$ surface instability were carried out. As for the band alignment at the TiN/$Al_{1-x}Sc_xN$ interface, the leakage current analysis revealed the effective Schottky barrier height near the TiN/$Al_{0.78}Sc_{0.22}N$ interface was reduced from 0.46 to 0.36 eV due to the formation of the positively charged N vacancies by the initial ferroelectric polarization switching. The large leakage current of the TiN/$Al_{0.78}Sc_{0.22}N$/TiN capacitor can be, in turn, used as a low Ohmic contact for the metal/$Al_{1-x}Sc_xN$ interface. However, the change in the barrier height near the metal/$Al_{1-x}Sc_xN$ interface may increase the contact resistance for p-type $Al_{1-x}Sc_xN$. As for the n-type conduction, n-type $Al_{1-x}Sc_xN$ was achieved by Si ion doping and subsequent activation annealing above 800°C. This is the first experimental data that the n-type conduction of $Al_{1-x}Sc_xN$ film is realized. Si doping was performed by two methods, ion implantation, and in-situ doping. However, there was little difference in activation temperature between the two methods. This activation annealing temperature is relatively low compared to other III-N semiconductor materials. Since the n-type conduction $Al_{1-x}Sc_xN$ has been realized, the fabrication of the semiconductor device using $Al_{1-x}Sc_xN$ as a channel may be possible. The instability of the Si-doped $Al_{1-x}Sc_xN$ films in the sheet resistance was measured. It was clarified that the n-type $Al_{1-x}Sc_xN$ surface is sensitive to water absorption, and the resistance of $Al_{1-x}Sc_xN$ film increases significantly by exposure to air due to its large remnant polarization. Since the R_s increase is caused by the formation of the depletion layer from the backside of the $Al_{1-x}Sc_xN$ layer, it is necessary to thicken the ferroelectric film and increase the carrier concentration.

6.2 Future perspective

The $Al_{1-x}Sc_xN$ film still has several issues to be improved for device applications. Compared to other n-type semiconductors, n-type $Al_{0.78}Sc_{0.22}N$ film is expected that the current density is small due to its high contact resistance. Therefore, it is essential to increase the carrier concentration of the $Al_{1-x}Sc_xN$ film. Secondly, the demonstration of p-type conduction by impurity doping is required for CMOS application. Mg doping, common p-type doping species for AlN, might be a solution.

Furthermore, the conduction model between the conductive $Al_{1-x}Sc_xN$ and non-conductive $Al_{1-x}Sc_xN$ (n^+ $Al_{1-x}Sc_xN/Al_{1-x}Sc_xN$, p^+ $Al_{1-x}Sc_xN/Al_{1-x}Sc_xN$) is not yet clear. Understanding the conduction through drain-channel-source with the ferroelectric channel is necessary. Also, the mobility of the non-conductive $Al_{1-x}Sc_xN$ film is not yet clear. The extraction of the non-conductive ferroelectric $Al_{1-x}Sc_xN$ is difficult but needs to be clarified. And then, the demonstration of the ferroelectric semiconductor channel FET and the evaluation of the on-current, the off-current, the breakdown voltage, the threshold voltage controllability, and the stability are important.

In terms of mobility, OS such as IGZO shows relatively high mobility of 5~50 cm^2/Vs despite its amorphous structure. [6-1] The conduction band of OS is formed by the spatially spread metal *n*s-orbitals, where *n* is an integer (IGZO case, *n* is 5). Therefore, the overlap of adjacent metal atoms with the *n*s orbitals of OS is not easily affected by crystal strain. [6-2] As a result, the mobility of amorphous and crystal OS shows a similar value. On the other hand, the mobility of III-N semiconductors is strongly affected by their crystal quality. It is necessary to improve the crystal quality to obtain higher mobility than that of OS. In this study, Si-implanted $Al_{0.78}Sc_{0.22}N$ film shows the μ_{Hall} of 8.6 cm^2/Vs (N_d=8.9×10^{18} cm^{-3}), this value is almost the same as that of IGZO which mobility of 9 cm^2/Vs (N_d=5×10^{18} cm^{-3}). There is a possibility that the μ can be made higher than that of the OS by improving the crystal quality of $Al_{0.78}Sc_{0.22}N$ film. In the case of AlN, it has been reported that mobility of 48 cm^2/Vs was obtained deposited by the pulse sputtering

method at a relatively low temperature of 480°C. [6-3]

In terms of the off-leak characteristics, the $Al_{1-x}Sc_xN$ film is expected to be low due to its large bandgap. However, the vacancy of N or Al atoms generates their level near the conduction band bottom and the valence band maximum, [6-4] which deteriorates the off-leak characteristics. C-atom doping in the $Al_{1-x}Sc_xN$ film may be effective to reduce the off-leakage current because C in AlN is reported to compensate for the free electron in AlN films. [6-5]

For mass production, the development of the dry etching process of the $Al_{1-x}Sc_xN$ film is mandatory. In this study, the dry etching by ICP-RIE with Cl_2/BCl_3 mixture gas chemistry was performed to remove the $Al_{1-x}Sc_xN$ film for fabricating the TLM pattern. The etching rate (E/R) of $Al_{1-x}Sc_xN$ was low in the low bias condition, and the E/R increased sharply by increasing the bias from 10 W to 50 W. The low E/R of the $Al_{1-x}Sc_xN$ film at the low bias condition may be due to the low vapor pressure of $ScCl_3$. The vapor pressure of $ScCl_3$ is reported of 10^{-4} Pa at 700°C, [6-6] indicating that the $ScCl_3$ is hard to be volatilized and the removal of ScN by dry etching is difficult. The development of the dry etching process for $Al_{1-x}Sc_xN$ with high Sc composition may be necessary.

As for the application of the TFT channel materials for driving TFT of the organic light-emitting diode (OLED) displays, the n-type $Al_{1-x}Sc_xN$ film used in this study can apply for the driver TFTs in OLED display device. For the OLED display application, the on-current of the driver TFTs requires an order of 10^{-5} A. In the parabolic region of MOSFET, I_d is expressed as (6.1). [6.7]

$$\boldsymbol{I_d = \mu_{eff} C_{ox} \frac{W}{L} \frac{(V_g - V_{th})^2}{2}} \qquad (6.1)$$

In this study, μ_{Hall} of Si-doped $Al_{0.78}Sc_{0.22}N$ film is 8.6 cm_2/Vs. For example, the W is 60 μm, L is 5 μm, V_g-V_{th}=3 V, V_d is 5 V, and a 100nm-thick SiO_2 is used as an insulator, the I_d of the Si-doped $Al_{0.78}Sc_{0.22}N$ TFT calculated from the eq. (6.1) is 1.6×10^{-5} A. This value

meets the I_d spec of the driver TFTs of the OLED display device. However, for OLED display applications, it is essential to lower the activation annealing temperature.

References

[6-1] T. Kamiya and H. Hosono, NPG Asia Mater., **2**, 15 (2010).

[6-2] K. Nomura, H. Ohta, A. Takagi, T. Kamiya, M. Hirano and H. Hosono, Nature, **432**, 488 (2004).

[6-3] Y. Sakurai, K. Ueno, A. Kobayashi, J. Ohta, H. Miyake, and H. Fujioka, APL Mater., **6**, 111103 (2018).

[6-4] T. L. Tansley and R. J. Egan, Phys. Rev., B **45**, 942 (1992).

[6-5] J. S. Harris, J. N. Baker, B. E. Gaddy, I. Bryan, Z. Bryan, K. J. Mirrielees, P. Reddy, R. Collazo, Z. Sitar, and D. L. Irving, Appl. Phys. Lett., **112**, 152101 (2018).

[6-6] https://patents.google.com/patent/JP5884840B2/ja

[6-7] Y. Taur and T. H. Ning, *Fundamentals of Modern VLSI Devices*, 2nd ed. (Cambridge University Press, 2009).

List of Publications

Journal papers

1.

Junji Kataoka, Sung-Lin Tsai, Takuya Hoshii, Hitoshi Wakabayashi, Kazuo Tsutsui, Kuniyuki Kakushima,

"n-type conduction of sputter-deposited polycrystalline $Al_{0.78}Sc_{0.22}N$ films by Si ion implantation", Appl. Phys. Express, **14**, 021002 (2020).

2.

Junji Kataoka, Sung-Lin Tsai, Takuya Hoshii, Hitoshi Wakabayashi, Kazuo Tsutsui, Kuniyuki Kakushima,

"A possible origin of the large leakage current in ferroelectric $Al_{1-x}Sc_xN$ films", Jpn. J. Appl. Phys., https://doi.org/10.35848/1347-4065/abe644 (2021).

Acknowledgments

First of all, I would like to express the deepest appreciation to the supervisor Assoc. Prof. Kuniyuki Kakushima for all of his dedicated guidance, helpful advice, and attentive support.

I am also deeply grateful to Prof. Hiroshi Iwai, Prof. Kazuo Tsutsui, Prof. Hitoshi Wakabayashi, Assoc. Assoc. Prof. Hiroaki Iino for reviewing the thesis and for valuable advice.

I would like to express my appreciation to Mr. Sung-Lin Tsai, Mr. Song Jinhan, Mr. Kazuto Mizutani for their warm supports.

I would like to express my gratitude to Dr. Keiji Suzuki, Mr. Minoru Inomoto, Dr. Hiroyuki Fukumizu, Mr. Shuichi Kuboi for giving me the opportunity to this research.

Finally, I would like to appreciate to my wife Nozomi, my parents, and all of my family members for their support and encouragement.